RUSSIAN ACADEMY OF SCIENCES
SIBERIAN BRANCH
INSTITUTE OF THEORETICAL AND APPLIED MECHANICS
INTERNATIONAL CENTER OF AEROPHYSICAL RESEARCH

HYPERSONIC CROSSING-SHOCK-WAVES/TURBULENT BOUNDARY LAYER INTERACTIONS

A.A. Zheltovodov, A.I. Maksimov

EOARD Contract F61775-98-WE091

FINAL REPORT FOR THE PERIOD

APRIL 1998 – APRIL 1999

Novosibirsk 1999

REPORT DOCUMENTATION PAGE

Form Approved OMB No. 0704-0188

1. AGENCY USE ONLY (Leave blank)	2. REPORT DATE	3. REPORT TYPE AND DATES COVERED
	1999	Final Report

4. TITLE AND SUBTITLE

Hypersonic Crossing Shock-Waves/Turbulent Boundary Layer Interaction

5. FUNDING NUMBERS

F61775-98-

6. AUTHOR(S)

Dr. Alexander Zheltovodov

7. PERFORMING ORGANIZATION NAME(S) AND ADDRESS(ES)

Institute of Theoretical and Applied Mechanics
Institutskaya 4/1
Novosibirsk 630090
Russia

8. PERFORMING ORGANIZATION REPORT NUMBER

N/A

9. SPONSORING/MONITORING AGENCY NAME(S) AND ADDRESS(ES)

EOARD
PSC 802 BOX 14
FPO 09499-0200

10. SPONSORING/MONITORING AGENCY REPORT NUMBER

SPC 98-4037

11. SUPPLEMENTARY NOTES

12a. DISTRIBUTION/AVAILABILITY STATEMENT

Approved for public release; distribution is unlimited.

12b. DISTRIBUTION CODE

A

13. ABSTRACT (Maximum 200 words)

This report results from a contract tasking Institute of Theoretical and Applied Mechanics as follows: The contractor will help the CFD group at AFRL to better understand shock-wave/turbulent boundary layer phenomena by providing a comprehensive set of experimental data with emphasis on both quantitative and flow visualization aspects. He will fill-in the gaps which exist in the test matrix both at Mach 4 and 5. He will also expand the range of measurements to include shock structure and skin friction coefficient data.

14. SUBJECT TERMS

EOARD, Separated Flows, Hypersonic Flow, Shock Waves

15. NUMBER OF PAGES

78

16. PRICE CODE

N/A

17. SECURITY CLASSIFICATION OF REPORT	18. SECURITY CLASSIFICATION OF THIS PAGE	19. SECURITY CLASSIFICATION OF ABSTRACT	20. LIMITATION OF ABSTRACT
UNCLASSIFIED	UNCLASSIFIED	UNCLASSIFIED	UL

Institute of Theoretical and
Applied Mechanics

By _____
Deputy director,
Prof. A.M.KHARITONOV

LIST OF AUTHORS

Date of Signature

_____ 04/12/99

Dr. Alexander A. ZHELTOVODOV
Head of Separated Flows Research Group,
Senior Research Scientist

_____ 04.12.99.

Dr. Alexander I. MAKSIMOV
Senior Research Scientist

FOREWORD

This document presents a detailed investigation of super- and hypersonic crossing-shock-waves/turbulent boundary layer interactions. New experimental studies were conducted at Institute of Theoretical and Applied Mechanics, Rusian Academy of Sciences, Siberian Branch (Russia, Novosibirsk) and the DLR Institute of Fluid Mechanics (Goettingen, Germany).

This final report, submitted by the authors, describes all the work accomplished for the duration of the EOARD Contract F61775-98-WE091 (monitor Dr. C.Raffoul) from April 1998 to April 1999.

ABSTRACT

The specific features of 3-D interaction of symmetric crossing-shock-waves/turbulent boundary layer interactions in the vicinity of two vertical fins mounted on a flat plate under the conditions of super- and hypersonic velocities are considered. A detailed comparison of numerical results based on Reynolds-averaged full Navier-Stokes equations and the k - ε model of turbulence with experimental data for the Mach number $M_\infty = 3.9$ and deflection angles of the side surfaces of the fins $\beta = 7, 11$ and $15°$ is performed. The surface pressure distributions in the interaction region, topological features of the limiting streamlines on the plate and on the side surfaces of the fins are analyzed for these cases parallel with the new experimental results for $\beta = 8 - 23°$ at $M_\infty = 5$ and some previous studies at $M_\infty = 8.3$. Possible reasons for discrepancy between the calculations and data as well as possibilities of further improvement of calculations are discussed. The new experimental data at the Mach number $M_\infty = 5$ are documented for the purpose of their subsequent use to verify CFD codes.

CONTENTS

INTRODUCTION

The study of 3-D interaction of shock waves with a turbulent boundary layer is one of the most complicated problems of gas dynamics, which is important for practical applications. These interactions are observed both in an external supersonic flow around various elements of flying vehicles and in internal flows, for example, in supersonic inlets. Limited possibilities of predicting their properties and further development of advanced numerical methods require a comprehensive understanding of the physics of such flows by examples of simplified canonical configurations that model the elements of real flying vehicles [1–4]. Among these configurations actively studied in connection with the development of promising inlets with spatial compression there are two vertical fins with inflected internal side surfaces mounted on a flat plate. The interaction of crossing shocks and expansion waves with a turbulent boundary layer on the internal surfaces of the half-channel is realized in a supersonic flow around these fins (Fig. 1.1, *a*). It is known that the emergence of intense perturbations in inlets induced by a possible separation of the boundary layer and the formation of spatial vortex structures can be accompanied by a substantial growth of the total pressure loss and significantly affect the inlet characteristics. Thus, it is important to refine the physical features of these flows to seek for promising configurations and effective methods for pressure loss reduction.

As it follows from a rather comprehensive review of investigations of the flow in the vicinity of fins with equal and different angles of deflection of the side surfaces [3–6], the advanced calculations based on the numerical solution of the Reynolds-averaged full Navier-Stokes equations using various models of turbulence allow a correct prediction of only some properties of these flows. For example, the numerical results are in good agreement with experimental data for the wave structure formed in the half-channel under the conditions of viscid-inviscid interaction, the fields of various parameters of the mean flow, the pressure distribution on the surface under the conditions of weak- and moderate-strength disturbances. This agreement, however, significantly decreases as the strength of the crossing shocks increases. The same situation occurs in the central separation region formed around the crossing point of the shock waves, where viscous effects prevail, in

comparison with external regions of the boundary layer in which the flow is predominantly inviscid. Significant differences are observed between the calculated and experimental distributions of the skin friction and heat transfer coefficients in interaction regions. These features, in particular, are typical of some specific cases of the flow around symmetric and asymmetric fins considered at the previous stages of the study [3, 7–13].

To clarify possible reasons for these discrepancies, it is necessary to perform a more careful analysis of the flow structure obtained numerically for the case of varied strength of the shock waves and a systematic comparison of the results with experiment. Taking into account that only one paper describes experimental studies for hypersonic speeds [14], it is important to expand the experimental data base for verification of numerical methods under these conditions.

The present report is the next stage of previously started studies [3]. In the first part we analyzed symmetric crossing-shock-waves/turbulent boundary layer interactions with increasing angles of deflection of the side surfaces under the conditions of super- and hypersonic velocities. A detailed comparison of experimental data obtained at ITAM SB RAS [3] for the Mach number $M_\infty = 3.9$ and deflection angles of the side surfaces of the fins $\beta = 7$, 11, and 15° with the results of numerical calculations based on Reynolds-averaged full Navier-Stokes equations and the k - ε model of turbulence, which were performed by D.Gaitonde M.Visbal and J.S.Shang in Air Force Research Laboratory Wright-Patterson AFB (Ohio, USA) [12, 13, 41] is performed. To explain the additional topological peculiarities of the flows considered, which were obtained in calculations, and to refine the results of previous studies [14] under the conditions of hypersonic velocities for $M_\infty = 8.3$, we used the experimental data for the Mach number $M_\infty = 5$ obtained by A.Zheltovodov and E.Schuelein at the DLR Institute of Fluid Mechanics (Goettingen, Germany) [33].

The second part contains a more detailed description of new experimental data obtained by A.Zheltovodov and E.Schuelein at DLR Institute of Fluid Mechanics (Goettingen, Germany) [33] for the Mach number $M_\infty = 5$ and deflection angles of the side surfaces of the fins $\beta = 8$, 12, 18, and 23° for the purpose of their subsequent use to verify CFD codes.

1. ANALYSIS OF EXPERIMENTAL AND COMPUTATIONAL DATA FOR SYMMETRIC CROSSING-SHOCK-WAVES/TURBULENT BOUNDARY LAYER INTERACTIONS UNDER SUPERSONIC AND HYPERSONIC SPEED CONDITIONS

1.1. Test Model, Test Conditions and Experimental Techniques

Supersonic crossing shock wave/turbulent boundary layer interactions data described on the first stage of the studies in [3, 5, 6] have been used for a detailed comparison with the results of numerical calculations. The experiments were conducted in the supersonic wind tunnel T-333 based at ITAM SB RAS for the following test conditions:

Mach number M_∞	3.92 ± 0.03
Stagnation pressure P_t, MPa	1.48 ± 0.02
Stagnation temperature T_t, K	260 ± 2
Reynolds number Re_1, m^{-1}	$(89 \pm 4) \cdot 10^6$
Boundary layer thickness δ, mm	3.5
Displacement thickness δ_1, mm	1.12
Momentum thickness θ, mm	0.128

The model was a flat plate with two symmetrically mounted fins, which had a sharp (~0.1 mm thick) leading edge (Fig. 1.1, *b*). The fins were 100 mm high and 192 mm long. The vertices of the fins were located at a distance of 210 mm from the leading edge of the plate, which ensured a developed turbulent boundary layer of thickness δ upstream of the fins under the conditions of adiabatic surface. Configurations with fins angles $\beta = 7$, 11, and 15° were experimentally studied. For these variants of the model, the width of the channel entrance was $A = 71.5$, 75.6, and 79.1 mm, respectively. The size of the constant-width section of the channel was identical in all cases and equal to $B = 32$ mm.

The pressure orifices 0.5 mm in diameter were located in four sections: one longitudinal section along the axis of symmetry of the plate and three cross-sections at distances of 46, 79, and 112 mm from the leading edges of the fins, which corresponds to $x/\delta = 13.14$, 22.57, and 32.0. The pressure on the plate surface was measured by silicon integral membrane gages and group registering manometers GRM-2 of class 0.5 (with the range of 0 – 0.1 MPa). The error of pressure measurement was ± 0,5%, and the maximum error of the relative quantity P/P_1 did not exceed 10%. (Hereinafter P_1 is the pressure on the plate in an undisturbed flow for $x = 0$ mm). The limiting streamlines on the model surface under adiabatic conditions were visualized using the mixture of lampblack and transformer oil. The surface temperature was controlled by thermocouples. We consider below the quantitative schemes of the limiting streamlines obtained by computer processing of photographs (see papers [3, 5]). Experimental techniques are also described in these papers in more detail.

1.2. Theoretical Model

The numerical calculations were conducted in Air Force Research Laboratory Wright-Patterson AFB (Ohio, USA) on the basis of the full 3-D mean compressible Navier-Stokes equations in strong conservation form and mass-averaged variables. A detailed description of the numerical method and numerical scheme can be found in [12, 15]. The inviscid flluxes were evaluated to nominal third order accuracy with Roe's flux-difference split scheme with a limiter for monotonicity. Viscous terms were differenced to second-order accuracy in a central manner. The effects of turbulence were incorporated through the eddy viscosity, μ_t, assumption and the turbulent Prandtl number was assumed constant at 0.9. The turbulence model employed to derive μ_t is based on the $k - \varepsilon$ equations [16] with low Reynolds number terms and incorporating a compressibility correction.

The boundary conditions are summarized as follows: on solid surfaces, the no-slip condition is enforced, the wall temperature is specified based on experiment and the

normal pressure gradient, k and ε are all assumed zero. The incoming boundary layer profile was specified at a distance of 4δ ($\delta = 3.5$ mm) upstream of the fin leading edges, *f.l.e*, by matching the momentum thickness (θ = 0.128 mm at the *f.l.e*) with 2-D calculations. The downstream and top boundaries are simulated to be far enough away for the application of simple zero-gradient extrapolation.

The grid was generated as a sequence of non-uniform Cartesian planes normal to the direction of the upstream flow. The clustering was designed to resolve not only the boundary layers and shock-waves but also the secondary features of the interior vortical flowfield. Guideline has been taken from extensive previous experience with the present model at field parameters similar to the present [12, 13, 17, 18]. Based on these studies, 123 points was employed in the streamvise direction, 88 points normal to the plate and 109 points in the spanwise direction. For considered symmetric cases only half the domain was computed.

1.3. Comparison of Computations with Experimental Data

For all cases under consideration, the flow at the entrance to the channel formed by two fins is determined by the interaction of swept shock waves generated by the fins and a turbulent boundary layer on the plate. As it follows from the experimentally registered pattern of the limiting streamlines for $\beta = 7°$ (Fig. 1.2, *a*), a local (singular) separation appears immediately ahead of the vertices of the fins, and the separation lines S_1 and S_2 emanating from saddle points rather rapidly degenerate to finite-width convergence regions slightly higher than the traces of the shock waves corresponding to inviscid flow (they are shown by the dashed curve). The streamlines in these regions begin to curve in the region of the beginning of pressure growth (the dash-dotted curve) and asymptotically approach each other to form a narrow region of parallel flow in the direction toward the channel axis. To simplify the patterns in the regions of dense concentration of the streamlines, some of them are deliberately terminated. A characteristic throat is formed above the calculated point of intersection of the shock waves. Practically all the limiting streamlines captured by the inlet section of the channel penetrate through this throat without any signs of separation. The interaction of intense secondary flows propagating from the divergence lines R_1 and R_2 and the flow passing through the throat results in the formation of secondary convergence lines S_3 and S_4. The limiting streamlines penetrating through the throat tend to diverge in the vicinity of the point of the first intersection of «inviscid» shock waves and then converge again to some central asymptotic convergence line together with secondary lines S_3 and S_4 that cover this region.

The pattern of the limiting streamlines on a flat plate obtained for the configuration considered in calculations [41] (Fig. 2, *b*) is qualitatively similar to the picture registered in experiment. At the same time, we should note a smaller width of the flow penetrating through the throat near the channel centerline and the absence of the secondary convergence lines S_3 and S_4 (see Fig. 1.2, *b*). The calculated isolines of the relative surface pressure (Fig. 1.2, *c*) illustrate some additional features of the flow. It is seen that the greatest increase in pressure is observed in the region of the flow penetrating near the centerline. The pressure distributions along the channel centerline versus the relative longitudinal coordinate $X = x/\delta$ (Fig. 1.2, *d*) and versus the coordinate $Z = z/\delta$ measured

from the axis in cross-sections I, II, and II shown in Fig. 1.2, *a, c* for $X = 13.14$, 22.57, and 32.0 (Fig. 1.3, *a*) demonstrate a good agreement with experiment.

Detailed numerical data [12] for the field of various parameters and spatial gas dynamic structure of the flows considered allow one to refine the specific features of their evolution at different strengths of shock waves generated by the fins. Figure 1.4, *a* shows some specific features of the flow in the vicinity of the vertical plane of symmetry for the case under consideration for the fins angles $\beta = 7°$. The lines shown in the plane of symmetry were obtained by crossing the streamlines by this plane. The limiting streamlines are shown on the horizontal surface of the plate. Two regions of condensation of the limiting streamlines on the plate can be clearly seen. The first region is located along the continuation of the primary convergence line S_2, and the second region is located downstream and oriented almost parallel to the plane of symmetry. In these regions, the emergence of the above-described secondary convergence lines S_3 and S_4 for greater angles β. In the case under consideration, a clearly seen line of convergence (separation) S_2 was registered both in calculations and experiments only near the fin vertex. At a distance from it, this line gradually degenerates to a finite-width convergence region. The lines in the plane of symmetry indicate that the flow is displaced from the plate surface under the action of the opposite pressure gradient, which occurs without any signs of separation and reverse flow caused by the latter. The numerical data presented in [12] indicate a significant thickening of the boundary layer in the direction toward the centerline and a greater height of the total pressure loss zone between the divergence lines R_1 and R_2 (see Fig. 1.2, *a*).

The experimental patterns of the limiting streamlines on the side surfaces of the fin show a local region of 3-D separation bounded by the lines of convergence S_5 and divergence R_5 at a certain height from the base at the point of incidence of secondary «inviscid» shock waves reflected from the plane of symmetry immediately ahead of the inflection of the side surface (Fig. 1.5, *a*). In the case of symmetric interactions considered, the flow patterns on the surfaces of both fins were almost identical. In this connection, the schemes for only one (upper) fin are presented in what follows. Its surfaces are developed into one plane. There is no separation of the boundary layer on the side surface near the plate, and the limiting streamlines are only slightly curved in the vicinity of the boundaries of the system of compression waves shown by dashed curves. These compression waves are formed at the base of the shock wave incident onto the surface in the course of its interaction with the boundary layer on the plate [3, 5, 12]. In the case under consideration, the strength of these waves is insufficient to cause the boundary layer separation. In calculations, a small-scale separation on the side surface was not registered, and only a typical curvature of the limiting streamlines that precedes the separation is observed (Fig. 1.5, *b*).

It follows from the experiment that, as the fin angles increase to $\beta = 11°$ (Fig. 1.6, *a*), the convergence regions previously existing at a certain distance from the leading edges of the fins transform to the convergence (separation) lines S_1 and S_2, and the divergence lines R_1 and R_2 become more definite. These features indicate a gradual transformation of secondary flows in the vicinity of the fins to separated flows and the growth of strength of transverse flows directed to the axis. The throat formed between the lines S_1 and S_2 becomes narrower, the flow expanding behind this throat and directed

along the centerline is terminated above the point of the first intersection of the «inviscid» shocks with the subsequent formation of the longitudinal divergence line R_3 of finite length along the flow. This divergence line gradually degenerates to a dividing streamline in the region of meeting of transverse flows. The secondary convergence lines S_3 and S_4 propagate more upstream toward the fin vertices than in the previous case. The flow character at the constant-width channel entrance is partly determined by the influence of expansion waves propagating from the points of inflection of the side surfaces of the fins. They are clearly seen on the surface pressure isolines obtained in calculations (Fig. 1.6, *c*). The influence of these waves favors a more intense motion of the near-wall flow toward the fin surfaces and stimulates the formation of the convergence lines S_7 and S_8. The shock wave reflected from the fin surfaces (Fig. 1.6, *a*, *c*) initiate the opposite pressure gradients and cause a deflection of the limiting streamlines to the channel centerline.

The calculated picture of the limiting streamlines (Fig. 1.6, *b*) reproduces qualitatively the characteristic features of the flow considered. At the same time, similar to the previously considered case $\beta = 7°$, a significantly smaller width of the flow penetrating through the throat in the vicinity of the centerline and the regions of the flow diverging from the divergence line R_3 are worth noting. The signs of the secondary convergence lines S_3 and S_4 appear in the calculations much more downstream that in the experiment.

The character of the surface pressure isolines (Fig. 1.6, *c*) indicate the growth of the opposite pressure gradient in the flow penetrating into the channel. A comparison of numerical and experimental data on pressure distribution along the channel centerline (Fig. 1.6, *d*) and in cross-sections I, II, and III (see Fig. 1.3, *b*) shows their good agreement for $X < 24$. For $X > 24$, however, the calculations tend to overestimate the value of the pressure level near the centerline, and the second maximum at $X \approx 43$, which was observed in experiments, was not registered in calculations (Fig. 1.6, *d*). The character of pressure distributions in cross-sections I, II, and III (see Fig. 1.3, *b*) is qualitatively similar to those considered previously for $\beta = 7°$, but the pressure levels are noticeably higher. The maxima observed in the vicinity of $Z \approx \pm 2.3 - 2.5$ in cross-section III correspond to the divergence lines R_1 and R_2 near the fins.

In the case under consideration $\beta = 11°$, vast 3-D separation regions bounded by the lines S_9 and R_9 (see Fig. 1.5, *c*) were observed in the experiment on the side surface of the fins in the region of incidence of the shock waves reflected from the axis behind the first inflections of the surfaces (Fig. 1.6, *a*). The behavior of the limiting streamlines allows us to assume the presence of singular points of the saddle C_2 and focus F_1 types. These features are more clearly seen in the next stage of development, which is analyzed in what follows. The calculated pattern of the limiting streamlines (Fig. 1.5, *d*) is close to the experimental results.

Figure 1.4, *b* shows the specific features of the flow near the vertical plane of symmetry, which were obtained in calculations for the case being analyzed. As already noted, the growth in strength of the crossing shock waves increases the length of the convergence line S_2 on the plate. In the vicinity of the plane of symmetry, however, this line curves and turns almost parallel to the centerline. The intensity of convergence of the ambient flow to this line decreases. All the limiting streamlines propagating from the free

stream penetrate into a narrow gap between S_2 and the centerline. The limiting streamlines located to the other side of S_2 also turn downstream under the influence of the reflected separation shock (1) formed upstream of the line S_2 [12]. This turning flow forms the secondary separation line S_4. The bulging of the boundary layer above the surface with the formation of a shear layer (2) is observed in the plane of symmetry. The line of divergence (bifurcation) *LB* arises beneath this shear layer. This line indicates that the flows that propagate from the fins and intersect reach the plane of symmetry. Below the bifurcation line, the flow attaches to the plate along the divergence line R_3 and forms longitudinal vortices. In accordance with the numerical data [12], such a character of the flow with increasing fin angles favors a further growth of the height of the near-wall region of significant total pressure losses, which extends over the channel width to the divergence lines R_1 and R_2 (see Fig. 1.6, *a, b*).

The pattern of the limiting streamlines on the plate obtained in experiment for the angles $\beta = 15°$ (Fig. 1.7, *a*) clearly indicates the separation not only in the regions adjacent to the fins, but also in the flow penetrating along the channel centerline through a narrow throat that still remains between the lines S_1 and S_2. This is evidenced by the appearance of the singular saddle point C_1 significantly higher than the first intersection of "inviscid" shock waves, and by the reverse flow propagating to this point along the axis. Another singular node point N_1 was observed further downstream (see [3, 5]). The central large-scale separation region is bounded by the convergence lines S_5 and S_6. The secondary separation lines S_3 and S_4 propagating from the fins are strongly curved by their interaction with the separation shock waves reflected from the axis. After that these lines merge with the lines S_5 and S_6 approximately in the middle of the central separation region and are entrained downstream along the centerline. Additional separation lines S_7 and S_8 are clearly seen on the plate surface behind the inflections of the side surfaces. The character of the calculated surface pressure isolines (Fig. 1.7, *c*) confirm the assumption, which was previously made in [3, 5], that the appearance of these separation lines is favored by additional terminal shock waves caused by flow overexpansion in expansion waves propagating from the deflections of the fins.

The pattern of the limiting streamlines on the plate, which was obtained in calculations for the case considered, is qualitatively similar to the specific features observed in experiment, but also reveals a number of significant topological differences (Fig. 1.7, *b*). Thus, for example, the separation lines S_1 and S_2 upstream of the fins do not form a typical throat and intersect in the singular node point N_1 which is associated with the separation point of the flow propagating along the centerline. This is more clearly shown qualitatively in an enlarged fragment in Fig. 1.7, *c*. As in experiment, the second node point N_2 is observed further downstream. Additional features, which were not registered in experiment, are two saddle points C_1 and C_2 located symmetrically about the centerline. As previously, it is worth noting that the calculations do not reveal the signs of the secondary separation lines S_3 and S_4 propagating from the fins, and also the additional separation lines S_7 and S_8 in the flow behind the inflections of the side surfaces (see Fig. 1.6, *a-c*). The central separation region bounded by the lines S_5 and S_6 is more compressed by the flows propagating from the fins and noticeably smaller in width in calculations than in experiment. This is particularly well seen in the vicinity of the point N_2 and upstream of it. These features testify that the near-wall secondary flows

propagating from the divergence lines R_1 and R_2 to the centerline, which were observed in calculations, have a better ability to overcome the adverse pressure gradients without separation that the real flows.

The calculated pattern of pressure isolines on the plate (Fig. 1.7, *d*) characterizes the features of the flow formed in the process of a strong viscid-inviscid interaction. The maximum levels of pressure are observed near the channel centerline and behind the points of reflection of the secondary shock waves from the side walls on the constant-width section. The pressure distribution along the centerline (Fig. 1.7, *e*) is characterized by the presence of a plateau region at $X \approx 14 - 18$, which is typical of developed separated flows. A comparison of numerical and experimental data on the pressure distribution shows that the calculated level of pressure is noticeably overestimated for $X > 18$. At the same time, the calculation correctly predicts the rapid decrease of pressure because of the influence of expansion waves propagating from the inflections of the side walls, the intermediate maximum, and the repeated growth caused by a sequence of reflected shocks and expansion waves.

A comparison of numerical and experimental data on pressure distributions in cross-sections I, II, and III shown in Fig. 1.7, *a*, *c* demonstrates their good agreement, except for some region near the centerline (see Fig. 1.3, *c*). A pressure maximum is formed in cross-section I in the flow compressed near the centerline. The pressure level dramatically increases toward the fins. The region of maximum pressures near the centerline in cross-section II coincides with the central separation region. The pressure minima at $Z \approx \pm 1.7$ correspond to the convergence lines S_1 and S_2 that cover this separation region (see Fig. 1.7, *a*), and additional maxima are formed at the points with the coordinates $Z \approx \pm 2.9$ in the vicinity of the divergence lines R_1 and R_2. In cross-section III, the maximum pressure is observed at the centerline, it dramatically decreases to minima at $Z \approx \pm 3$ under the action of expansion waves propagating from the fins, and increases again with the formation of noticeable maxima at $Z \approx \pm 3.4$ in the vicinity of the shock waves that arise behind the fins.

Taking into account the above differences in the topology of the limiting streamlines on the plate, which are obtained in calculations and experiments for $\beta = 11°$ and 15°, it seems of interest to perform a more careful analysis of the specific features of evolution of the flows under consideration with a gradual increase of the angle within this range. The conducted numerical studies show that, as β increases, at some point $11° < \beta < 15°$ the first pair of singular points N_1 and C_1, in which the surface friction turns to zero, appears for the first time on the plate (see the fragment in Fig. 1.4, *c*). This flow pattern is also observed in some other cases, for example, in an asymmetric interaction near the fins with the angles $\beta_1 = 11°$ and $\beta_2 = 15°$ [12], and also in 3-D interactions in the flow formed by three compression surfaces [19] and in the flow around a cylinder with a flare [15]. Under the conditions under consideration, the separation line S_2, as in previous patterns, turns along the flow near the plane of symmetry, but is terminated in the singular node point N_1 at the centerline itself. Further downstream a saddle point C_1 is formed. In the plane of symmetry, the node N_1 corresponds to the saddle point c^1, and the point C_1 is associated with the node n^1, which acts as a source of fluid under the separated boundary layer. The bifurcation line *LB* emanates from the point n^1 and, as previously, indicates that the opposing flows propagating from different sides of the plane of symmetry reach this

plane. An interesting difference with the case of a 2-D separated flow is that in this case the separation occurs both at the point c^1 and at the point n^1.

As the fin angle increases to $\beta = 15°$, the saddle point C_1 located previously on the plate (see Fig. 1.4, *c*) moves from the centerline and forms two symmetric saddle points C_2 located on different sides from it, and the node N_2 appears instead of the saddle point (see Fig. 1.4, *d*). Correspondingly, the point n^1 in the plane of symmetry leaves the plate and forms an internal stagnation point in the form of a focus, and its place is occupied by the saddle c^2. As was shown in [5, 17], a similar flow pattern is observed in calculations if different models of turbulence are used. At the same time, following the experimentally obtained scheme of the limiting streamlines (see Fig. 1.7, *a*), it is possible to imaging another topological pattern of the flow (see Fig. 1.4, *e*). The separation line S_2, not reaching the plane of symmetry and forming a throat, propagates downstream and is displaced by the near-wall flow diverging from the centerline. The flow penetrating through the throat separates from the plate in the saddle point C_1 rather than in the node, as obtained in calculations. In fact, this point is analogous to the stagnation point that appears ahead of the circulation region induced by breakdown of the longitudinal vortex or axisymmetric wake under the conditions of their interaction with the shock wave (see, e.g., [20]). All the limiting streamlines on the plate behind the line S_2 are strongly curved in the separated shock wave (1) reflected from the centerline and propagate downstream. The transverse flow formed directly above the plate does not penetrate into the central separation region and does not terminate the convergence line S_6, as it is observed in calculations. The flow penetrates into the separation region through the layers located above the surface in the vicinity of the bifurcation line *LB*, where the flow structure and its topological features in the plane of symmetry are similar to those obtained in calculations.

Analyzing the noted differences between the calculation and experiment, we can assume that the main reason for them is the complexity of a correct reproduction of the state of flows in the regions of turbulent separation in calculations. For example, it was experimentally found [21] that the reverse flow in separation regions ahead of two-dimensional obstacles can be laminar. The numerical studies [22, 23] conducted using the $k-\omega$ turbulence model showed that the scale of separation and the surface skin friction and heat transfer distributions can be satisfactorily predicted only by reaching this state by controlling the balance between the production and dissipation of turbulence. Similarly, it was experimentally demonstrated [24–27] that the reverse flow propagating from the divergence line in the vicinity of a single vertical fin in the case of 3-D interaction can be also laminar under certain conditions. The calculations based on the modified algebraic Baldwin-Lomax model [28, 29] showed that the secondary separation appears only in modeling of this state of the flow (see Fig. 1.8, *a*), and a good agreement with experiment is achieved for the distributions of various parameters, including surface skin friction. The use of the standard Baldwin-Lomax model led to the turbulization of the reversed flow, disappearance of the secondary separation (Fig. 1.8, *b*), and a noticeable disagreement with the experiment. These conclusions are in line with the experimental studies [27] which demonstrated a possibility of suppressing the secondary separation near the fin by turbulizing the reverse flow using sand roughness.

Finally, the authors of [29] describe the flow around two fins with the angles $\beta = 15°$ calculated using the modified Baldwin-Lomax model, which is similar to the flow considered above. The resultant pattern of the limiting streamlines (Fig. 1.8, *c*) is a good reproduction of the specific features of the behavior of the secondary separation lines S_3 and S_4 under the conditions of a laminar reversed flow, the scale of the central separation region, and the pressure distribution along the centerline (Fig. 1.8, *d*, solid curve), which were observed in the present experiments (see Fig. 1.7, *a*) and in [30]. At the same time, in regions between the lines S_1 and S_3, and also S_2 and S_4 (Fig. 1.8, *c*), the near-wall secondary flows propagating from the fins penetrate into the central separation region to form the node N_1 at the centerline and two singular points C_1 and C_2 located symmetrically relative to the node point, like in the present calculations (Figs. 1.4, *d* and 1.7, *b, c*), which was not registered in experiment. A noticeable difference with the experiment is also observed in skin friction distribution along the centerline (Fig. 1.8, *e*). As noted previously in [25], based on the concept [24], we can assume that the transition from the laminar to turbulent state can occur only if the secondary flows in the mentioned regions are rather extended. After reaching this state, we can expect the emergence of additional features predicted by calculations. According to experimental studies [27], these secondary flows include a laminar boundary layer flowing down from the side surfaces of the fins immediately behind their vertices onto the plate (see the character of the limiting streamlines in Figs. 1.5 and 1.8). This favors a decrease of the initial level of disturbances in the flow propagating to the centerline. At the same time, as it follows from [28, 29], a flow with an elevated turbulence is almost immediately observed in these regions in calculations. Apparently, the advanced calculations based on the above-considered approaches with the use of various models of turbulence do not allow a fully adequate modeling of the flow state in the complex situations of 3-D interaction that are considered. Taking into account the experimentally registered effects of amplification of turbulence in shock waves, attenuation of turbulence in expansion waves, flow relaminarization in separation regions, and a possibility of the repeated laminar-turbulent transition in secondary flows under the conditions of conical sub- and supersonic velocities (see, e.g., [26, 27, 31, 32]), this problem seems to be rather complicated and requires further improvement of advanced numerical methods.

It should be noted that the experimental studies of 3-D crossing shock wave/turbulent boundary layer interactions at the Mach number $M_\infty = 5$ [33] allowed one to obtain a pattern of the limiting streamlines similar to the calculated pattern (Figs. 1.4, *d* and 1.7, *b, c*) for the case $\beta \geq 18°$ (Fig. 1.9, *d*). It was found that, apart from two symmetric saddle points C_1, C_2 and the node N_2, the saddle point C_0 is still formed instead of the node point N_1 in the beginning of the central separation region, and two additional foci F_1 and F_2 symmetrical about the centerline are located immediately behind it. This scheme, as well as the previously considered patterns, corresponds to the known topological rule [34], according to which sadlle points are balanced by nodes and foci. It is also essential that, as the angle β decreases, the patterns of the limiting streamlines transform in a complex way (Figs. 1.9, *a–c*) and for $\beta = 8°$ and 12° (see Figs. 2.6, 2.7) they become similar to those shown in Figs. 1.2, *a* and 1.6, *a*, respectively. The results obtained for $M_\infty = 5$ are considered in more detail in the second part of the report.

As noted in [5], the pattern of the limiting streamlines at the stage of incipience and development of intermittent separation with surface skin friction coefficient close to zero at the centerline is determined to a large extent by the influence of unsteady effects typical of real flows. Under these conditions, the lampblack-oil mixture gives almost no response to the reverse flow that exists for a very small time and cannot correctly register the lines or points of separation. Their appearance is observed at a later stage of the incipience of a steady separation when the reverse flow exists for more than 50% of time, which corresponds to the intermittency factor $\gamma > 0.5$. Probably, exactly these features are manifested for $\beta = 11°$ (Fig. 1.6, *a*), where the flow behind the expected point of separation at the centerline has the same direction as the incoming flow. Under these conditions, the longitudinal divergence line R_3 is formed in this region at the background of increasing pressure. The picture described here was clearly registered in [5] for a similar configuration for $M_\infty = 3$. Taking into account the unsteady intermittent character of real turbulent flows in the vicinity of separation lines and points even under the conditions of steady separation [35], the above-noted difference between the numerical and experimental patterns of the limiting streamlines and topological schemes seems quite understandable, since the approached considered do not model unsteady effects. Possibly, these effects can be described on the basis of direct numerical simulation (DNS) or large eddy simulation (LES) (see, e.g., [36–39]), but the use of such approaches for high Reynolds numbers is difficult at the moment because of limited capabilities of modern computers.

Considering the numerical and experimental patterns of the limiting streamlines on the side surfaces of the fins for $\beta = 15°$, $M_\infty = 3.9$ (Fig. 1.10, *a*, *b*), we can state that they are in good agreement. The formation of vast separation regions bounded by the lines of convergence S_9 and divergence R_9 was experimentally observed in the region of incidence of the shock wave behind the surface inflection. An additional pair of singular points C_3 and N_2 was registered near the fin base, along with the saddle point C_2 and the focus F_1. Similar features are manifested in calculations. The flowfield detailes in this region are depicted in Fig. 1.11. A thin boundary layer on the side surface of the fin separates along the line S_9, and the contour of the separation region is shown as surface 1. The near-wall flow directed to the fin base below the points C_2 and N_2 separates and forms longitudinal vortex 2. The appearance of such a vortex in the vicinity of an isolated fin was previously registered in [40]. A vortex originating at the base rises above the surface from the focus F_1, the flow along this vortex propagates upwards. According to the numerical data [12], the separation region bounded by surface 1 and vortex flow 2 at the fin base are characterized by appreciable losses of the total pressure.

Based on the above considerations, we can refine some results of [14, 42], in which the authors studied the crossing-shock-wave/turbulent-boundary-layer interaction for the Mach number $M_\infty = 8.3$. Thus, for instance, Figures 1.12 and 1.13 show the photographs of the limiting streamlines borrowed from [14] and the corresponding patterns, which characterize qualitatively the orientation of some of these lines for the fins angles $\beta = 10°$ and 15°. A low quality of the photographs did not allow the authors of this paper to show the specific features of the flow patterns obtained. An additional analysis of the photograph of the limiting streamlines for $\beta = 10°$ (Fig. 1.12, a) indicates that this pattern is similar to that considered above for the case $\beta = 7°$ and $M_\infty = 3.9$ (see Fig. 1.2, *a*). The

photograph shows the convergence lines S_1 and S_2 propagating from the fin vertices, the divergence lines R_1 and R_2 formed near the fin bases, and the secondary convergence lines S_3 and S_4 that arise when the secondary flows propagating from the fins interact with the flow passing along the centerline.

The qualitative features of the flow for $\beta = 15°$ (Fig. 1.13, *a*) are, probably, close to those shown in Fig. 1.6, *a* for $\beta = 11°$ and $M_\infty = 3.9$. In this case, the flow along the centerline penetrated through a narrow throat between the lines S_1 and S_2 without the signs of singular points typical of the developed separation, and the longitudinal divergence line R_3 appear further downstream. The secondary convergence lines S_3 and S_4 propagate almost to the fin vertices. The calculations [43] obtained using the Rodi model of turbulence with two equations (Fig. 1.14, *b*) are in better agreement with experimental data that the calculations based on the algebraic Baldwin-Lomax model (Fig. 1.14, *a*), whose typical features are the disappearance of the throat and the appearance of singular points at the centerline. At the same time, the signs of the secondary separation lines S_3 and S_4 disappear in the both types of calculations toward the fin vertices, in contrast to experiment. The analysis of a great body of numerical data for the flow under study [18, 43–47] indicates that the models of turbulence exert a significant effect on the quality of calculations and it is necessary to seek for the methods of adequate modeling of the state of secondary flows propagating from the fins.

2. DOCUMENTATION OF EXPERIMENTAL DATA FOR HYPERSONIC CROSSING-SHOCK-WAVES/TURBULENT BOUNDARY LAYER INTERACTIONS

The experimental studies presented in this chapter of report have been carried out by A.Zheltovodov and E.Schuelein at the DLR Institute of Fluid Mechanics (Goettingen, Germany) and briefly described in [33]. The data for crossing-shock-waves/turbulent boundary layer interactions are presented here in a convenient form to be used for CFD code validation.

2.1. Windtunnel Facility, Test Conditions and Test Model

The experiments were conducted in the supersonic/hypersonic Ludwieg-Tube (RWG) of DLR at Goettingen. This facility (Fig. 2.1) covers a Mach number range of $3 \le M_\infty \le 7$ and a unit Reynolds number range of $5 \cdot 10^6$ m$^{-1} \le Re \le 80 \cdot 10^6$ m^{-1}. The facility consists of an 80-meter long storage tube used as pressure reservoir which is separated from the nozzles and the test section by a fast-responce gate valve. The tunnel is started by opening this valve. The test section for the Mach numbers $M_\infty = 3$ and 4 has a cross section $0{,}5 \times 0{,}5$ m^2, while those for high Mach numbers have circular sections of 0,5 m diameter. A run time of the facility $\approx 0{,}3 - 0{,}4$ seconds. The test gas is pre-heated by heating the storage tube wall electrically in order to avoid condensation during the strong expansion in the nozzle. Additional details of the design and the operation of the RWG are given in [48].

The experiments described in this chapter were carried out at nominal conditions, which are listed below with indicated run-to-run variations of flow parameters:

Nominal Mach number:	$M_\infty = 5$
Reynolds number:	$Re_1 = 41{,}9\ (\pm 1) \times 10^6\ m^{-1}$
Total pressure:	$P_t = 2210\ (\pm 10)$ kPa
Total temperature:	$T_t = 427\ (\pm 6)$ K
Wall temperature:	$T_w = 295\ (\pm 5)$ K

The sketches of four basic test model configurations used for the crossing-shock experiments as well as the coordinate system are shown in Fig. 2.2 together with the Table 1, where their typical sizes are indicated. The model consists of two fins, each at angle of attack β, mounted on a vertical flat plate. All the fins had sharp (~0.1 mm) leading edges and the height $H = 100$ mm. The side faces of basic fins ("short fins") with the angles $\beta = 8$, 12 and 18° (Fig. 2.2, *a*) had the inflected generatrices with a constant-width channel behind inflection. For these basic variants the width values of the channel entrance were $A = 142$; 161,5; 196 mm and the size of the constant-width channel section was the same in all cases $B = 100$ mm (see Fig. 2.2, Table 1). The values of the distance between the plate and fins leading edges for these test configurations correspondingly were $L = 229{,}5$; 249,5 and 269 mm.

The last basic configuration with $\beta = 23°$ had the flat side faces ("long fin", Fig. 2.2, *b*) and it typical sizes are presented also in Table 1 (Fig. 2.2). The width of the channel entrance was $A = 307$ mm, the distance between the trailing edges of fins sides faces $B = 100$ mm and the distance between the plate and fins leading edges $L = 286$ mm.

The fin pairs could be easily moved in the x and z direction and the widths A and B changed. Some examples of the surface flow pattern visualization are additionally considered below for the $\beta = 18°$ configuration at different B (and A) values: $B = 38{,}4$; 43,2 and 64 mm ($A = 134{,}4$; 139,2; 160 mm).

A possibility of fins rotation around the points C (Fig. 2.2, *a*) have been used to change β values in some narrow range for the basic ($\beta = 18°$) configuration. The examples of surface flow pattern visualization for $\beta = 16$, 17 and 17,5° cases are considered additionally at constant width between points C: $B = 100$ mm (see Fig. 1.9).

143 static pressure taps were located on a plate between the fins with interval 10 mm in the x and z directions. The first horizontal taps line located 370 mm downstream of the plate leading edge. To obtain continuous data throughout interaction region, the fin pairs were moved 5 mm in the x and z directions.

The local freestream and incoming turbulent boundary layer properties on the flat plate were determined from pitot and static pressure surveys in [49, 50]. They were measured along a plate centerline in 5 positions (at different distances x_0 from a plate leading edge) in a streamwise direction (Table 2). The velocity profiles obtained from these surveys were transformed into incompressible coordinates using the Van Driest II transformation and compared with law of the wall [49]. The comparison has verified a turbulent state of the boundary layer in the interaction region for the fin flows being

investigated. The skin friction measurements discussing below support additionally such conclusion.

Table 2. Documentation of undisturbed turbulent boundary layer properties

x_o, mm	M_e	δ, mm	δ_1, mm	θ, mm	$C_{f\,prof}$ *	$C_{f\,VD}$ **
266	4.961	3.814	1.576	0.157	0.001382	0.001340
296	4.973	4.175	1.788	0.177	0.001296	0.001302
316	4.989	4.410	1.792	0.177	0.001324	0.001283
336	4.976	4.658	1.894	0.189	0.001324	0.001280
356	4.984	4.813	2.000	0.202	0.001311	0.001268

* $C_{f\,prof}$ – skin friction coefficient, obtained on the basis of mean velocity profiles (a least-squared curvefit of the wall-wake law for transformed velocity profiles to the corresponding "incompressible" flow);

** $C_{f\,VD}$ – skin friction coefficient, calculated from Van Driest II equation.

2.2. Instrumentation and Technique

2.2.1. Surface Skin Friction Measurements

The skin friction data on a plate surface upstream of the interaction region (Table 2) have been obtained in [49, 50] from the measured mean velocity profiles by an application of the combined wall–wake law with the Van Driest mixing-length damping function for the viscous sublayer to the corresponding transformed "incompressible" flow. This technique is well known and described in [51]. The Van Driest II formula has been used also to obtain wall skin friction coefficients (C_{fVD}) for comparison.

Additional skin friction measurements have been carried out using the Global Interferometer Skin Friction (GISF) meter. This technique proposed in [52] overcomes many well known limitations of other existing methods, since it provides non-intrusive skin friction measurements. It is based on the relationship between the thinning of an oil film, placed on the test surface exposed to the flow, and the local surface shear. The rate of thinning of the oil film is determined using optical interference arising when an incident light beam is partially reflected from the oil and test surface. The surveys of different modern realizations of such a technique are presented in [50, 53].

The used version of the GISF meter was described in [53, 54]. The optical scheme (Fig. 2.3) realized before in the Ludwieg-Tube (RWG) [49, 50] was applied. The beam from a 2 mW, 633 nm wavelength He-Ne laser was widened by the lenses and sent with a mirror to the test surface with the thin oil film. Because of very short test times in the facility, the interferograms images were recorded during a run by Sony VO-9600P video recorder and digitized thereafter by a full frame video capture card Hauppauge

Win/Motion 60 and stored on a PC's hard disk at up to 30 frames per second. Various Wacker silicon oils AK–10, AK–0.65 and Shell mineral oil S.5585 with corresponding nominal viscosity of 10 mm^2/s, 0,65 mm^2/s and 5,4 mm^2/s at 25 °C have been used. Typically, 4 to 5 high quality images were captured 40 ms apart at an image resolution of 768x576 pixels. The skin friction coefficient C_f was calculated by the integral method, described in [52, 53].

The comparison of the skin friction measurements on a plate obtained by different methods is shown in Fig. 2.4. The C_f values, extracted from the GISF measurements in [50] and present study (preliminary presented in [33]), show an adequate distribution and good agreement with the data obtained from the velocity profile measurements [49, 50] and at $x > 200$ mm agree with the well-known Van Driest II correlation for the turbulent boundary layer. At $x \leq 100$ mm the skin friction distributions show a transitional boundary layer. The curve for laminar boundary layers corresponds to the empirical Young correlation [55]. So, the end of natural transition occurred at about 100 mm. The comparison supports conclusion regarding the turbulent state of the boundary layer upstream of the crossing shocks interaction.

Some examples of the GISF application to the study of 3-D interaction properties are considered briefly below.

2.2.2. Surface Flow Pattern and Surface Reflection Visualization Technique

A very liquid mixture of the Shell mineral oil S.5585 with the lamp black or oil-paint has been used for the surface flow pattern visualization. The time approximately 20 – 40 ms was necessary to achieve the stable surface flow pattern properties which existed for the next 260–280 ms of the RWG facility run time without any significant changes. The movement of the mixture particles along the limiting streamlines was recorded during a run by the Sony VO-9600P video recorder. This gave a possibility of analyzing the dynamics of the topology development.

The surface reflective visualization (SRV) technique has been developed and used in the RWG [33] parallel with the surface flow pattern visualization by the oil–lamp black and C_f measurements by the GISF meter for the 3-D shock waves/turbulent boundary layer interactions. This technique is similar in some details with one described in [56]. The SRV system is a derivative of a double-pass shadowgraph system in which the model surface itself is a mirror and a component of the optical system (Fig. 2.5, *a*). A parallel bundle of light was directed into the test section along a path perpendicular to the surface of the model. The light is reflected back along nominally the same path and brought to focus on the image plane of CCD camera. Such an optical system produces a two-dimensional image of a component of the density gradient existing perpendicular to a parallel light bundle integrated over its path. An example of the crossing shock wave structure and the oil-lamp black surface flow visualization in the vicinity of double fin configuration (β = 18°, A = 139,2 mm, B = 43,2 mm) is shown in Fig. 2.5 *b*. The appearance of a 3-D central separated zone around the crossing shock waves is seen distinctly.

2.2.3. Surface Pressure Measurements

143 static pressure taps were located on a plate with interval 10 mm in the x and z directions. The taps were 0,3 mm in diameter and connected with short-length tubing (150 mm) to a 32-port PSI ('PRESSURE SYSTEMS INC') pressure transducer modules with a measurements rate of ±15 psi (±103400 Pa) and a rated accuracy of ±0,1% full scale (±100 Pa) or better. Two such modules have been used in every run.

The measurement error of surface pressure P_1 in undisturbed flow was ±2÷2,5%, and the maximum error of the relative quantity P_w/P_1 did not exceed ±5%. The measured surface pressure distributions for basic configurations at β = 8, 12, 18 and 23° are tabulated and presented in figures in the Appendix.

2.3. Brief Description of Experimental Results at Mach Number $M_\infty = 5$

The surface flow pattern photographs on a plate between two fins for all considered configurations are presented in Figs. 2.6–2.25. The letters in the figures denote: "*S*" – convergence (or separation) lines, "*R*" – divergence (or reattachment) lines.

The limiting streamlines properties for the case $\beta = 8°$ at $M_\infty = 5$ (Fig. 2.6) are very similar to that considered above for $\beta = 7°$ case at $M_\infty = 3.9$ (Fig. 1.2, *a*). Realized flow is characterized by a smooth turning of the limiting streamlines towards the channel axis and their downstream penetration through the throat between convergence lines S_1 and S_2. Secondary convergence (separation) lines S_3 and S_4 are formed due to the interaction of intense secondary flows arising at the fin bases from the divergence lines R_1 and R_2 with the flow passing through the throat.

The surface flow pattern for $\beta = 12°$, $M_\infty = 5$ (Fig. 2.7) is close to that considered above for $\beta = 11°$ at $M_\infty = 3.9$ (Fig. 1.6, *a*). Fig. 2.8 shows an increased fragment of the photograph for this configuration, when the oil-paint mixture was applied upstream of the fins tips only (for the other surface patterns shown the mixture was also applied within the interaction region). In the vicinity of centerline the yellow point has been used. It's seen that the yellow oil-paint mixture penetrating through the throat between the lines S_1 and S_2 is excluded from further access to some central zone. Nevertheless, in the beginning of this zone (when the mixture was also applied within the interaction region) the appearance of only divergence line R_3 has been fixed (see increased fragment in Fig. 2.9, *a*) without a saddle point associated with a singular separation. The surface flow pattern properties in the vicinity of downstream part of the central zone is shown in increased fragment in Fig. 2.9, *b*.

The surface flow pattern for $\beta = 18°$, $M_\infty = 5$ is shown in Fig. 2.10. It's obvious the appearance of the distinct central separated zone in this case. Some increased fragments of the central separated zone are shown in Figs. 2.11. The influence of the distance B between the fins has been analyzed additionally in the experiments. Figs. 2.12 and 2.13 show an evolution of the surface flow pattern at B = 43.2 mm from the channel global shocking regime to a stable state regime with the local central separation zone. An interpretation of the surface flow pattern for the channel global shocking regime at

$M_\infty = 3$ has been considered in [3, 5]. The channel width increasing up to B = 64 mm stimulated quick appearance of the second regime (Fig. 2.14). It's seen that the surface flow pattern in the vicinity of the central separated zone for this situation is similar with previous one. The increased fragment of the photograph (Fig. 2.15) shows the limiting streamlines properties in the vicinity of the central separated zone entrance.

The surface reflective visualization (SRV) technique has been used for the crossing shock wave structure visualization parallel with the surface flow pattern visualization. The examples are shown in Figs. 2.16, *a*, *b* for the regimes with the local central separated zone at $\beta = 18°$, $B = 43{,}2$ and the channel global shocking regime at $\beta = 18°$, $B = 38{,}4$. The different surface flow pattern properties around the crossing shock waves are seen distinctly for these cases.

The surface flow pattern for $\beta = 23°$, $M_\infty = 5$ is shown in Fig. 2.17. The distinct secondary separation (S_3, S_4) and reattachment (R_3', R_4') lines appear in the penetrating from the fins to the centerline conical supersonic secondary flows at such conditions. The shock waves in the secondary flow in the vicinity of the secondary separation and reattachment lines initiate a distinct flow disturbance in the places of their crossing with the external boundary of the central separated zone. Fig. 2. 18 shows the surface flow pattern properties in the vicinity of the central separated zone entrance for this case. Increased fragment of this place is shown in Fig. 2.19, *b* and the oil iterferogram obtained on a basis of GISF technique – in Fig. 2.19, *a*. The distance decreasing between the interference fringes in downstream direction in the in Fig. 2.19, *a* corresponds to the region of the C_f decreasing. The increased fragment of the downstream region of the central separated zone is shown in Fig. 2.20. The interferogram and oil flow visualization photographs demonstrate the reverse flow existence in the vicinity of the central line. The surface flow pattern topology interpretation for this case is shown in Fig. 2.21, c. The region for which the interferogram is presented (see Figs. 2.20, *a*; 2.21, *b*) is indicated in Fig. 2.21, *c*. The surface flow pattern in the central separated zone after the node point N_1 is shown in Fig. 2.22. The increased fragments of the GISF interferogram and a surface flow pattern visualization photographs (Fig. 2.23) demonstrate a flow properties in a place where the secondary separation and reattachment lines S_3 and R_3 intersect the external boundary of the central separated zone S'_3.

The photographs in Figs. 2.24 and 2.25 show increased fragments of the surface flow pattern visualization for different β values in the vicinity of the central separation zone's "apex", which have been considered briefly in the chapter 1 of the report (see Fig. 1.9). The cases with $\beta = 16$, 17, 17,5 and 18° have been obtained by rotation of the fins for the basic ($\beta = 18°$) configuration around the points C (see Fig. 2.2, *a*) at the constant width between these points $B = 100$ mm. The schemes presented in Fig. 1.9 specify the stages of the flow topology development for these cases with β increasing. The formation of two convergence (separation) lines S_1 and S_2, additional secondary convergence lines S_3 and S_4 and one central divergence line R_3 has been fixed at $\beta = 16°$ (Fig. 1.9, *a*; 2.24, *a*). It was not possible to fix an appearance of the saddle-node points combination upstream of the line R_3 in the region shaded in the sketch in Fig. 1.9, *a*. The appearance and development of the local separated zone has been registered at $\beta = 17$ and 17,5° (Figs. 1.9, *b*, *c*) after the central separation line S_0. This local zone is limited upstream and downstream by two saddle points and includes two focuses. The next scheme for $\beta = 18°$ (Fig. 1.9, *d*) has

been considered above. It displays the appearance of the long reverse flow from the downstream located node N_1 to the saddle point C_0 in the center of the separation line S_0. Two shaded regions are shown in the scheme where the flow pattern interpretation is difficult.

CONCLUSION

The conducted experimental and numerical studies allowed a significant refinement of the specific features of the evolution of complex turbulent separated flows under the conditions of 3-D interaction of a sequence of crossing shocks and expansion waves with a turbulent boundary layer in the vicinity of two vertical symmetric fins with deflected side surfaces and the angles of deflection $\beta = 7$, 11, and 15°, which are mounted on a flat plate, for the Mach number $M_\infty = 3.9$. It was shows that the numerical methods based on the full 3-D Reynolds-averaged Navier–Stokes equations and the $k-\varepsilon$ model of turbulence can satisfactorily predict the specific topological features of these flows and the pressure distribution for small and moderate strengths of the shock waves under the conditions of the absence or incipience of separation. The results obtained made it possible to refine some specific features of similar flows studied previously in [14] for the Mach number M = 8.3.

To expand the data base necessary for verification of numerical calculations, the results of experimental studies [33] of symmetric interactions of the crossing shock waves and a turbulent boundary layer for the Mach number $M_\infty = 5$ and the range of fins deflection angles $\beta = 8 - 23°$ are presented in more detail.

Based on a careful analysis of the data obtained, it is shown that one of the main possible reasons for the increasing disagreement between the numerical and experimental data with the growth of the shock strength is inadequate modeling of the state of reverse and secondary flows in 3-D separation regions within the framework of the approach considered. To check the possibility of refinement of these calculations, including the prediction of surface friction and heat transfer, it is desirable to perform a more detailed study for the analysis of the influence of the balance between the turbulence production and dissipation processes on the basis of differential models of turbulence.

To analyze the joint effect of the state of the secondary flows and unsteady effects, it is necessary to use the DNS and LES methods. Taking into account the complexity of such calculations as applied to the problems considered and also the accumulated experience, it seems reasonable in the first stage to perform only the large-scale eddy simulation for moderate Reynolds numbers in order to verify the adequate prediction of the regular features of evolution of the secondary separation in the vicinity of a simpler configuration – a single fin mounted on a flat plate.

The surface skin friction and heat transfer measurements as well as deep analysis of flow topology at $M_\infty = 5$ for considered cases is recommended for a comparison with new computations as a logic next stage of the program.

ACKNOWLEDGEMENTS

The authors wish to express their sincere gratitude to Doctors D.V.Gaitonde, M.R.Visbal and J.S.Shang (Air Force Research Laboratory Wright-Patterson AFB, Ohio, USA) as well as to Dr. E.Schuelein (DLR Institute of Fluid Mechanics, Goettingen, Germany) for collaboration in a framework of this program. We would like also to acknowledge the assistance of Dr. M.S.Maurice. The studies were supported by EOARD Contract F61708-97-W0136 (monitor: Dr. C.Raffoul).

References

1. Settles G.S., Dolling D.S. Swept shock wave-boundary layer interactions – tutorial and update. AIAA Paper 90–0375, 1990, 29 p.
2. Zheltovodov A.A. Shock waves/turbulent boundary layer interactions – fundamental studies and applications. AIAA Paper 96–1977, 1996, 27 p.
3. Zheltovodov A.A., Maksimov A.I. Symmetric and asymmetric crossing-shock-waves/turbulent boundary layer interactions. EARD Contract F61708-97-W0136 Final Report for the period July 1997 – July 1998. Novosibirsk, 1998, 76 p.
4. Knight D.D. Numerical solution of 3-D shock wave turbulent boundary layer interactions. AGARD Special Course on Shock Wave/Turbulent Boundary-Layer Interactions in Supersonic and Hypersonic Flows, Advisory Group for Aerospace Research and Development, August 1993. AGARD Report, 1993, № 792, p. 3-1 –3-34.
5. Zheltovodov A.A., Maksimov A.I. and Shevchenko A.M. Topology of three-dimensional separation under the conditions of symmetric interaction of crossing shocks and expansion waves with turbulent boundary layer. Thermophysics and Aeromechanics, 1998, Vol. 5, № 3, p. 293–312.
6. Zheltovodov A.A., Maksimov A.I., Shevchenko A.M., and Knight D.D. Topology of three-dimensional separation under the conditions of asymmetric interaction of crossing shocks and expansion waves with turbulent boundary layer. Thermophysics and Aeromechanics, 1998, Vol. 5. № 4. P. 483–503.
7. Zheltovodov A.A., Maksimov A.I., Shevchenko A.M., Vorontsov S.S., Knight D.D. Experimental study and computational comparison of crossing shock wave/turbulent boundary layer interaction. Int. Conf. on the Methods of Aerophys. Research: Proc. Pt 1. Novosibirsk, 1994, p. 221–230.
8. Knight D.D., Garrison T.J., Settles G.S., Zheltovodov A.A., Maksimov A.I., Shevchenko A.M., Vorontsov S.S. Asymmetric crossing shock wave/turbulent boundary layer interaction. AIAA J., 1995, Vol. 33, № 12, p. 2241–2249.
9. Knight D.D., Garrison T.J., Settles G.S., Zheltovodov A.A., Maksimov A.I., Shevchenko A.M., Vorontsov S.S. Asymmetric crossing shock wave/turbulent boundary layer interaction. AIAA Paper 95– 0231, 1995, 18 p.
10. Gnedin M., Knight D., Zheltovodov A., Maksimov A., Shevchenko A., Vorontsov S. 3-D crossing shock wave - turbulent boundary layer interaction. AIAA Paper 96–2001, 1996, 18 p.
11. Gnedin M., Zha G., Knight D., Zheltovodov A., Maksimov A., Shevchenko A., Vorontsov S. 3-D crossing shock wave – turbulent boundary layer interaction. Int. Conf. on the Methods of Aerophys. Research: Proc., Pt 1. Novosibirsk, 1996, p. 114–122.
12. Gaitonde D.V., Shang J.S., Garrison T.G., Zheltovodov A.A., Maksimov A.I. Evolution of the separated 3-D shock wave/turbulent boundary layer interaction. AIAA Paper 97-1837, 1997, 14 p.
13. Gaitonde D.V., Visbal M.R., Shang J.S., Zheltovodov A.A., Maksimov A.I. Parametric investigation of flowfield structure and validation issues in 3-D crossing-shock wave/turbulent boundary layer interactions. Int. Conf. on the Methods of Aerophys. Research: Proc. Pt 1. Novosibirsk, 1998, p. 67–76.
14. Kussoy M..I., Horstman K.C. Intersecting shock-wave/turbulent boundary-layer interactions at Mach 8.3. NASA TM 103909, 1992, 46 p.

15. Gaitonde D., Edvards J.R., Shang J.S. The computed structure of a 3-D turbulent interaction caused by a cylinder/offset flare juncture. AIAA Paper 95–0230, 1995, 17 p.
16. Launder B.E., Sharma D.I. Application of the energy dissipation model of turbulence to the calculation of flows near a spinning disk. Letters in Heat and Mass Transf, 1974, Vol. 1, p. 131–138.
17. Gaitonde D., Shang J.S. The structure of a turbulent double-fin interaction at Mach 4. AIAA J., 1995, Vol. 33, № 12, p. 2250–2258.
18. Gaitonde D., Shang J., Visbal M. Calculations on a double-fin turbulent interaction at high speed. AIAA J., 1995, Vol. 33, № 2, p. 193–200.
19. Gaitonde D., Shang J.S. On 3-D shock wave/turbulent boundary layer interactions at Mach 4. AIAA Paper 96–0043, 1996, 16 p.
20. Nedungadi A., Lewis M. Computational study of the flowfield associated with oblique shock/vortex interaction. AIAA J., 1996, Vol. 34, № 12, p. 2545–2553.
21. A.A.Zheltovodov. Analysis of the features of two-dimensional separated flows at supersonic velocities. The Study of Near-Wall Flows of Viscous Gas, Novosibirsk: Inst. Theor. Appl. Mech., Siberian Branch, USSR Acad. Sci., 1979, p. 59–94 (In Russian).
22. Borisov A.V., Zheltovodov A.A., Maksimov A.I., Fedorova N.N., Shpak S.I. Verification of turbulence model and computational metdods of supersonic separated flows. Int. Conf. on the Methods of Aerophys. Research: Proc. Pt 1. Novosibirsk, 1996, p. 54–61.
23. Bedarev I.A., Zheltovodov A.A., Fedorova N.N. Supersonic turbulent separated flows numerical model verification. Int. Conf. on the Methods of Aerophys. Research: Proc. Pt 1. Novosibirsk, 1998, p. 30–35.
24. Zubin M.A., Ostapenko N.A., Flow structure in the separation region under the interaction of a normal shock wave with the boundary layer in a corner, Izv. AN SSSR, Mekhanika Zhidkosti I Gaza, 1979, No 3, p. 51–58 (In Russian, Engl. transl. in Fluid Dynamics).
25. Zheltovodov A.A., Kharitonov A.M., Specific features of mass and heat transfer in two- and three-dimensional separation regions, in: Heat and Mass Transfer VI: Proc. VI All-Union Conference on Heat and Mass Transfer, Vol. 1, Part II, Minsk, 1980, p. 64–70.
26. Zheltovodov A.A. Regimes and properties of three-dimensional separation flows. Journ. of Applied Mech. and Techn. Physics, 1982, № 3, p. 116–123 (In Russian, Engl transl., p. 413–418).
27. Zheltovodov A.A., Maksimov A.I., Scheulein E. Development of turbulent separated flows in the vicinity of swept shock waves. Interaction of Complex 3-D Flows, Novosibirsk: Inst. Theor. Appl. Mech., Siberian Branch, USSR Acad. Sci., 1987, p. 67–91 (In Russian).
28. Panaras A. G. The effect of the structure of swept-shock-wave/turbulent-boundary-layer interactions on turbulence modeling. J. Fluid Mech., 1997, Vol. 338, p. 203–230.
29. Panaras A. G. Algebraic turbulence modeling for swept shock-wave/turbulent boundary-layer interactions. AIAA J., 1997,Vol. 35, № 3, p. 456–463.
30. Garrison T.J., Settles G.S. Interaction strength and model geometry effects on the structure of crossing-shock wave/turbulent boundary layer interactions. AIAA Paper, 1993, № 0780, 12 p.
31. Zheltovodov A.A., Pavlov A.A., Shilein E.H., Yakovlev V.N. Interconnectionship between the flow separation and the direct and inverse transition at supersonic speed conditions. IUTAM Simp. on Laminar-Turbulent Transition, Novosibirsk, 1984: Proc. Springer–Verlag, 1985, p. 503–508.

32. Zheltovodov A.A. Peculiarities of development and modeling possibilities of supersonic turbulent separated flows, IUTAM Separated Flows and Jets Simp., Novosibirsk, 1990: Proc. Springer–Verlag, 1991, p. 225–236.
33. Schuelein E., Zheltovodov A.A. Development of experimental methods for the hypersonic flows studies in Ludwieg tube. Int. Conf. on the Methods of Aerophys. Research: Proc. Pt 1. Novosibirsk, 1998, p. 191–199.
34. Tobak M., Peake D.J. Topology of three dimensional separated flows // Annual Review of Fluid Mech., 1982, Vol. 14, p. 61–85.
35. Dolling D.S. Unsteady phenomena in shock wave-turbulent boundary layer interactions. Turbulent Boundary-Layer Interactions in Supersonic and Hypersonic Flows, Advisory Group for Aerospace Research and Development, August 1993. AGARD Report, 1993, № 792, p. 4-1 – 4-46.
36. Lipanov A.M., Kisarov Yu.F., and Klyuchnikov I.G. Numerical simulation of viscous subsonic flows for the Reynolds number of 10^4. Matem. Modelirovanie, 1997, Vol. 9, No. 3, p. 3–12 (In Russian).
37. Lipanov A.M., Kisarov Yu.F., and Klyuchnikov I.G. A class of high-order difference schemes for direct simulation of turbulent flows for the Reynolds number of 10^5. In: The Use of Mathematical Simulation for Solving Problems in Science and Technology, Izhevsk, 1997, p. 81–102.
38. Urbin G., Knight D., Zheltovodov A.A. Compressible large eddy simulation using unstructured grid: Supersonic turbulent boundary layer and compression corner. AIAA Paper 99–0427, 1999, 11 p.
39. Hunt D., Nixon D. A very large eddy simulation of an unsteady shock wave/turbulent boundary layer interaction. AIAA Paper 95–2212, 1995, 11 p.
40. Zheltovodov A.A. Physical features and some properties of 2D and 3D separated flows. Izv. AN SSSR, Ser. Mekhanika Zhidkosti i Gaza, 1979, No 3, p. 42–50.
41. Zheltovodov A.A., Maksimov A.I., Gaitonde D.V., Visbal M.R., Shang J.S. Experimental and computational studies of symmetric crossing shocks and expansion waves with turbulent boundary layer. Thermophysics and Aeromechanics, 1999 (to be published).
42. Narayanswami N., Horstman C.C., Knight D.D, Numerical simulation of crossing shock/turbulent boundary layer interaction at Mach 8.3 – comparison of zero- and two-equation turbulence models. AIAA Paper 93–0779, 1993, 14 p.
43. Kussoy M.I., Horstman K.C., Horstman C.C. Hypersonic crossing shock-wave/turbulent-boundary-layer interactions. AIAA J., 1993, Vol.31, № 12, p. 2197–2203.
44. Narayanswami N., Horstman C.C., Knight D.D. Computation of crossing shock/turbulent boundary layer interaction at Mach 8.3, AIAA J., 1993, Vol. 31, № 8, p. 1369–1376.
45. Bardina J.E., Coakley T.J. Three-dimensional Navier-Stokes simulations with two-equation turbulence models of intersecting shock waves/turbulent boundary layer at M = 8.3. AIAA Paper, 1994, № 1905, 11 p.
46. Bardina J.E., Coakley T.J. The structure of intersecting shock waves/turbulent boundary layer interaction flow. AIAA Paper, 1995, № 2215, 11 p.
47. Smith B.R. Prediction of hypersonic shock-wave/turbulent-boundary-layer interactions. AIAA J., 1996, Vol.33, № 5, p. 614–619.
48. Ludwieg H., Hottner Th., Grauer-Garson H. Der Rohrwindkanal der Aerodynamischen Versuchsanstalt Gottingen. Janhrbuch 1969 der DGLR, 1970, p. 52–58.

49. Schuelein E., Krogmann P., Stanewsky E. Documentation of two-dimensional impinging shock/turbulent boundary layer interaction flow. DLR Forschungsbericht. IB 223 - 96 A 49. October, 1996, 69 p.
50. Schuelein E., Koch S., Rosemann H. Skin friction measurement and transition detection techniques for the Ludwieg-Tubes at DLR. Proc. RTO/AGARD Fluid Dynamic Measurement Technology, Seattle, USA, September 22–25, 1997, p. 23-1–23-9.
51. Settles G.S. Recent scin friction techniques for compresible flows. AIAA Paper 86–1099, 1986.
52. Tanner L., Blows L. A study of the motion of oil films on surfaces in an air flow, with application to the measurementof skin friction. J.Phys. E.: Sci. Instrum., 1976, Vol. 9, p. 194–202.
53. Borisov A.V., Vorontsov S.S., Zheltovodov A.A., Pavlov A.A., Shpak S.I. Development of experimental and computational methods of studies of supersonic separated flows. Preprint No 9–93, ITAM SD RAS, Novosibirsk, 1993, 45 p.(In Russian).
54. Maksimov A.I., Pavlov A.A., Shevchenko A.M. Development of the optical skin friction measurement technique for supersonic gradient flows. Int. Conf. on the Methods of Aerophys. Research: Proc. Pt. 2. Novosibirsk, 1994, p. 172–177.
55. Young A.D. High speed flow // Modern developments in fluid mechanics. Vol. 1. / Ed. L. Howard. Oxford: Clarendon Press, 1953, p. 375–475.
56. Donohoe S.R., Bannik W.J. Surface reflective visualization of shock-wave/vortex interactions above a delta wing. AIAA J., 1997, Vol. 35, No 10, p. 1568–1573.

FIGURES

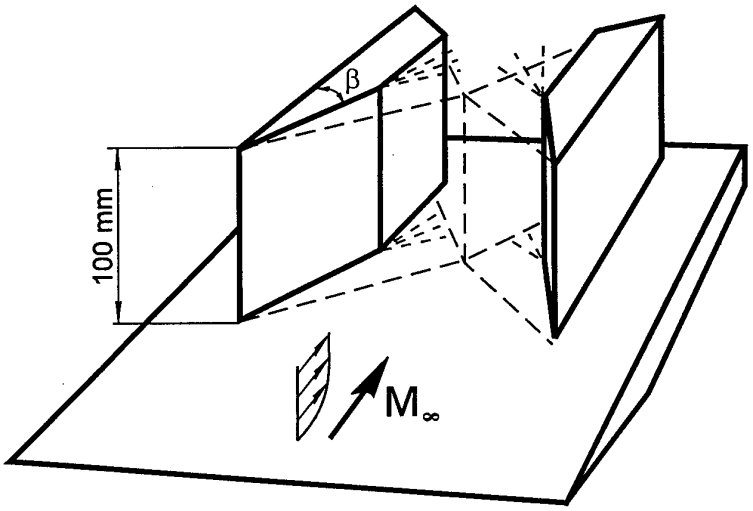

a

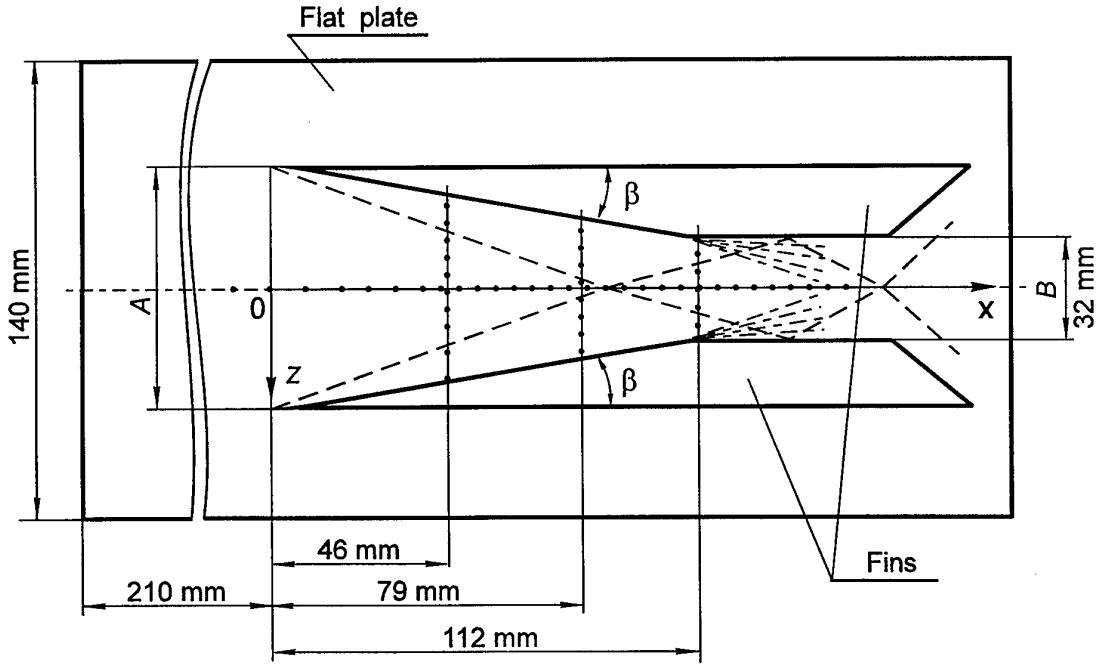

b

Fig. 1.1. Test configuration

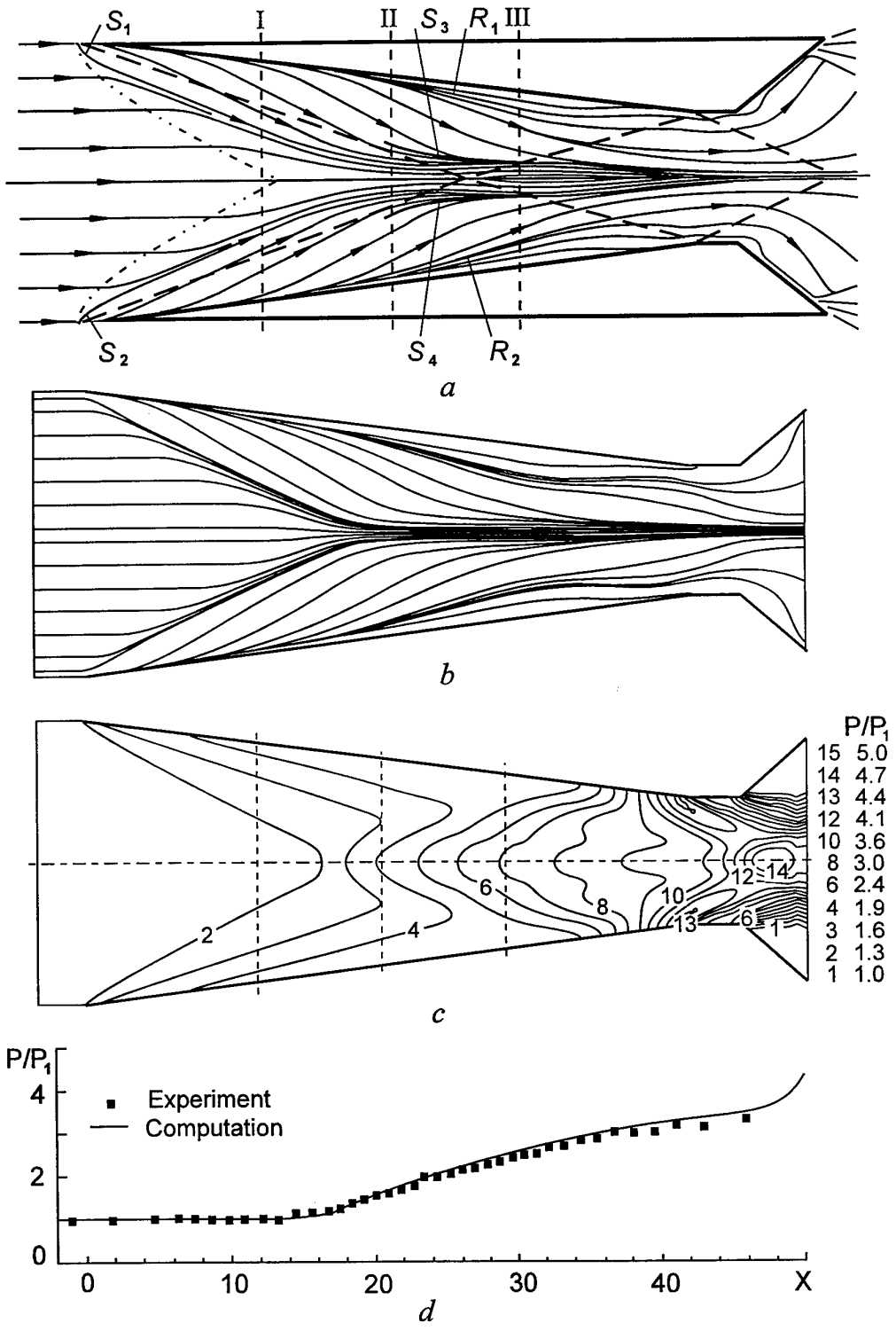

Fig. 1. 2. Comparison of experiments and computations for $\beta = 7°$, $M_\infty = 3.9$

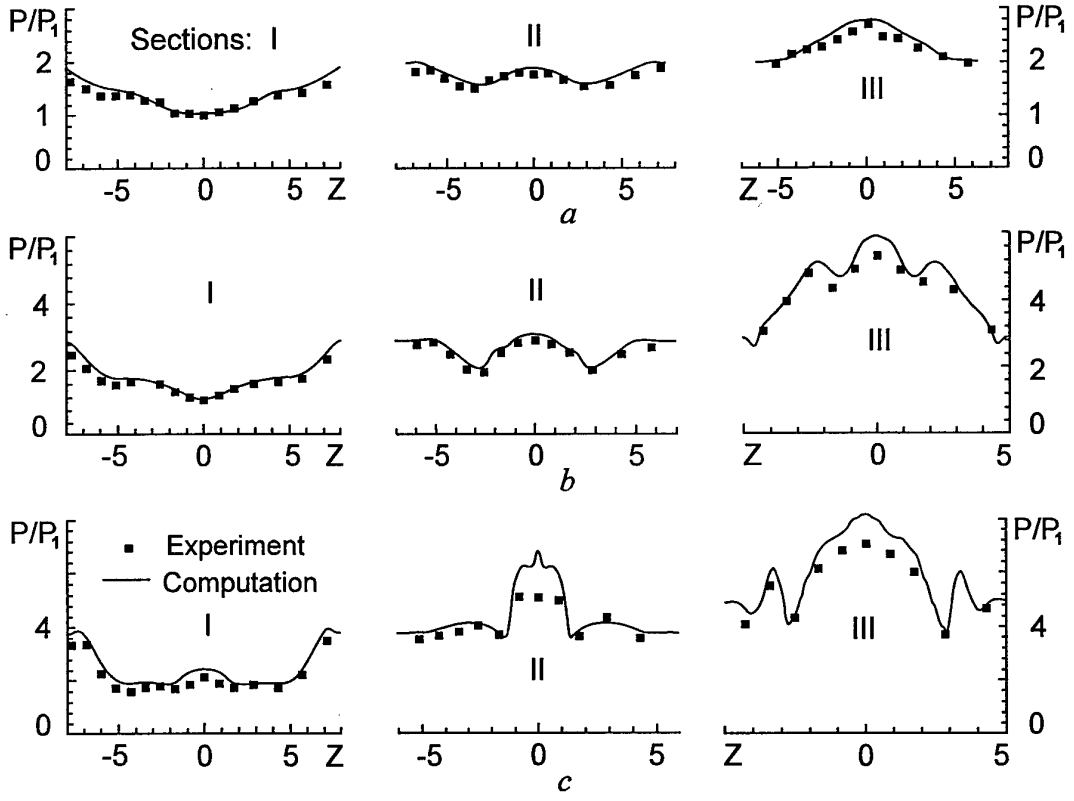

Fig. 1.3. Surface pressure distributions in cross sections at $M_\infty = 3.9$ and $\beta = 7°(a), 11°(b), 15°(c)$

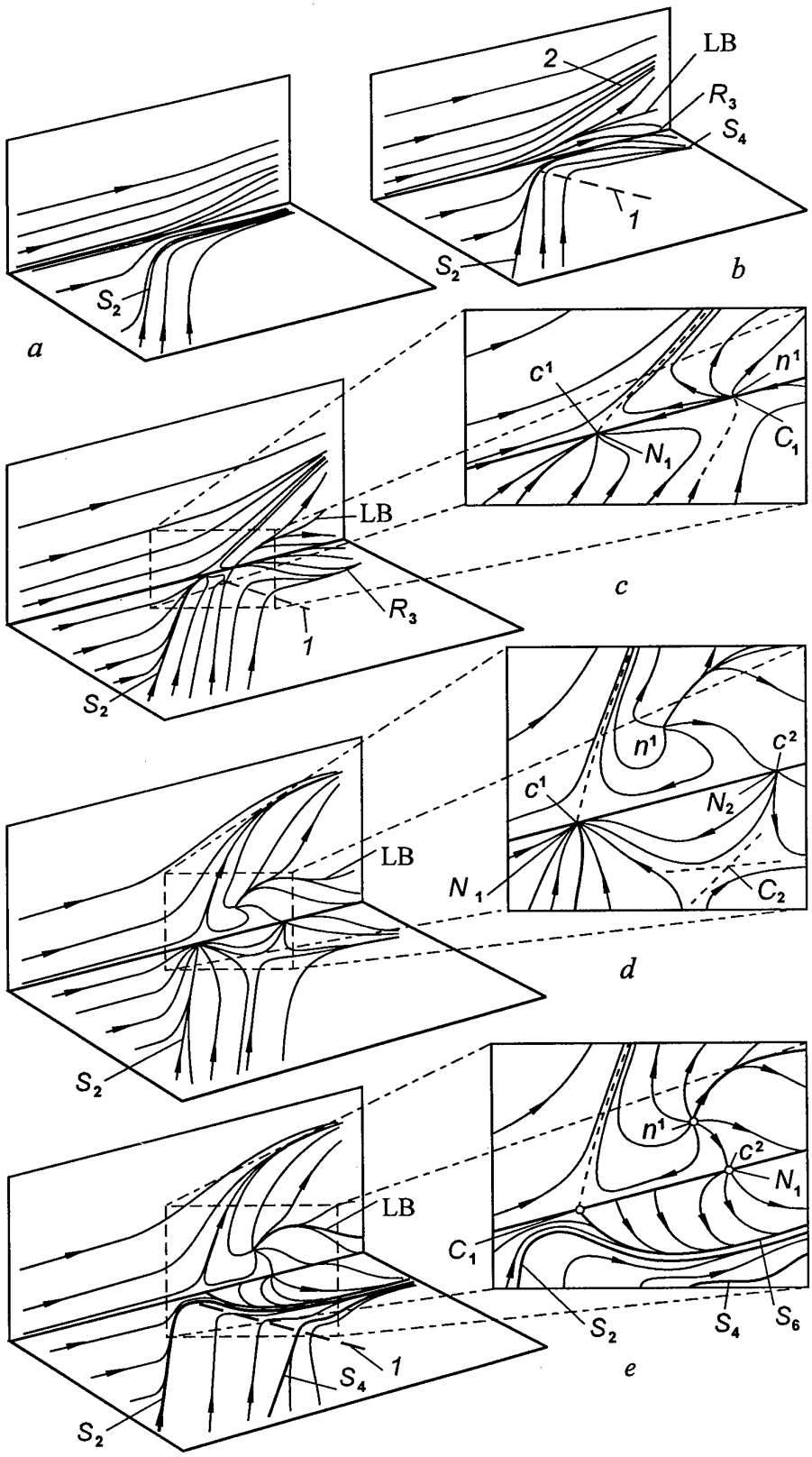

Fig. 1.4. Observed evolution of the computed separation topology for $M_\infty = 3.9$, $\beta = 7°$ (*a*), $11°$ (*b*), $11° < \beta < 15°$ (*c*), $15°$ (*d*) and supposed on a basis of experimental study for $\beta = 15°$ (*e*)

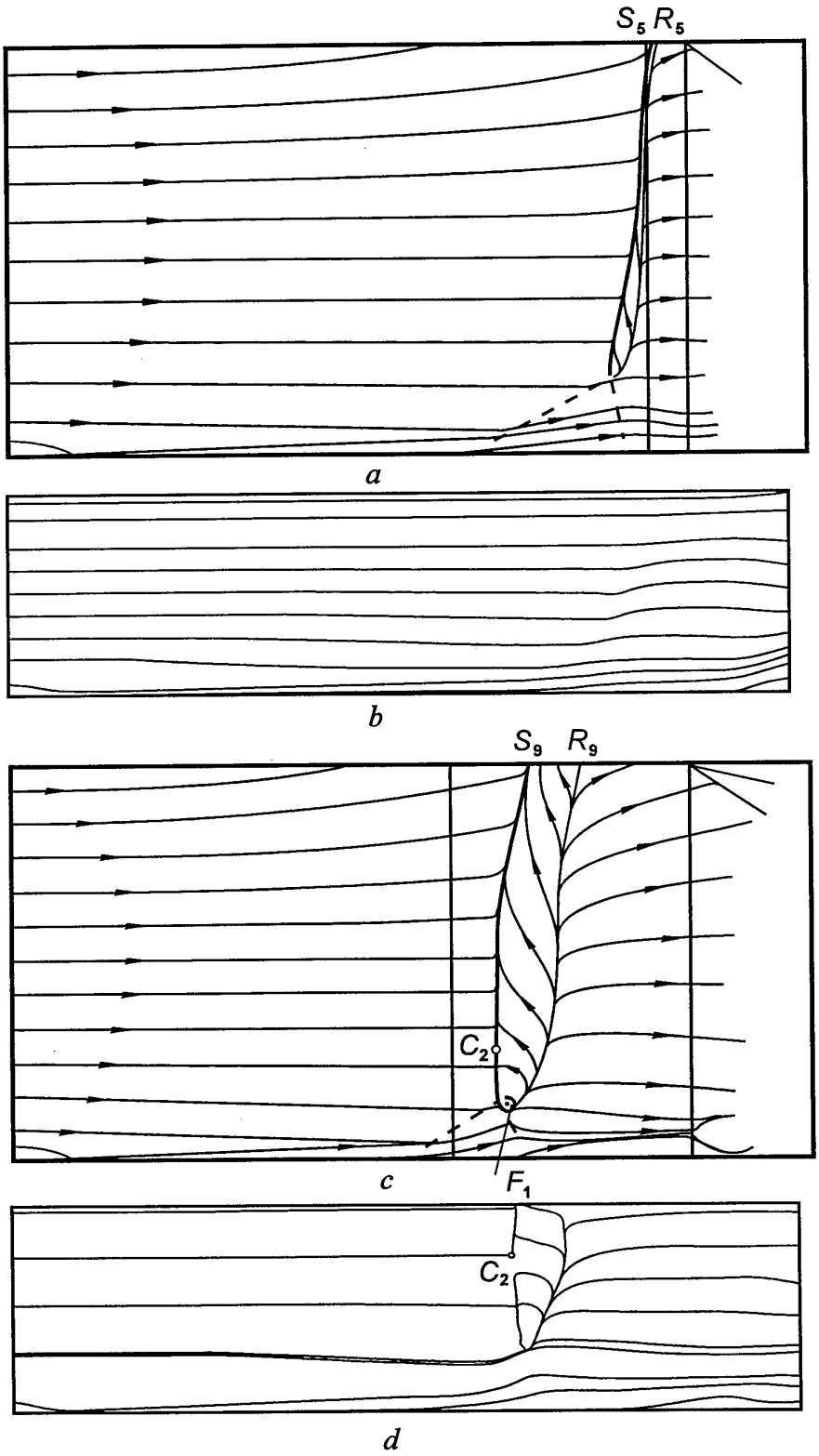

Fig. 1.5. Surface flow pattern on the fins sides for $M_\infty = 3.9$, $\beta = 7°$ (*a* - experiment, *b* - computation) and 11° (*c* - experiment, *d* - computation)

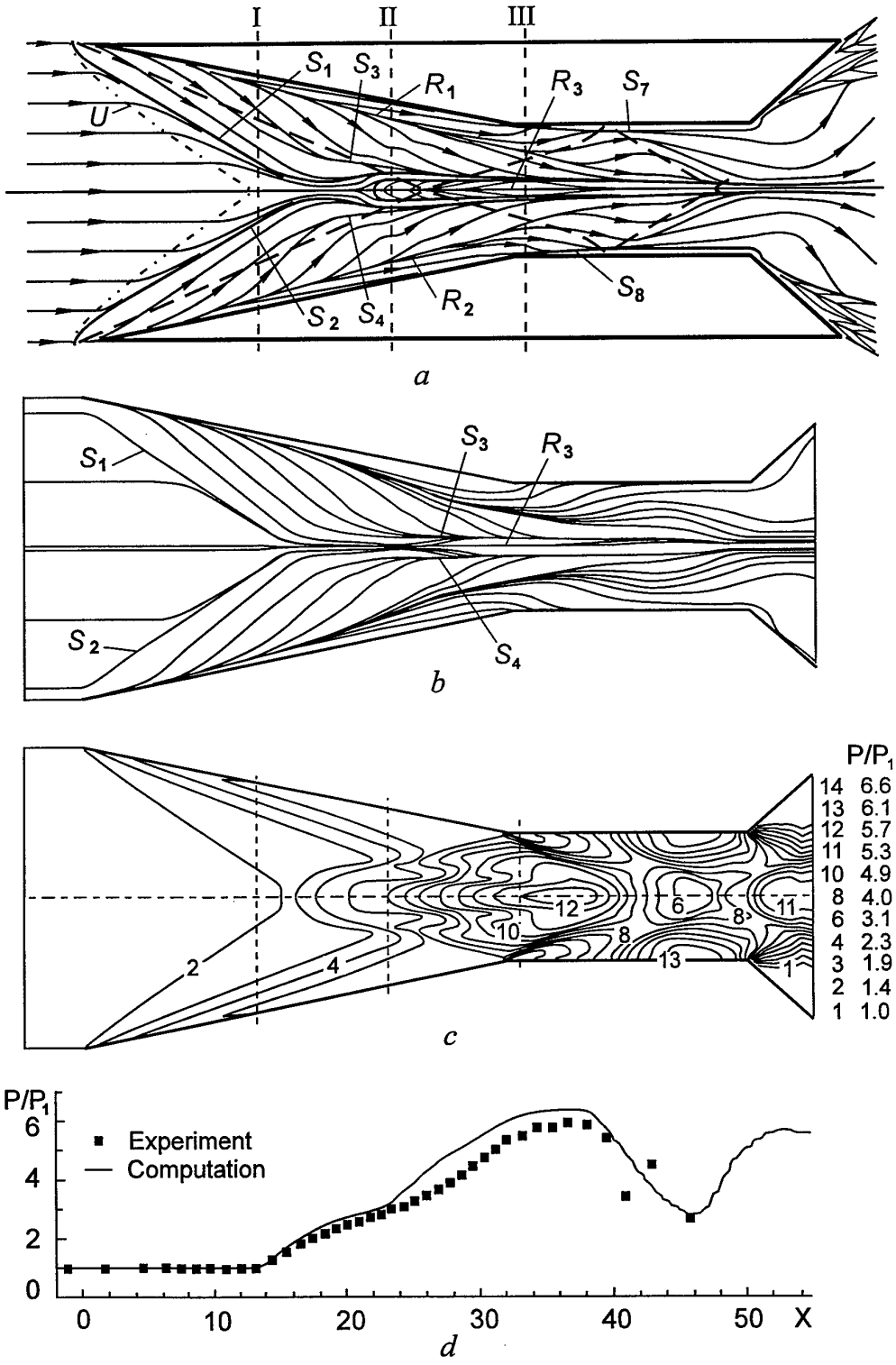

Fig. 1.6. Comparison of experiments and computations for $\beta = 11^{\circ}$, $M_{\infty} = 3.9$

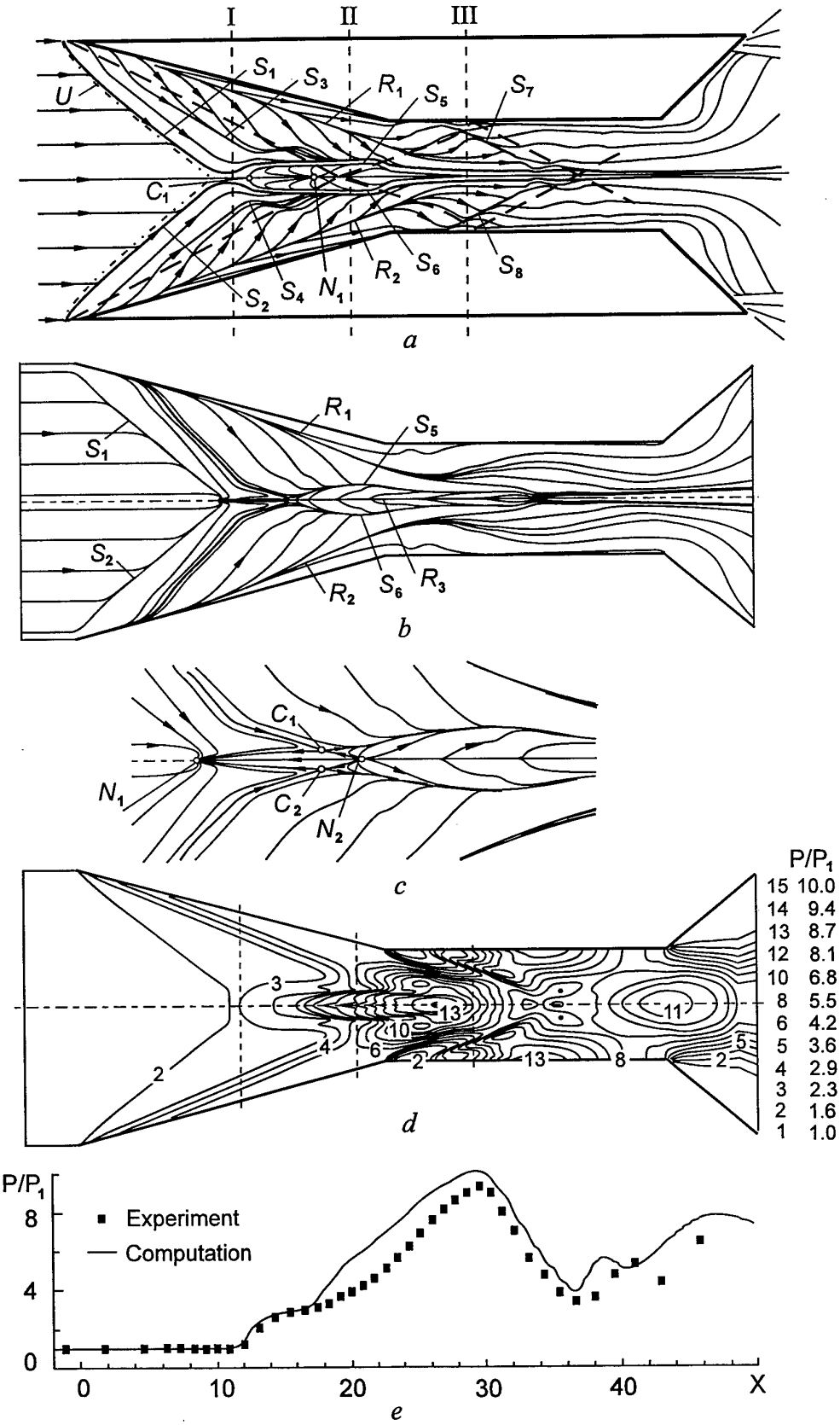

Fig. 1.7. Comparison of experiments and computations for $\beta = 15^{\circ}$, $M_{\infty} = 3.9$

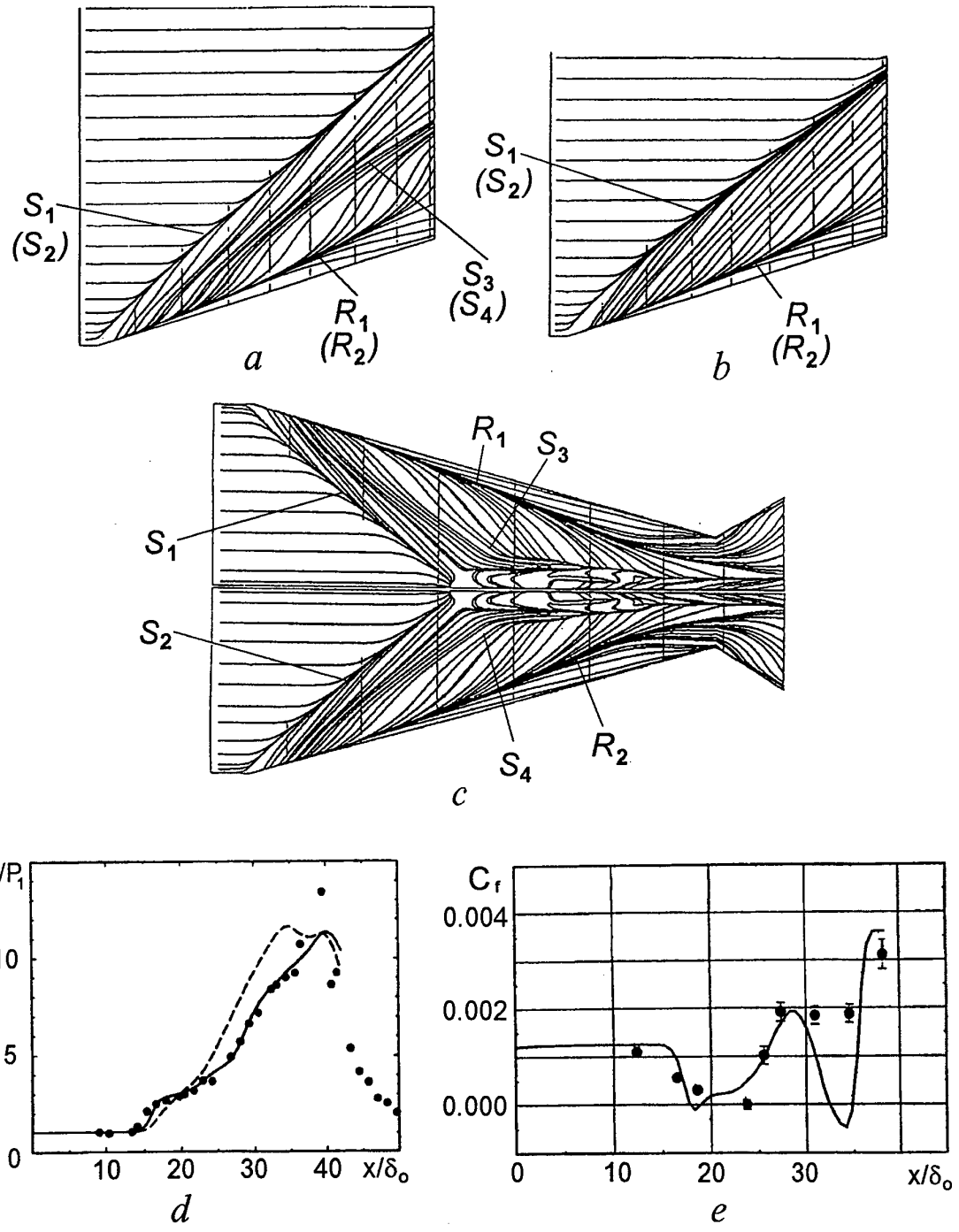

Fig. 1.8. Computations by A.Panaras for one- and two-fins configurations at $M_\infty = 3.9$:

a - modified B-L model, $\beta = 16°$;
b - original B-L model, $\beta = 16°$;
c - surface flow pattern for $\beta_1 = \beta_2 = 15°$, modified B-L model [29];
d - centerline pressure (• - experim. Settles, Garrison; --- - original B-L model;
—— - modified B-L model);
e - centerline skin friction (• - experim. Settles, Garrison; —— - modified B-L model)

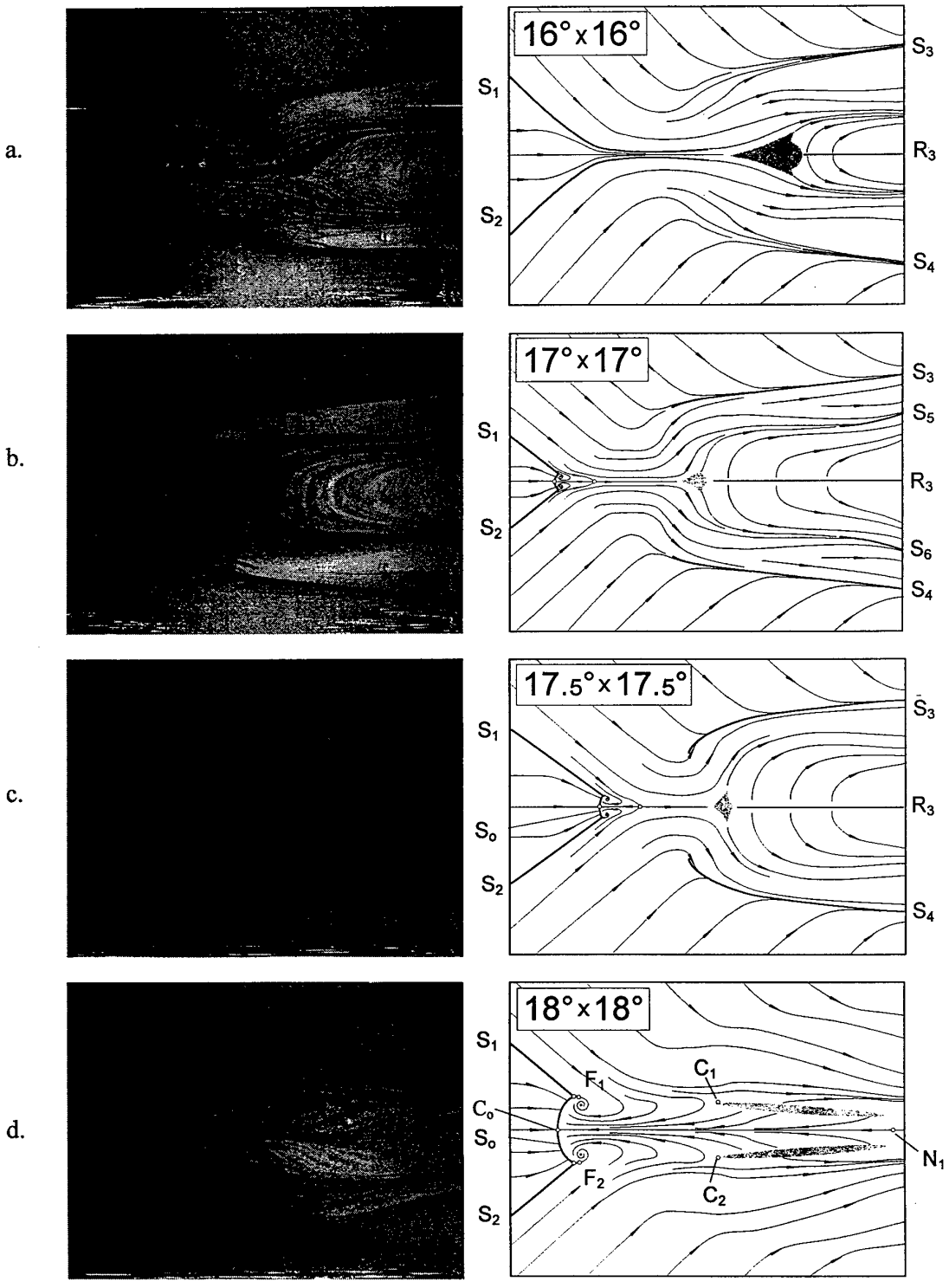

Fig. 1.9. Surface flow pattern variation for $M_\infty = 5$ [33]:

a) $\beta = 16°$, A/B = 1.86; b) $\beta = 17°$, A/B = 1,91; c) $\beta = 17{,}5°$, A/B = 1.93; d) $\beta = 18°$, A/B = 1,96

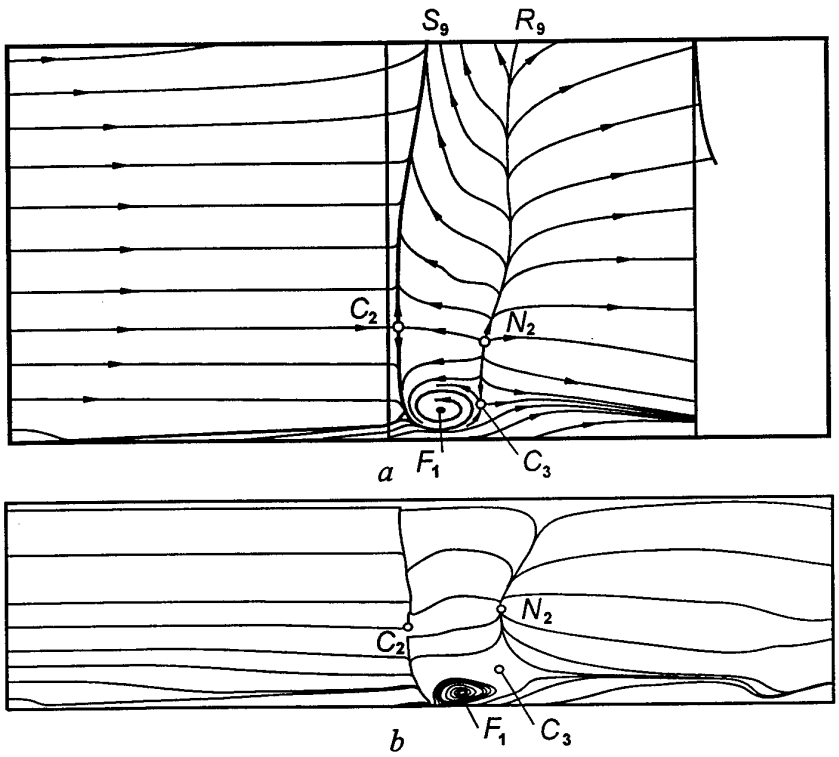

Fig. 1.10. Surface flow pattern on the fins sides for $\beta = 15^{\circ}$, $M_{\infty} = 3.9$ (*a* - experiment, *b* - computation)

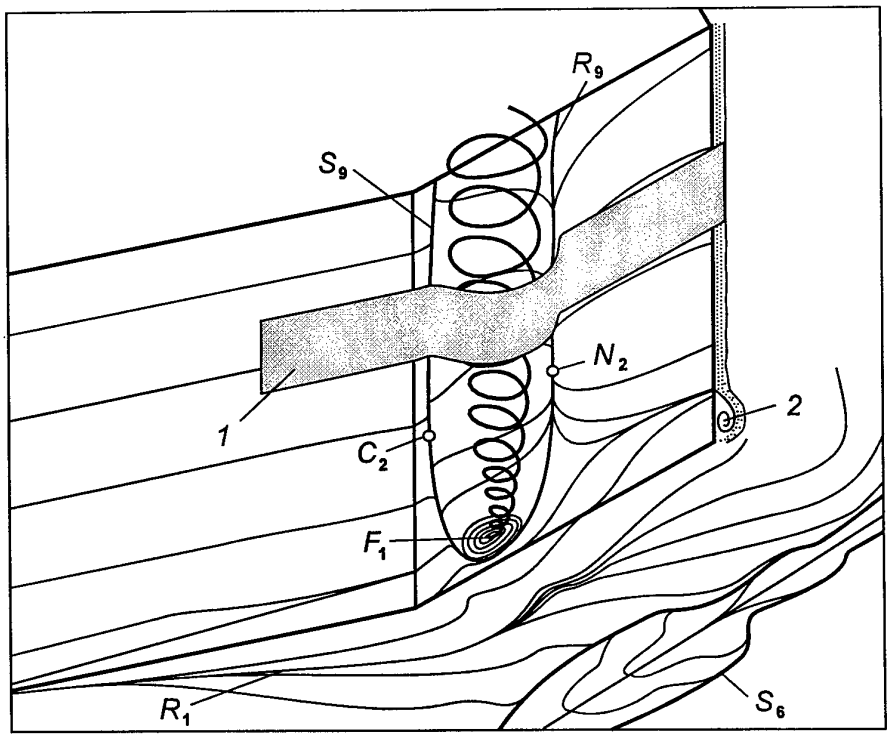

Fig. 1.11. Flowfield structure cased by vortex/sidewall interactions for $\beta = 15^{\circ}$, $M_{\infty} = 3.9$

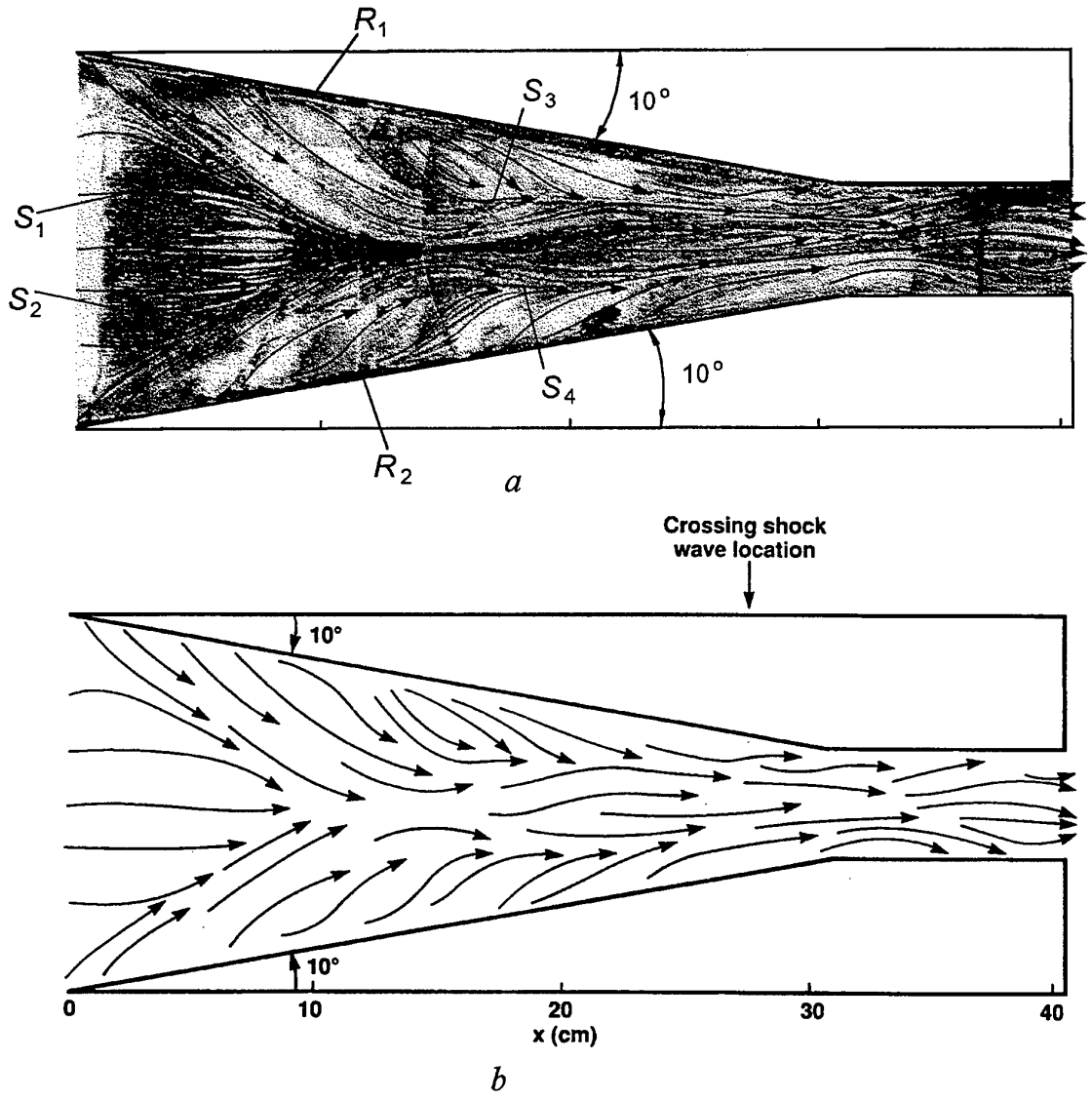

Fig. 1.12. Surface flow pattern for $\beta = 10^{\circ}$, $M_{\infty} = 8.3$ [14]

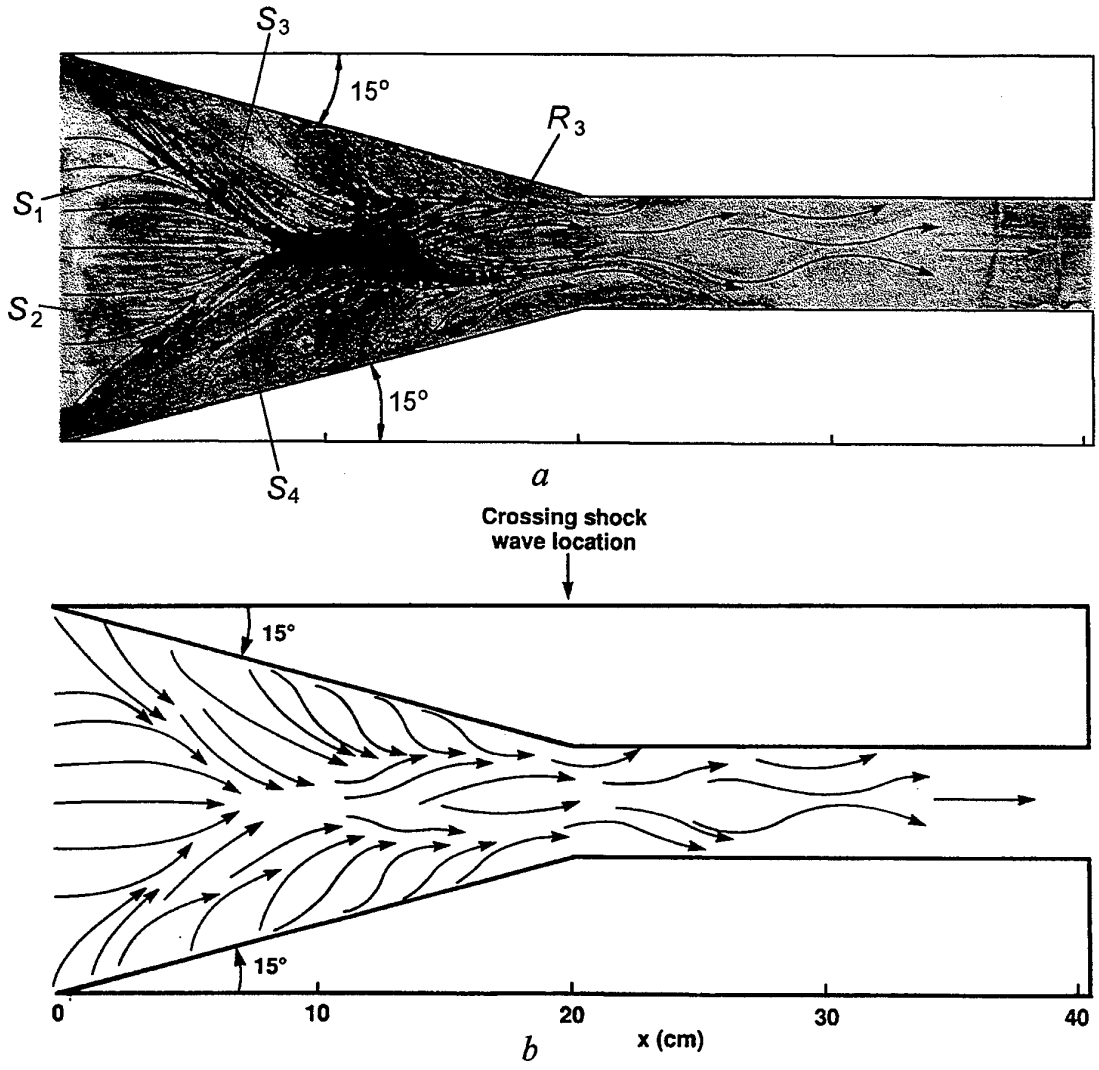

Fig. 1.13. Surface flow pattern for $\beta = 15°$, $M_\infty = 8.3$ [14]

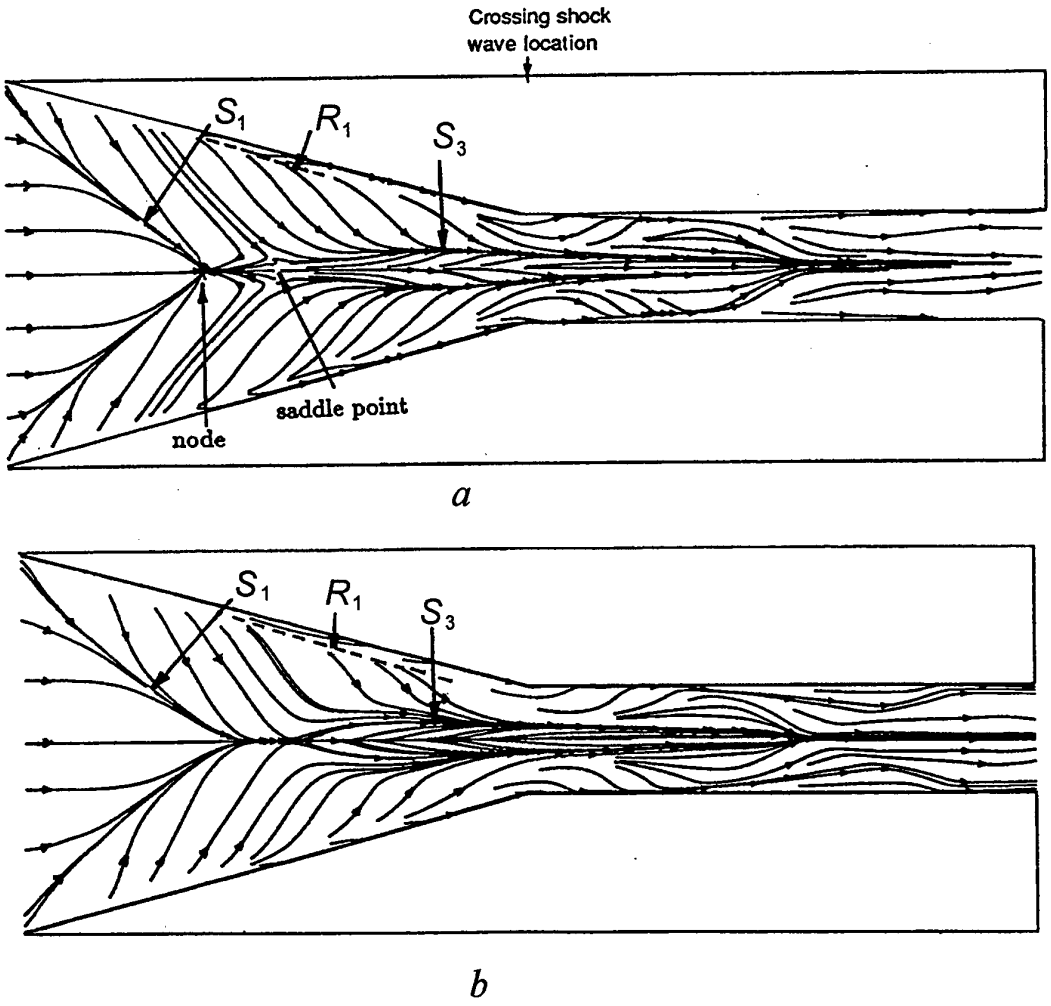

Fig. 1.14. Computations of surface flow pattern for $\beta = 15^{\circ}$, $M_{\infty} = 8.3$
(*a* - Boldwin-Lomax comp., *b* - Rodi comp.) [42]

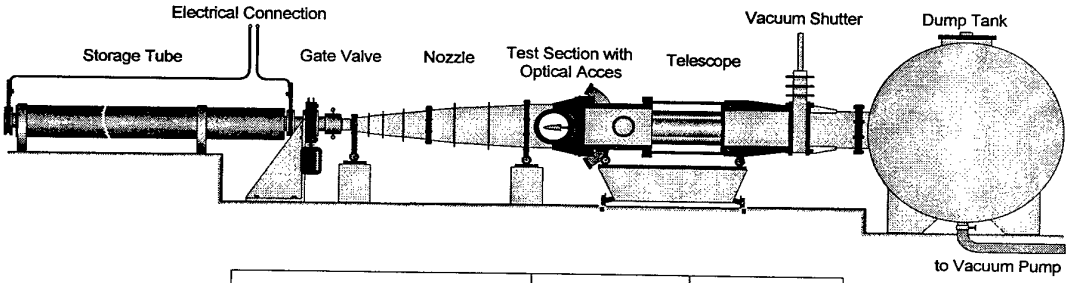

Performance	Tube A	Tube B
Max. Stag. Pressure, bar	15	40
Max. Stag. Temperature, °C	20	400
Mach Number	2.79 to 4.65	5.0 to 6.9
Unit Reynolds Number, 10^6 m^{-1}	5 to 60	5 to 50
Run Time, s	0.4	0.3
Test Section	0.5 x 0.5 m²	⌀ 0.5 m

Fig. 2.1. Super- and Hypersonic Ludwieg-Tube Goettingen (RWG)

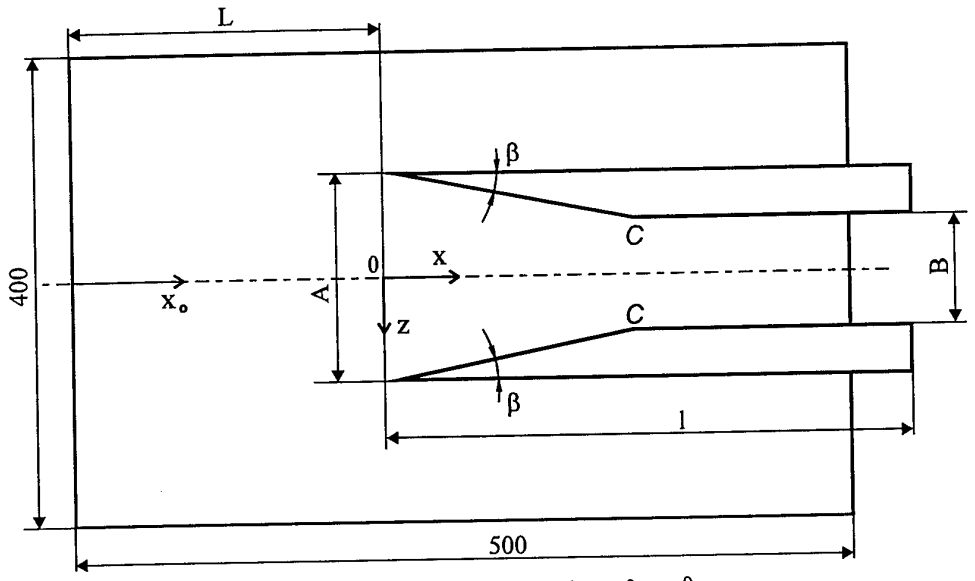

a Short Fins (SF, $\beta = 8°, 12°, 18°$)

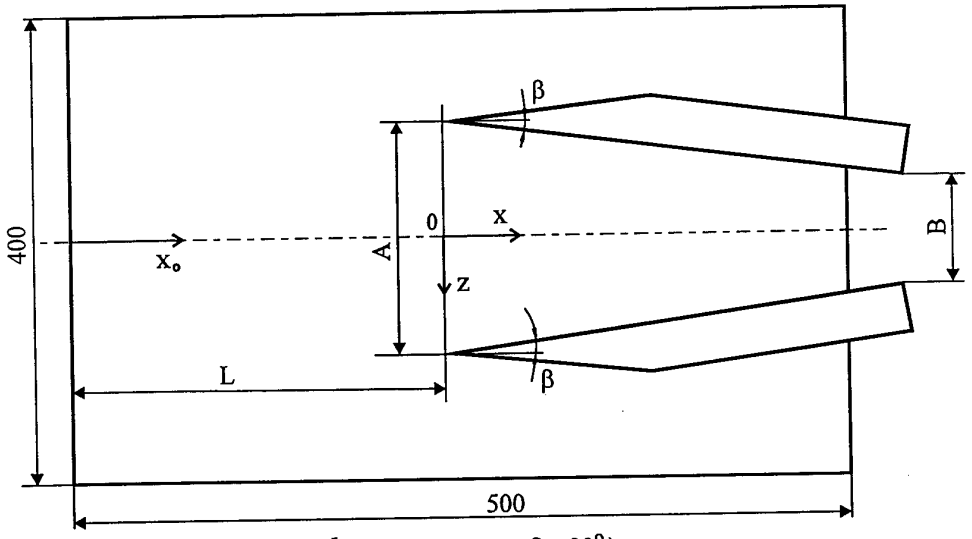

b Long Fins (LF, $\beta = 23°$)

Table 1. Basic configurations

β , deg.	L, mm	A, mm	B, mm	l, mm
8° x 8° (SF)	229.5	142.0	100	309
12° x 12° (SF)	249.5	161.5	100	280
18° x 18° (SF)	269.0	196.0	100	260
23° x 23° (LF)	286.0	307.0	100	

Fig. 2.2. Test models

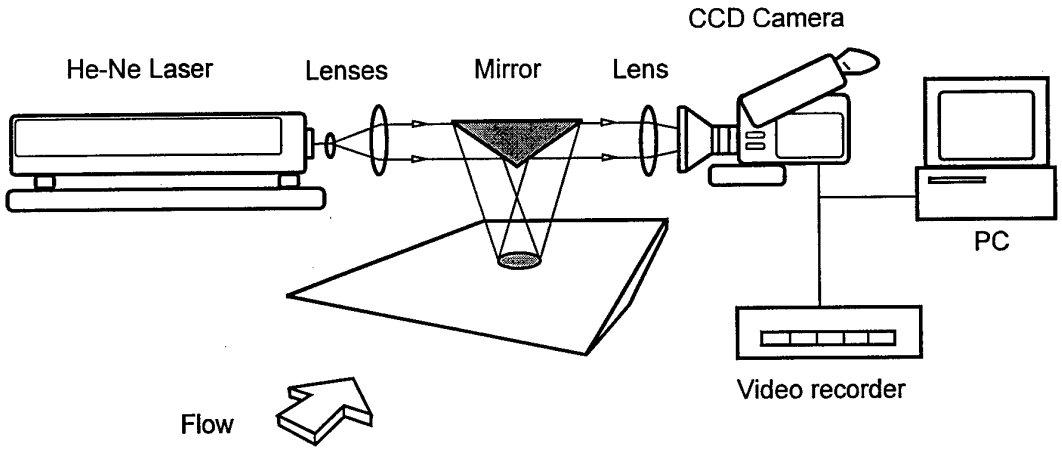

Fig. 2.3. Schematic of the GISF instrument set-up

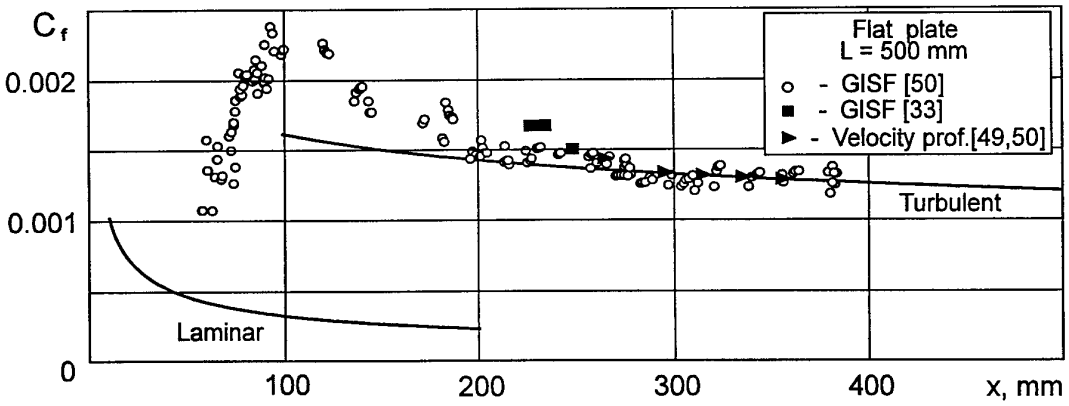

Fig. 2.4. C_f distributions on a plate

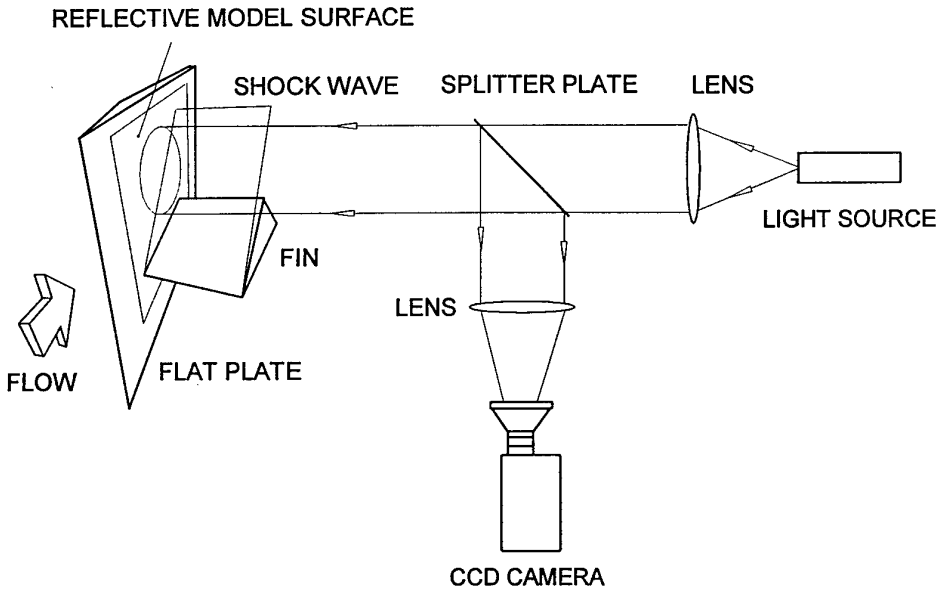

a

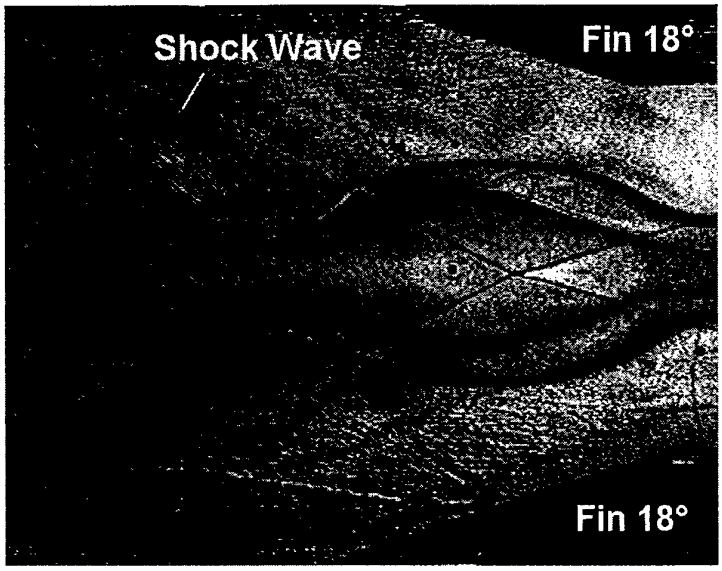

b

Fig. 2.5. Surface reflective visualisation shadowgraph and surface flow pattern for the double fin configuration $\beta = 18°$ at Mach 5

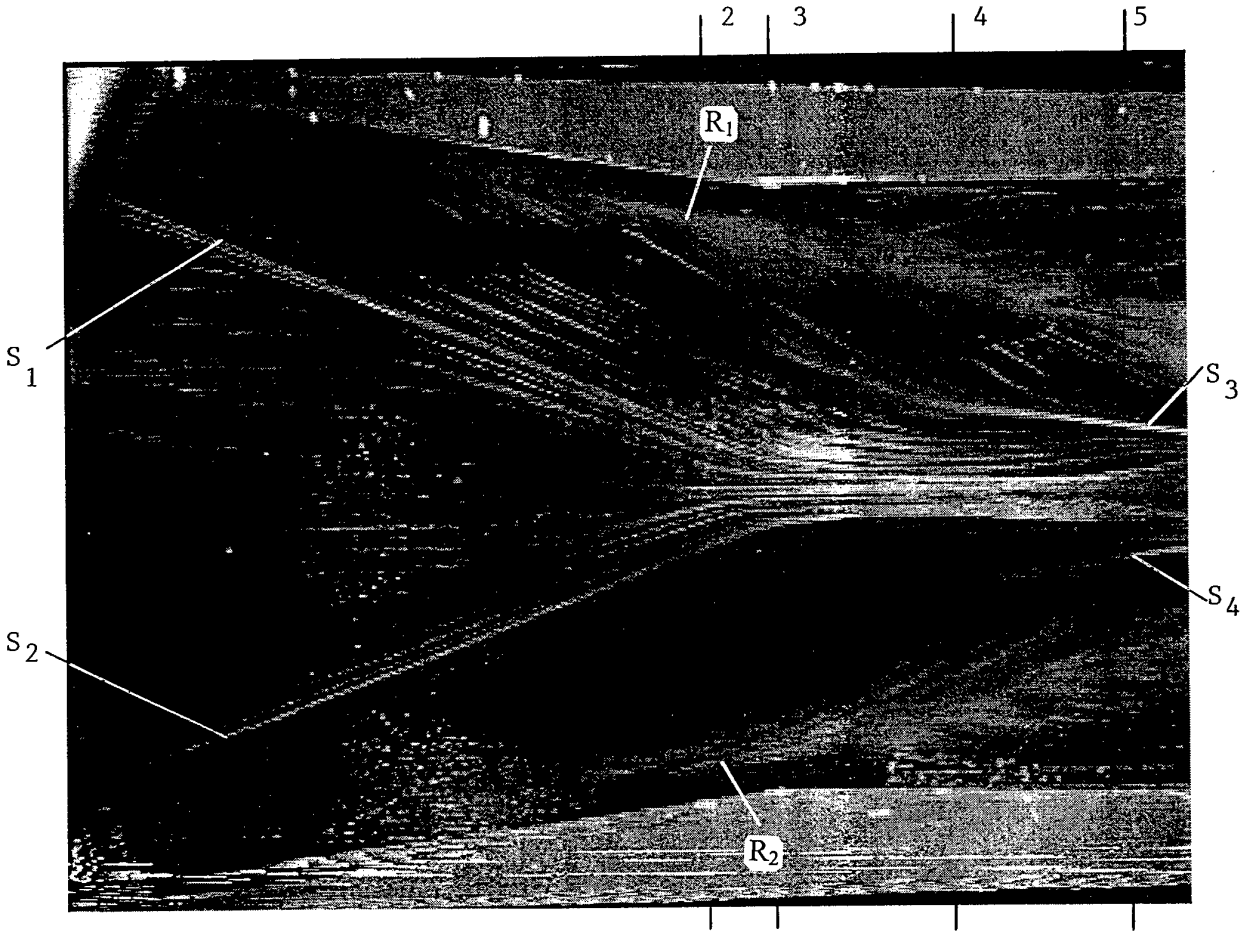

Double Fin: ß = 8°, A = 142 mm, B = 100.5 mm, L = 228 mm

M = 5, $Re_l = 40 \times 10^6$ 1/m (RWG DLR Göttingen)

Fig. 2.6

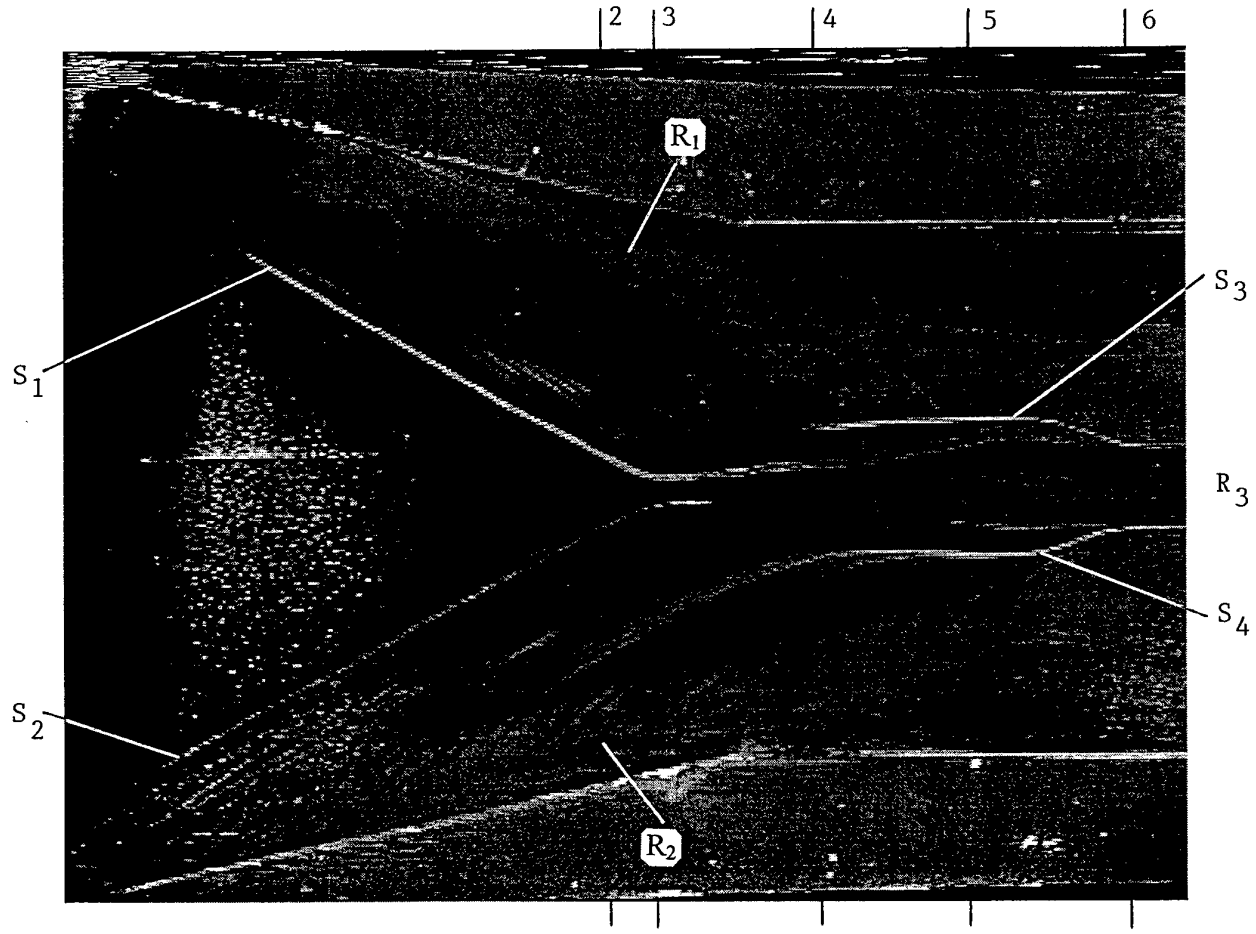

Double Fin: ß = 12°, A = 163 mm, B = 100.7 mm, L = 248 mm

M = 5, Re_1 = 40 x 10^6 1/m (RWG DLR Göttingen)

Fig. 2.7

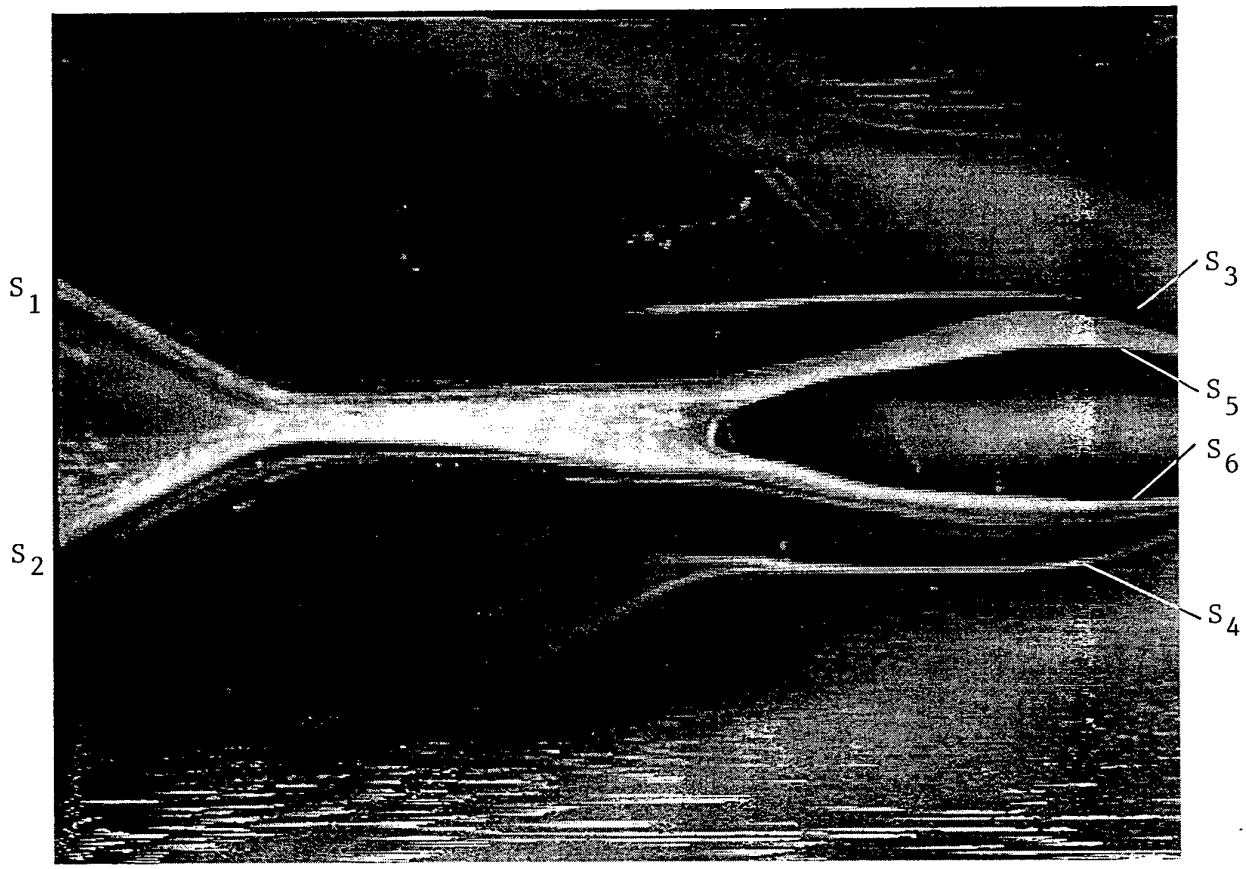

Double Fin: ß = 12°, A = 163 mm, B = 100.7 mm, L = 248 mm (Fragment)

M = 5, Re_1 = 40 x 10^6 1/m (RWG DLR Göttingen)

Fig. 2.8

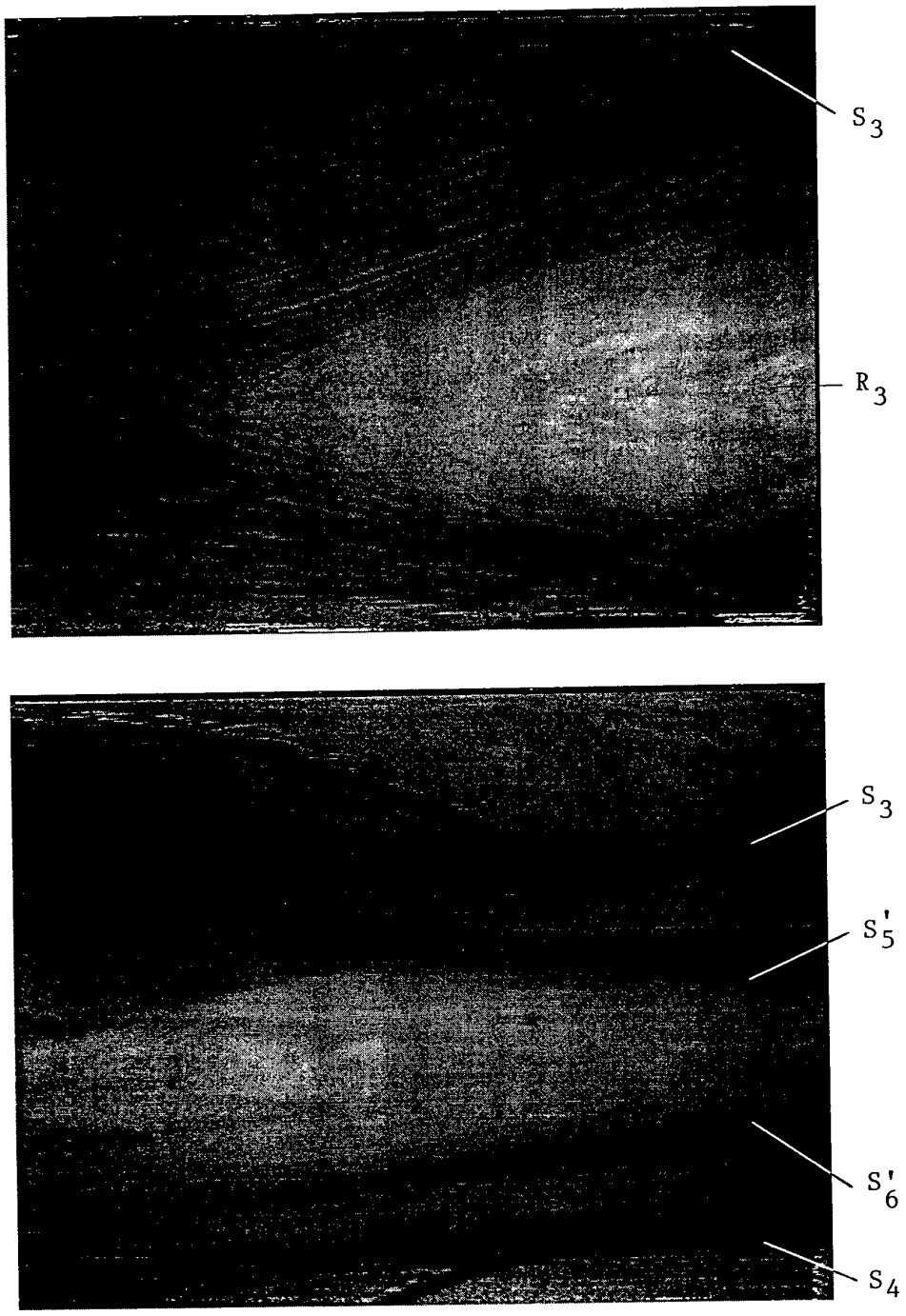

ß = 12°, A = 161.5 mm, B = 100 mm (Fragments)

Double Fin, M = 5, $Re_l = 40 \times 10^6$ 1/m (RWG DLR Göttingen)

Fig. 2.9

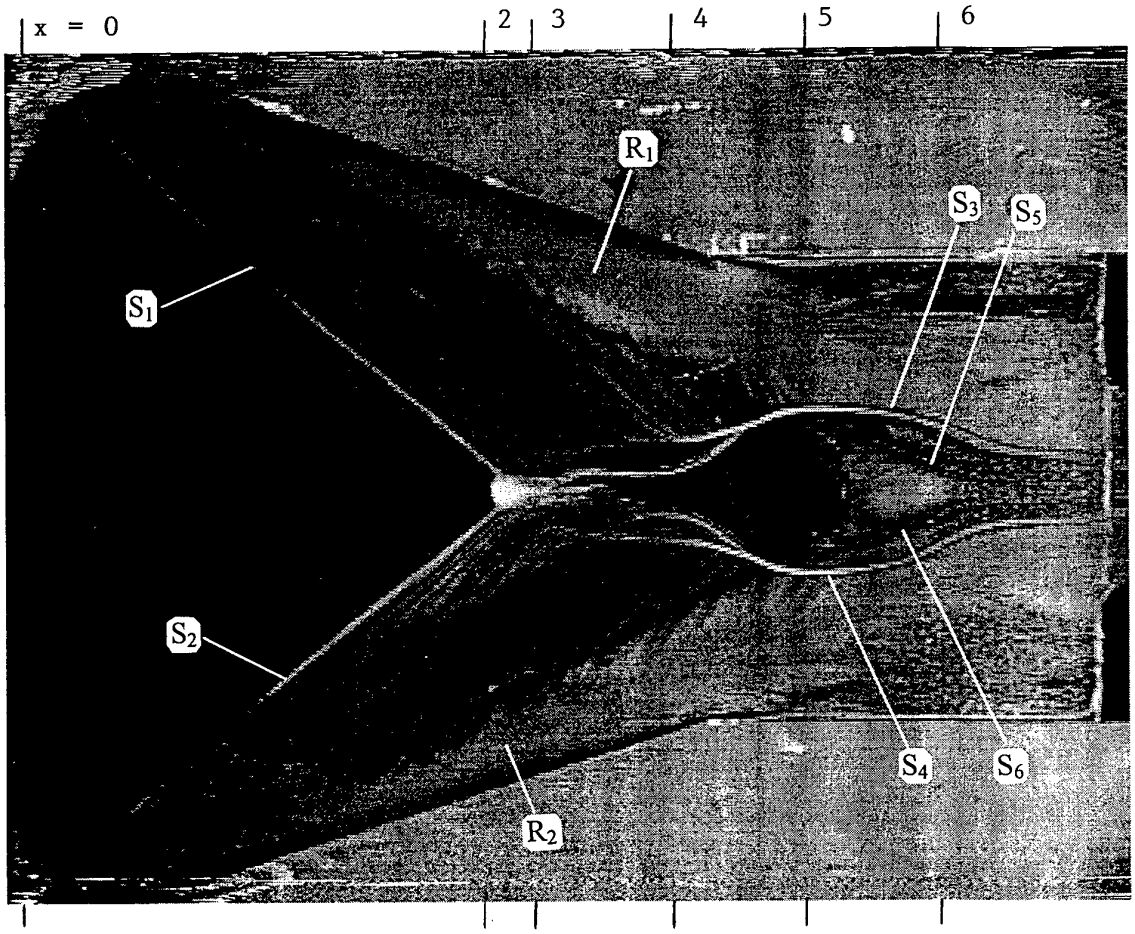

Double Fin: ß = 18°, A = 196 mm, B = 100 mm, L = 268 mm

M = 5, Re_1 = 40 x 10^6 1/m (RWG DLR Göttingen)

Fig. 2.10

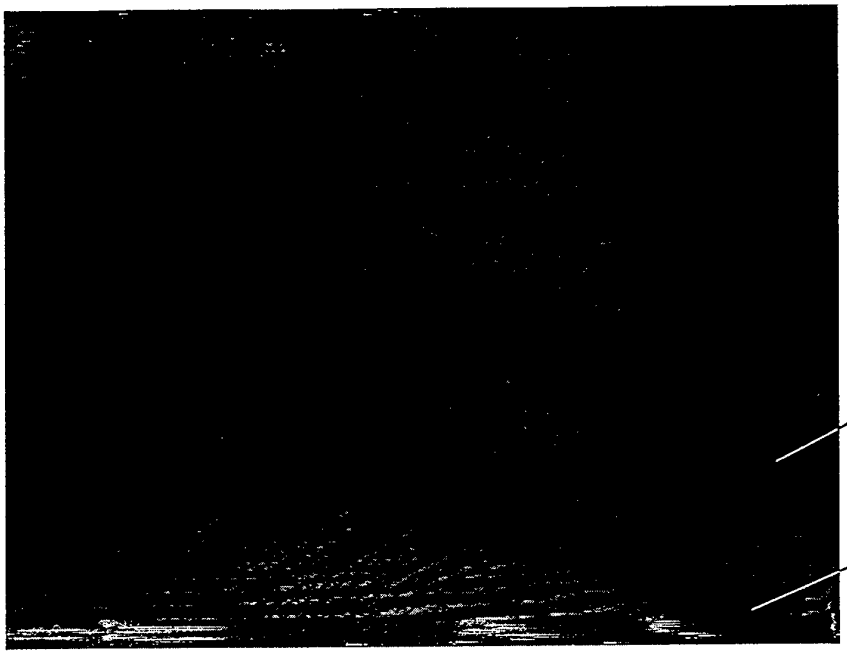

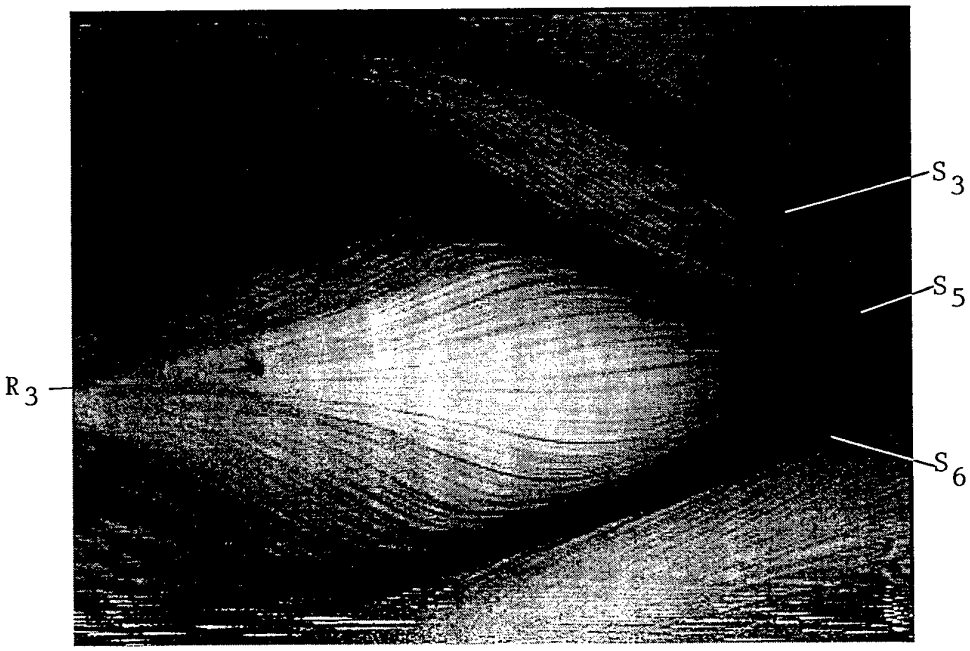

ß = 18°, A = 196 mm, B = 100 mm (Fragments)

Double Fin, M = 5, Re_l = 40 x 10^6 1/m (RWG DLR Göttingen)

Fig. 2. 11

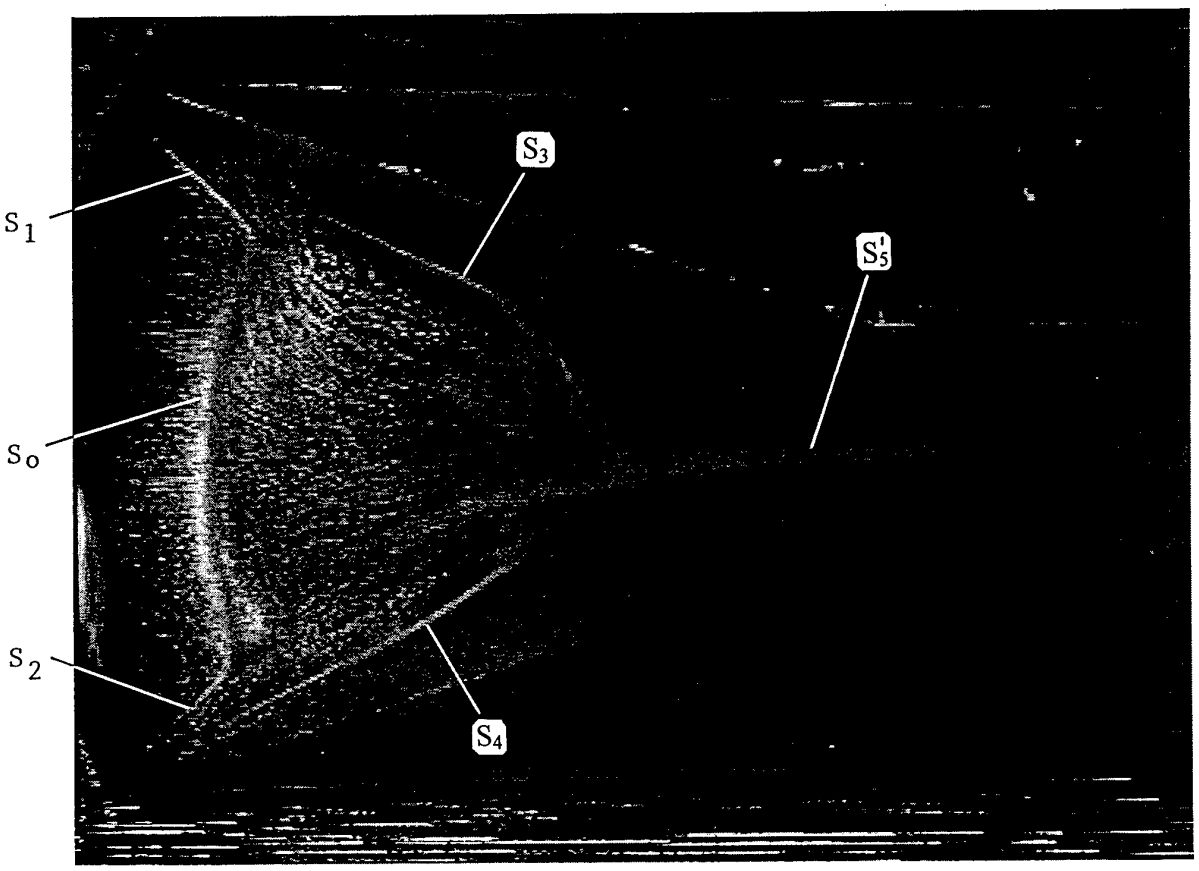

Double Fin: ß = 18°, A = 139.5 mm, B = 43.2 mm, L = 267 mm

(Start of run) M = 5, Re_1 = 40 x 10^6 1/m (RWG DLR Göttingen)

Fig. 2.12

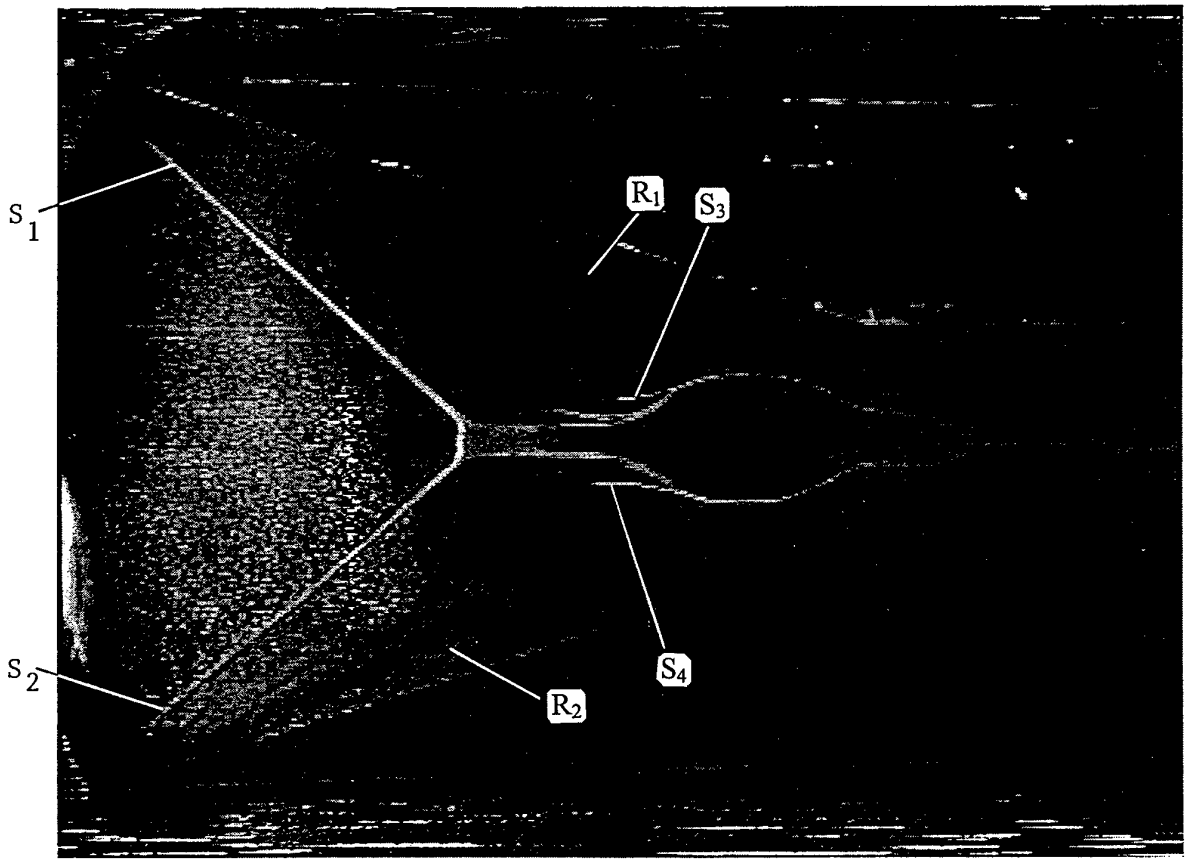

Double Fin: ß = 18°, A = 139.5 mm, B = 43.2 mm, L = 267 mm

M = 5, Re_1 = 40 x 10^6 1/m (RWG DLR Göttingen)

Fig. 2.13

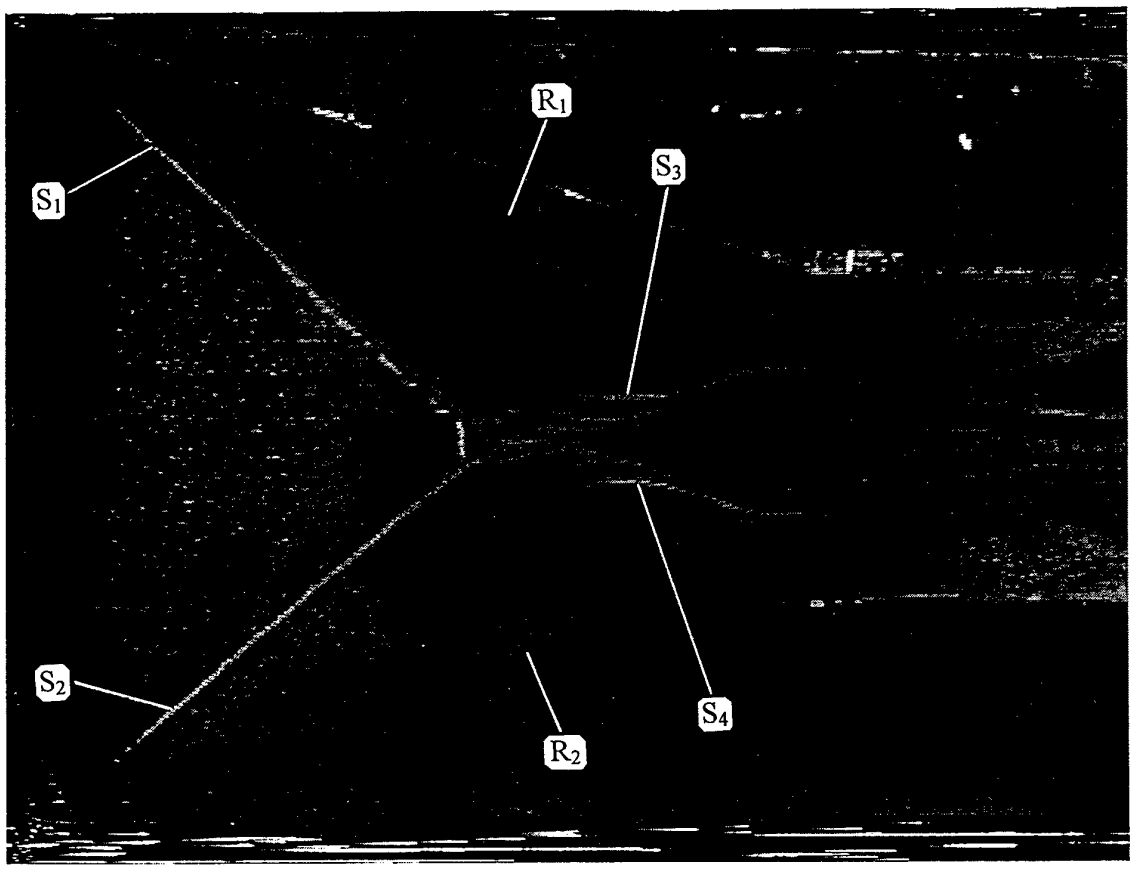

Double Fin: ß = 18°, A = 160 mm, B = 63.9 mm, L = 267 mm

M = 5, Re_1 = 40 x 10^6 1/m (RWG DLR Göttingen)

Fig. 2.14

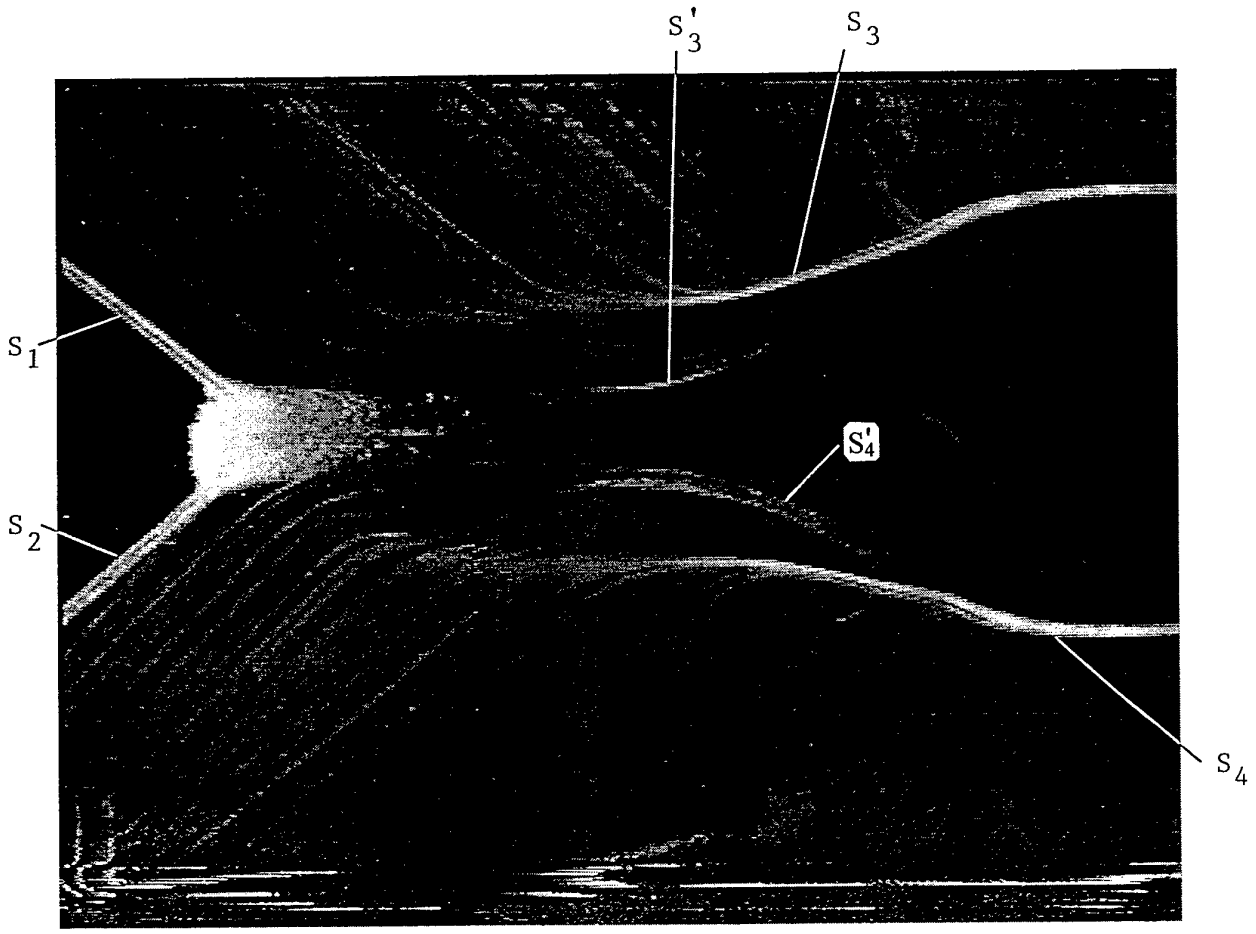

Double Fin: ß = 18°, A = 160 mm, B = 63.9 mm, L = 267 mm (Fragment)

M = 5, Re_1 = 40 x 10^6 1/m (RWG DLR Göttingen)

Fig. 2.15

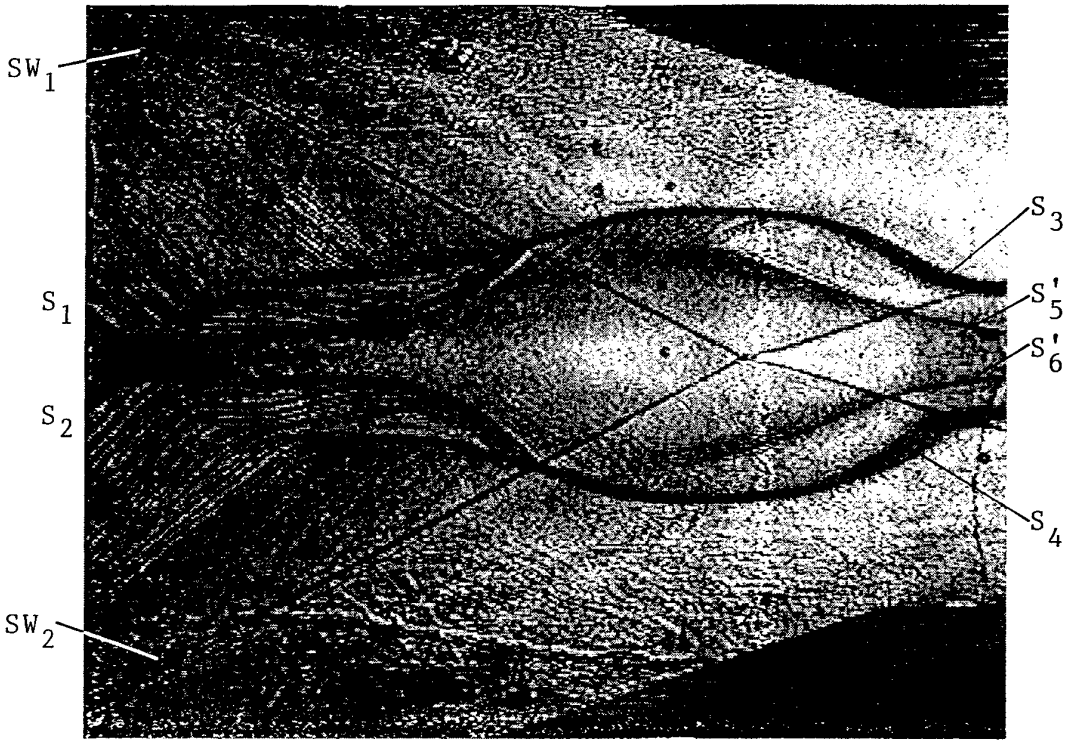

a: ß = 18°, A = 139 mm, B = 43.2 mm

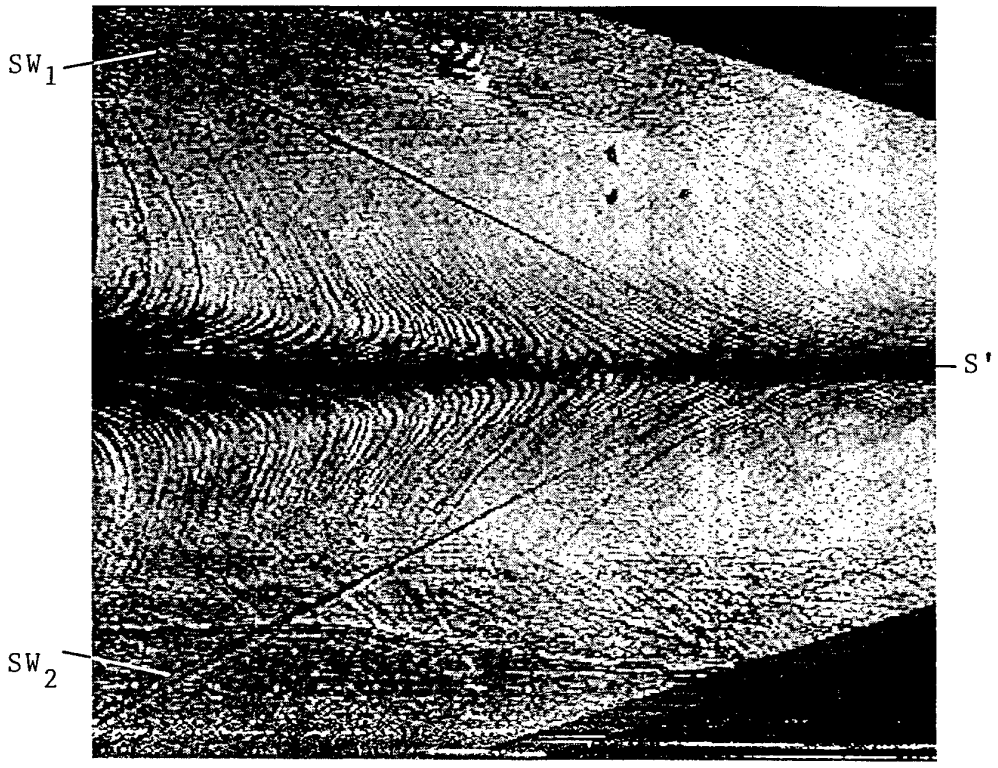

a: ß = 18°, A = 134 mm, B = 38.4 mm

Double Fin, Surface Flow Visualisation with Shadowgraph
M = 5, Re_1 = 40 x 10^6 1/m (RWG DLR Göttingen)

Fig. 2.16

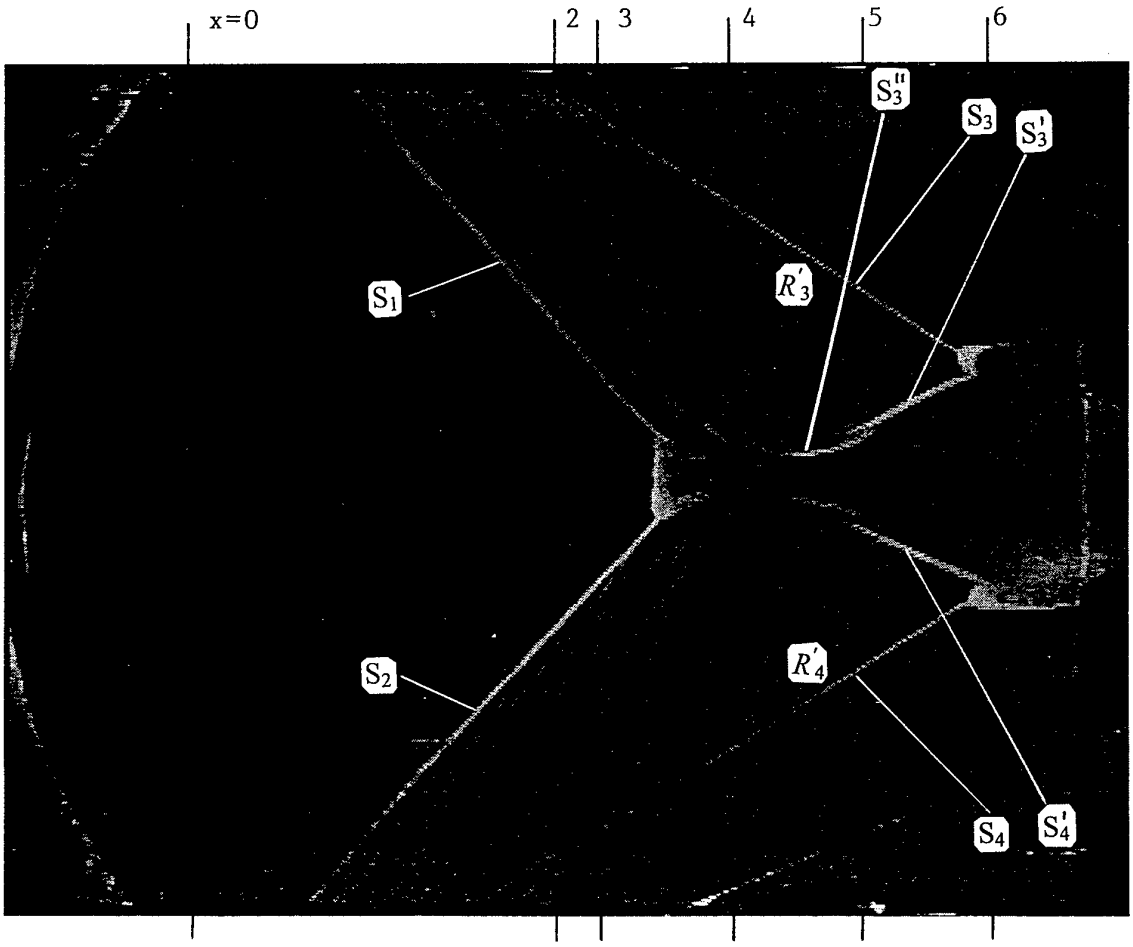

Double Fin: ß = 23°, A = 304 mm, B = 100.4 mm, L = 285 mm

M = 5, Re_1 = 40 x 10^6 1/m (RWG DLR Göttingen)

Fig. 2.17

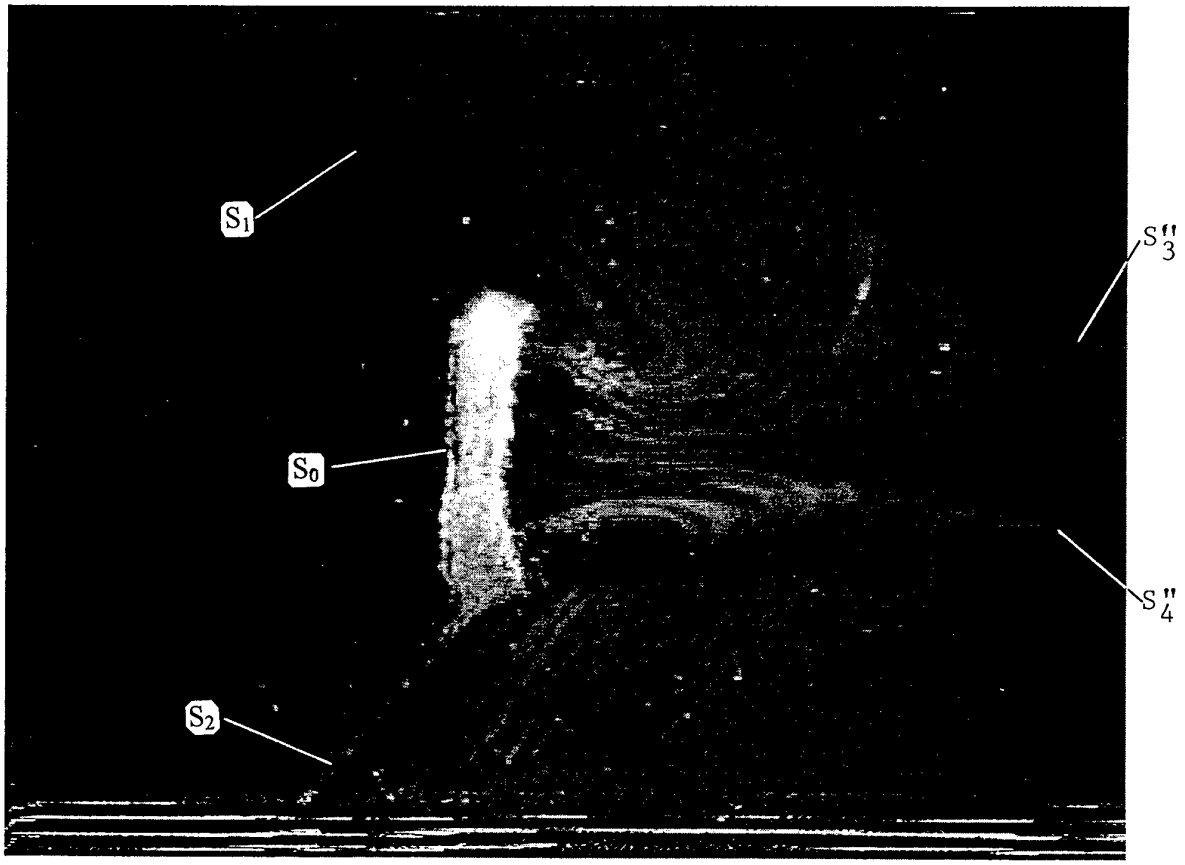

Double Fin: ß = 23°, A = 304 mm, B = 100.4 mm, L = 285 mm

M = 5, Re_l = 40 x 10^6 1/m (RWG DLR Göttingen)

Fig. 2.18

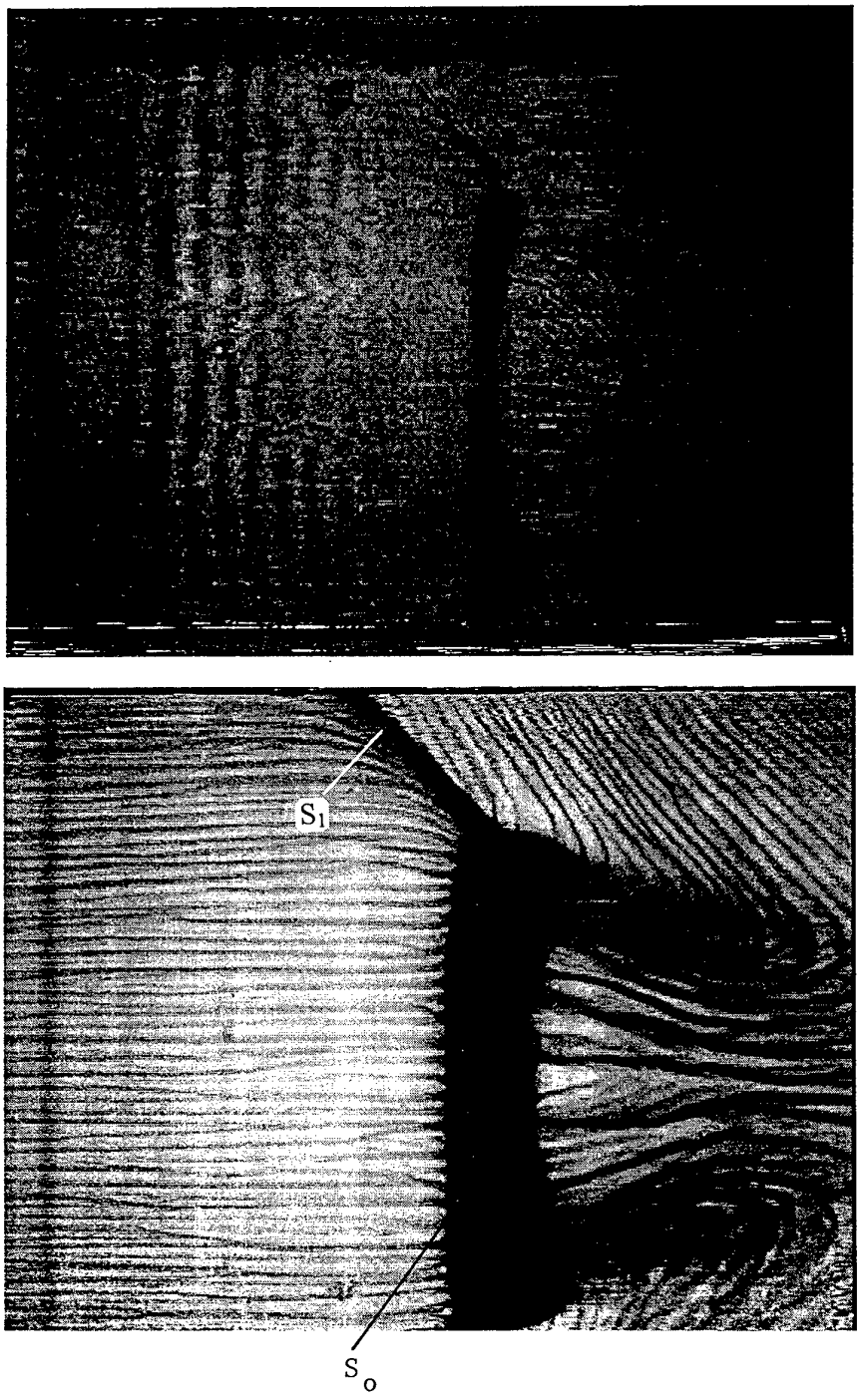

Double Fin: ß = 23°, A = 307 mm, B = 100 mm, L = 285 mm (Fragment)

Oil Film Interferometry and Surface Flow Visualisation

M = 5, $Re_1 = 40 \times 10^6$ 1/m (RWG DLR Göttingen)

Fig. 2.19

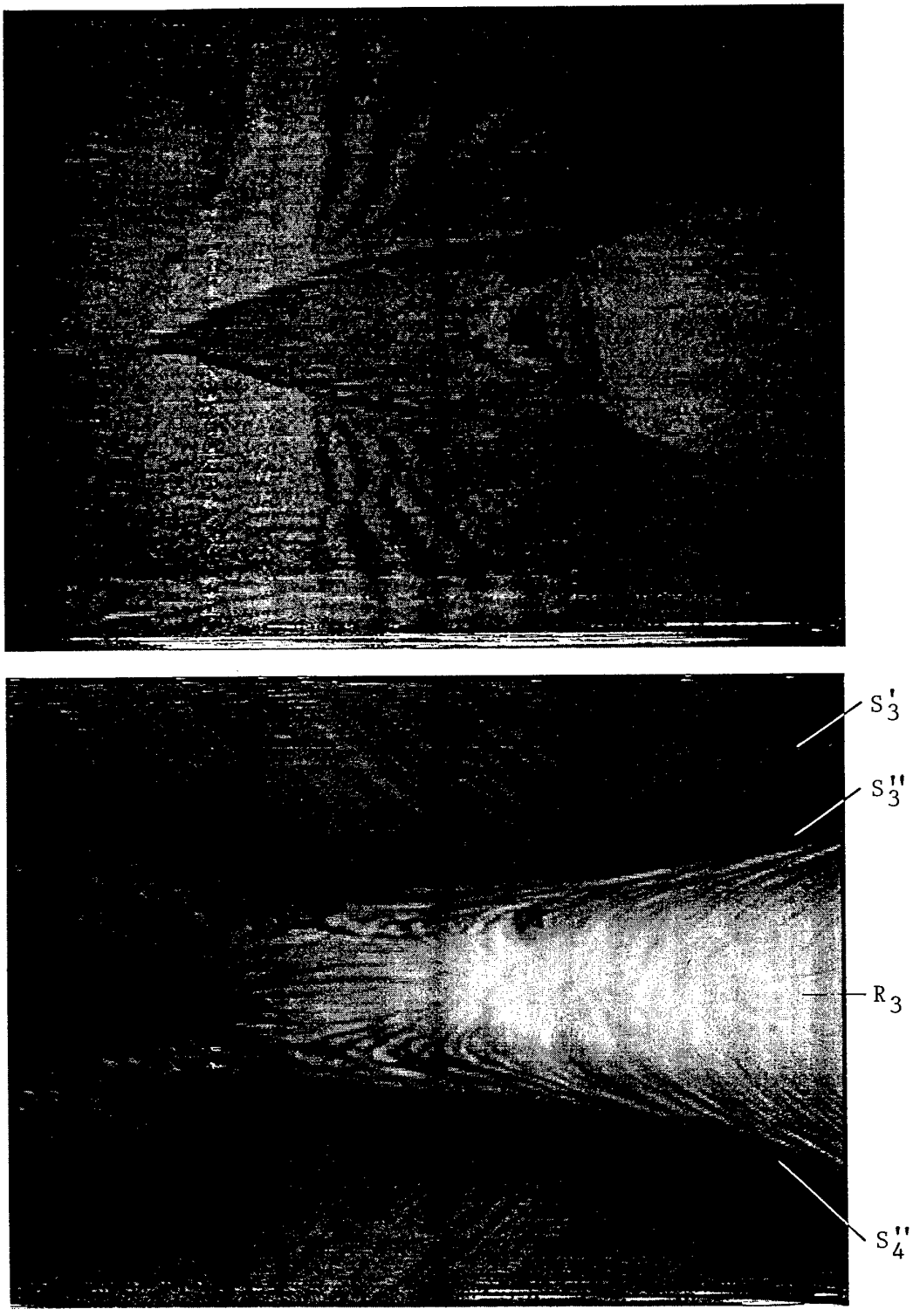

Double Fin: ß = 23°, A = 307 mm, B = 100 mm, L = 285 mm (Fragment)

Oil Film Interferometry and Surface Flow Visualisation

M = 5, $Re_1 = 40 \times 10^6$ 1/m (RWG DLR Göttingen)

Fig. 2.20

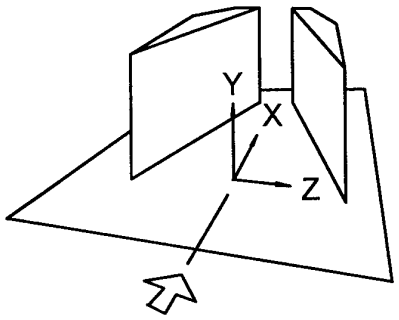

a.

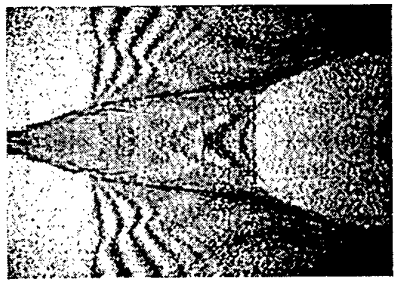

b.

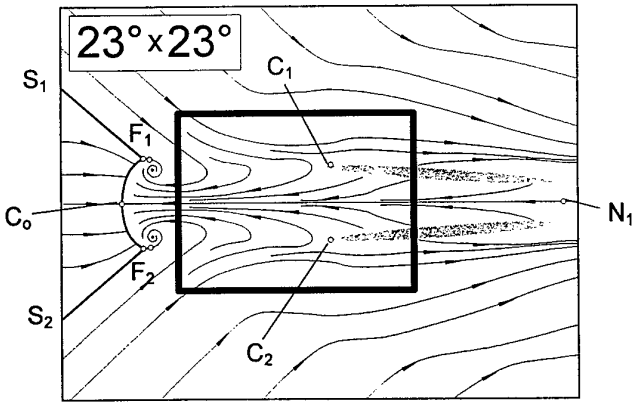

c.

Fig. 2.21. The oil interferogram and surface flow scheme for a double fin configuration at M = 5: β= 23°, A = 307 mm, B = 100 mm.

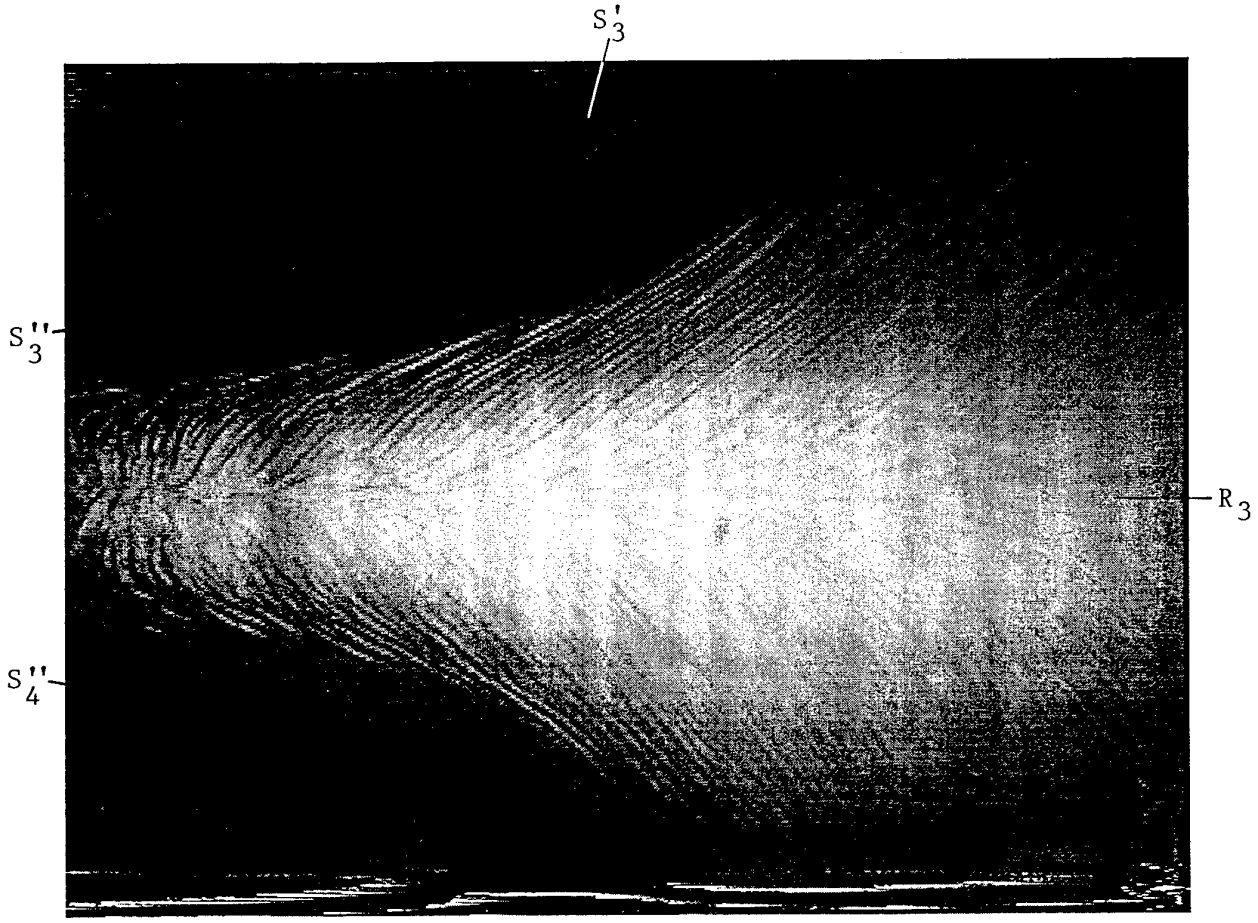

Double Fin: ß = 23°, A = 307 mm, B = 100 mm, L = 285 mm (Fragment)

M = 5, $Re_1 = 40 \times 10^6$ 1/m (RWG DLR Göttingen)

Fig. 2.22

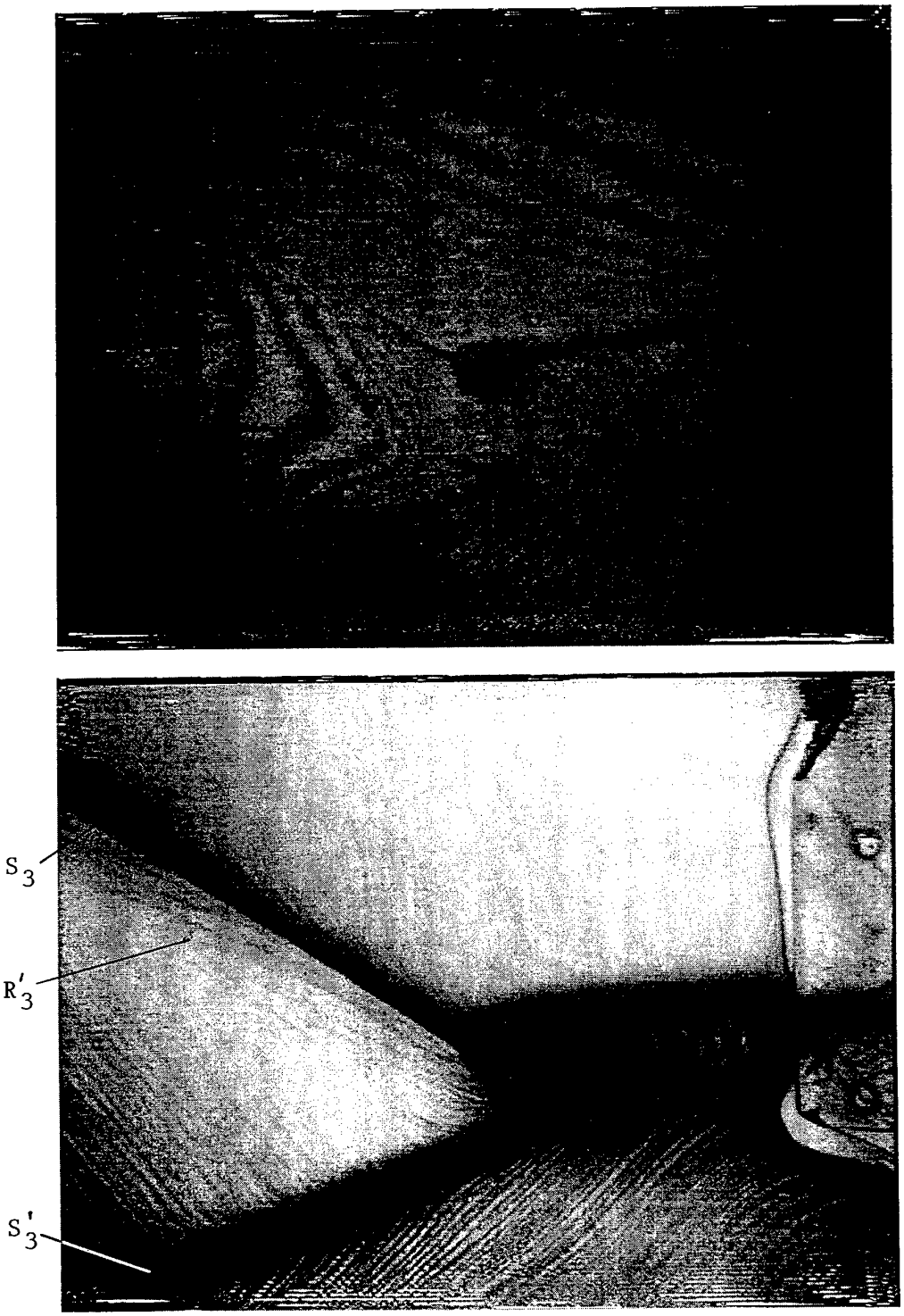

Double Fin: ß = 23°, A = 307 mm, B = 100 mm, L = 285 mm (Fragment)

M = 5, $Re_1 = 40 \times 10^6$ 1/m (RWG DLR Göttingen)

Fig. 2.23

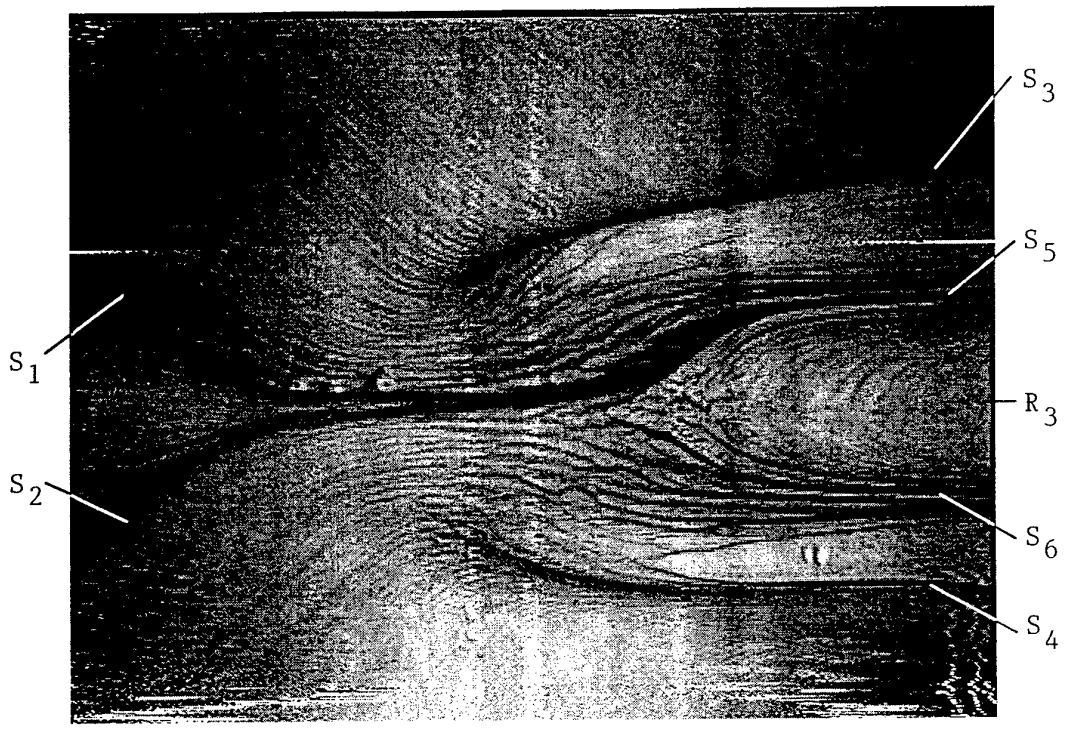

a. ß = 16°, A = 185.5 mm, B = 100 mm (Fragment)

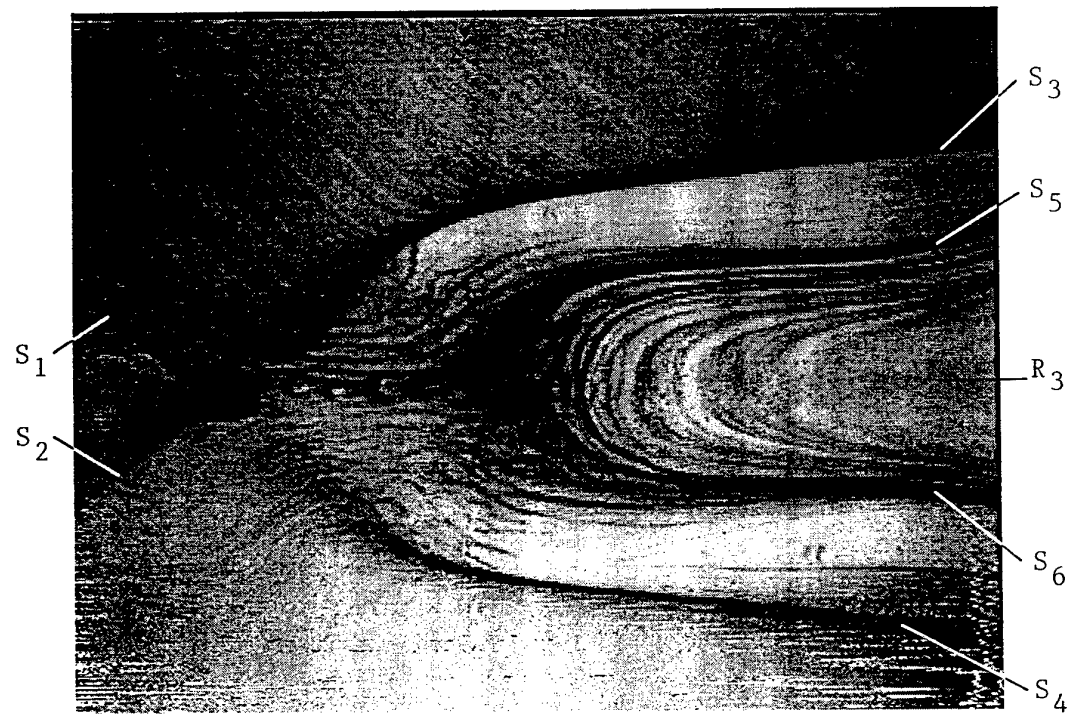

b. ß = 17°, A = 192 mm, B = 101 mm (Fragment)

Double Fin, M = 5, Re_l = 40 x 10^6 1/m (RWG DLR Göttingen)

Fig. 2.24

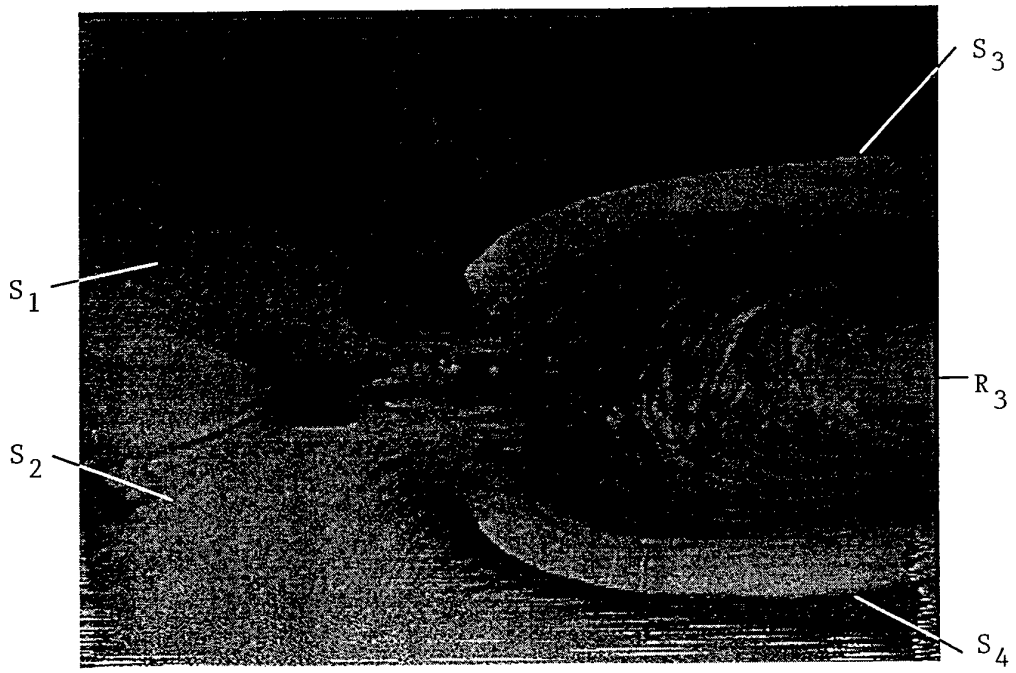

a. ß = 17.5°, A = 193 mm, B = 100 mm (Fragment)

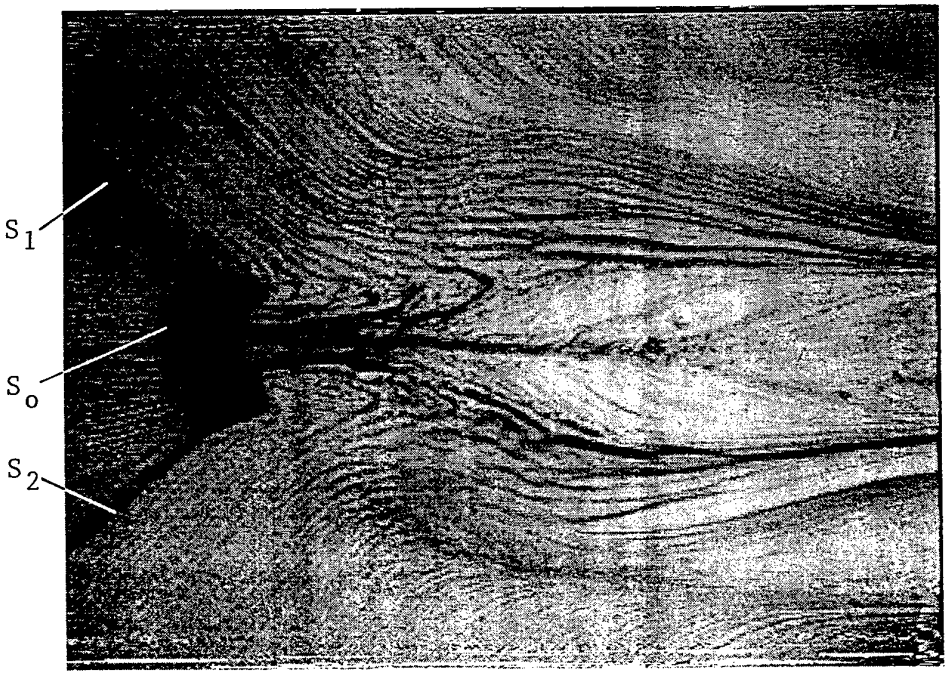

b. ß = 18°, A = 196 mm, B = 100 mm (Fragment)

Double Fin, M = 5, $Re_1 = 40 \times 10^6$ 1/m (RWG DLR Göttingen)

Fig. 2.25

APPENDIX

(Surface Pressure Distributions)

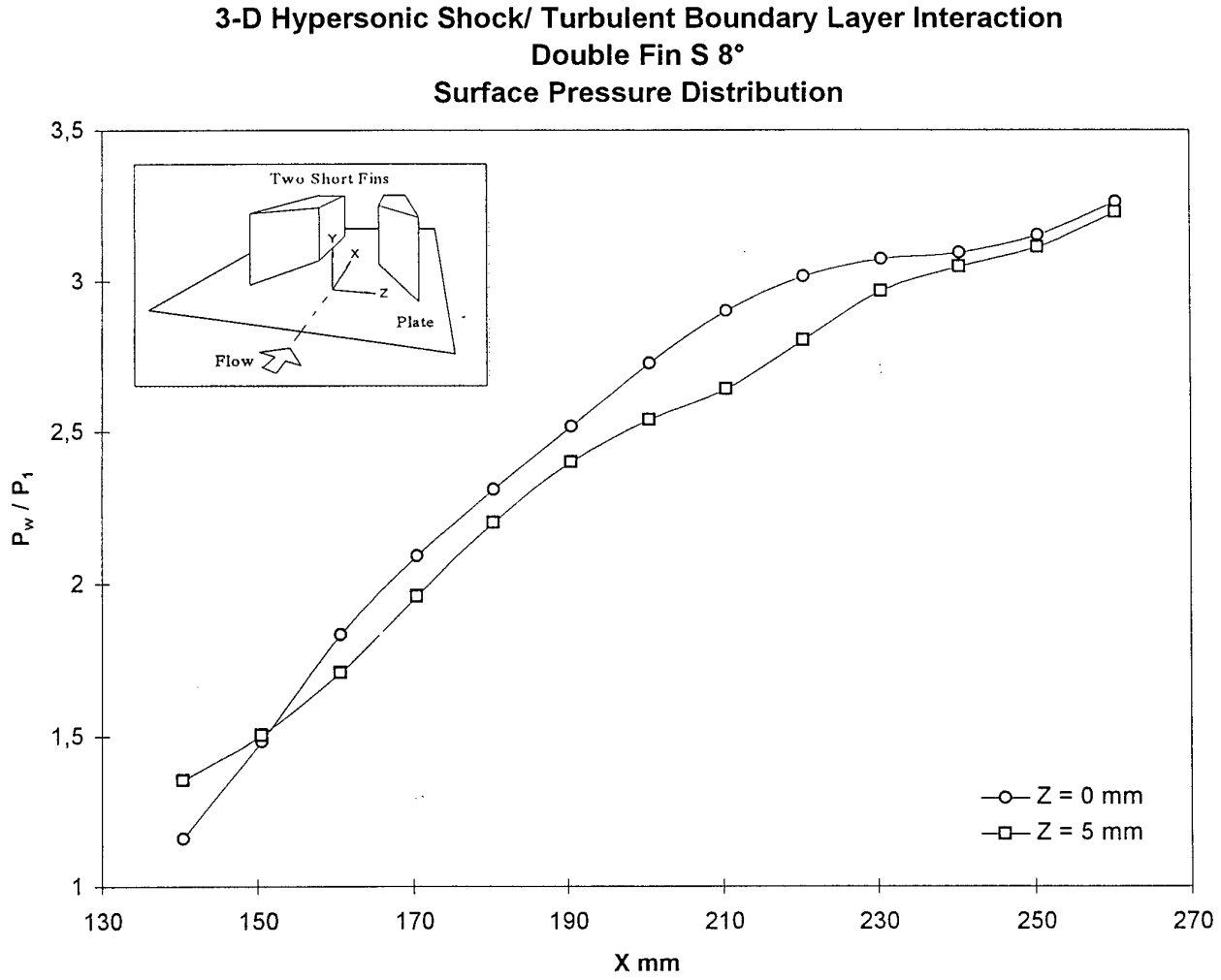
3-D Hypersonic Shock/ Turbulent Boundary Layer Interaction
Double Fin S 8°
Surface Pressure Distribution
Two Short Fins
Y
X
Z
Plate
Flow
3,5
3
2,5
2
1,5
1
P_w / P_1
130
150
170
190
210
230
250
270
X mm
Z = 0 mm
Z = 5 mm

Fig. 2.26

3-D Hypersonic Shock/ Turbulent Boundary Layer Interaction
Double Fin S 8°
Surface Pressure Distribution

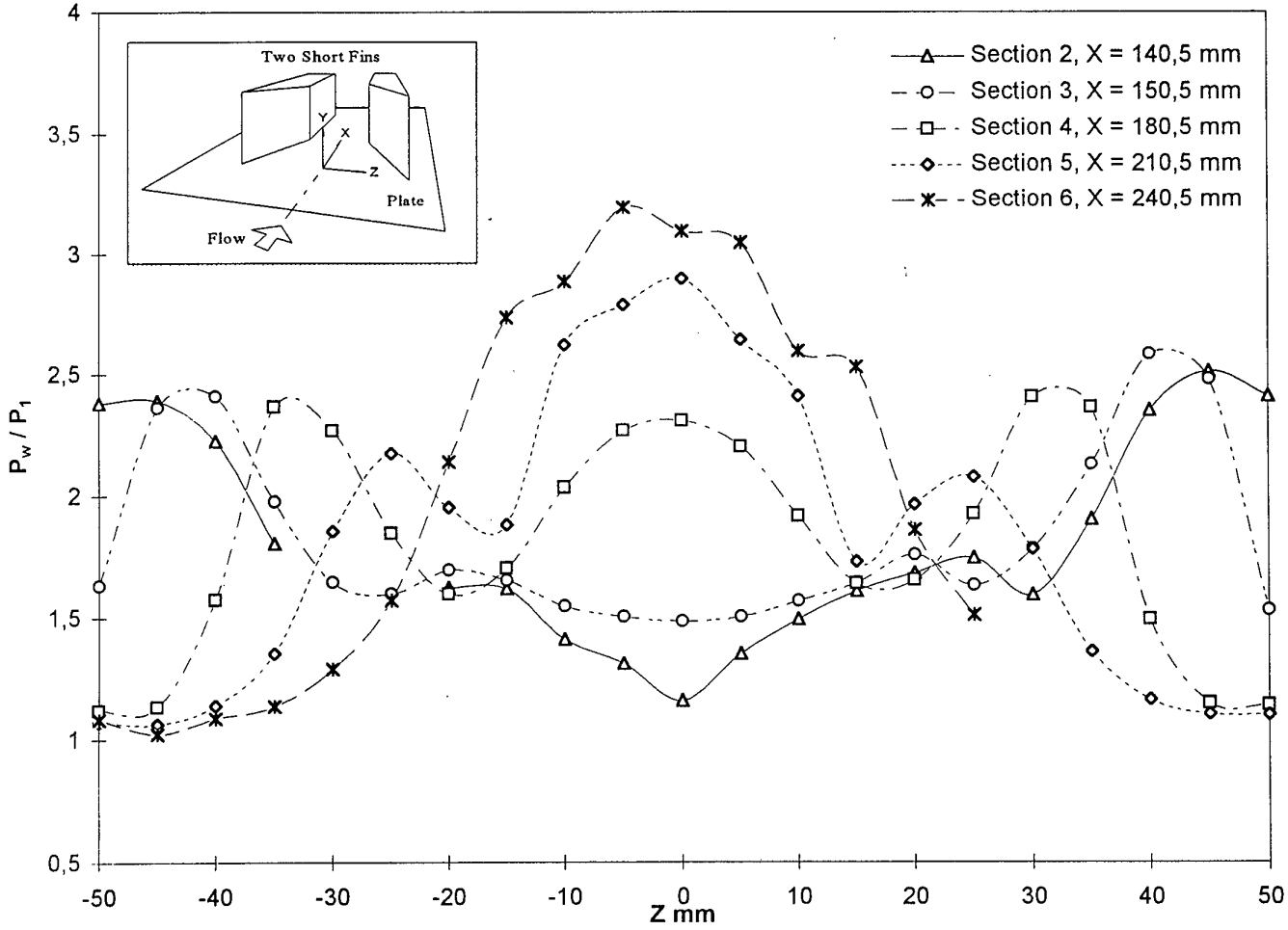

Fig. 2.27

Surface Pressure for SF 8°

Pw / P1

Z mm	Section 2	Section 3	Section 4	Section 5	Section 6
-50	2,37953496	1,63069773	1,11837208	1,07186043	1,08000004
-45	2,38818192	2,36181808	1,13302326	1,06162786	1,02139533
-40	2,22395349	2,40837216	1,57279074	1,13674414	1,08627903
-35	1,80295455	1,97590911	2,36604643	1,35116279	1,13465118
-30		1,64511633	2,26883721	1,85348833	1,287907
-25		1,5977273	1,8465116	2,17325592	1,57023251
-20	1,62418604	1,69348836	1,59720933	1,95255816	2,13744187
-15	1,61795449	1,65181816	1,70116282	1,87883723	2,73744178
-10	1,41232562	1,54627907	2,03186035	2,62162781	2,88651156
-5	1,31136358	1,50431824	2,26767445	2,7897675	3,19232559
0	1,15930235	1,48395348	2,30767441	2,89930224	3,0927906
5	1,35295451	1,50477278	2,20068192	2,64386368	3,04681826
10	1,49418604	1,56837213	1,9160465	2,40930223	2,5965116
15	1,60772729	1,6431818	1,63860464	1,72720933	2,52860475
20	1,68325579	1,75604653	1,65511632	1,96441865	1,85813951
25	1,74431813	1,63348842	1,92418599	2,07395339	1,51209307
30	1,59511626	1,78302324	2,4069767	1,7806977	
35	1,90363634	2,1281395	2,36209297	1,36186051	
40	2,35093021	2,58348846	1,49441862	1,16488373	
45	2,51409101	2,47953486	1,1497674	1,10348833	
50	2,41116285	1,53162789	1,1425581	1,10139537	

x, mm	Z = 0 mm	Z = 5 mm
140,5	1,15930235	1,35295451
150,5	1,48395348	1,50477278
160,5	1,83465111	1,71022725
170,5	2,0893023	1,96000004
180,5	2,30767441	2,20068192
190,5	2,51674414	2,4000001
200,5	2,72744179	2,54136372
210,5	2,89930224	2,64386368
220,5	3,01511621	2,80522728
230,5	3,07255816	2,96659088
240,5	3,0927906	3,04681826
250,5	3,15255809	3,11136365
260,5	3,26302314	3,22931814

Section 2, X = 140,5 mm
Section 3, X = 150,5 mm
Section 4, X = 180,5 mm
Section 5, X = 210,5 mm
Section 6, X = 240,5 mm

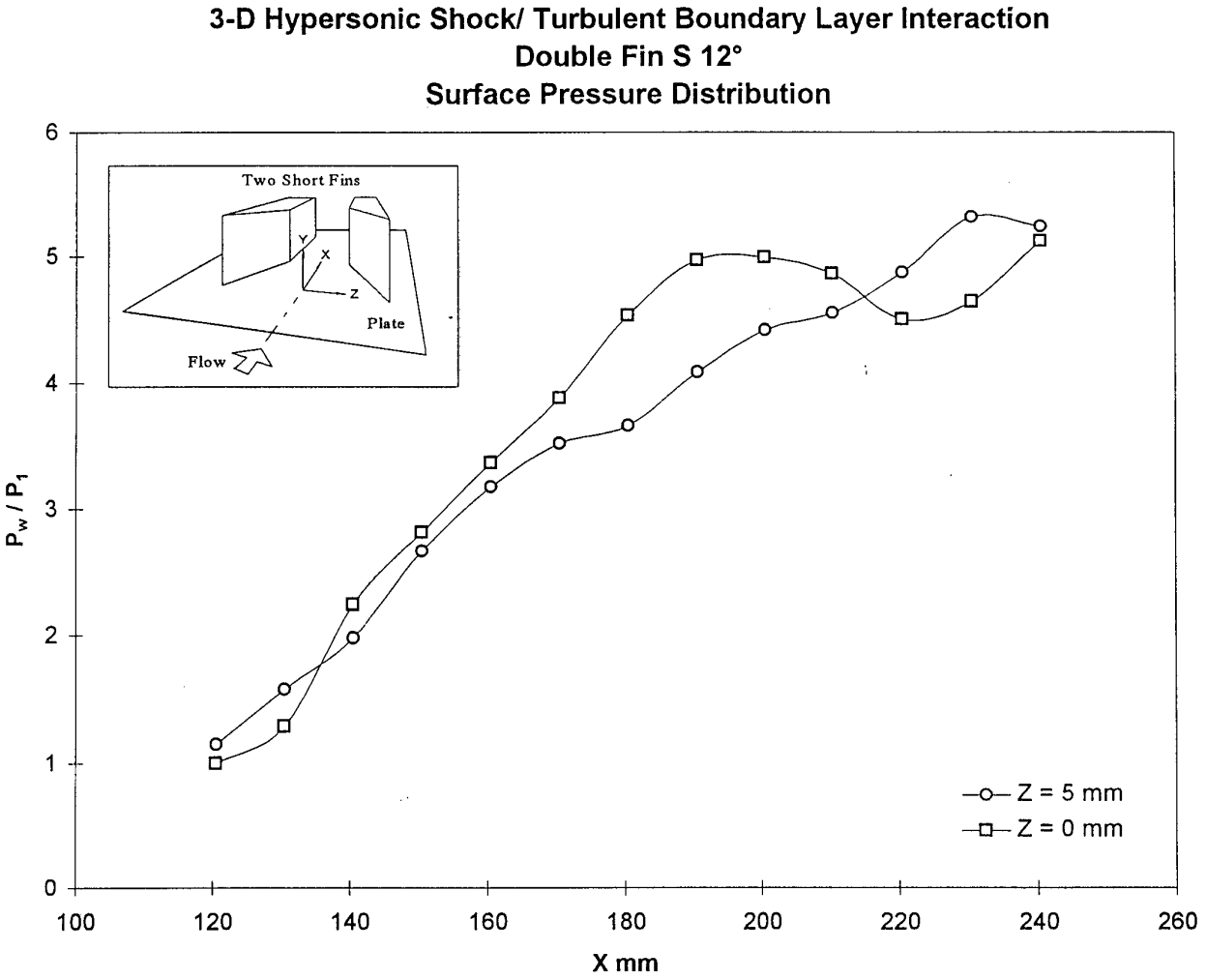
3-D Hypersonic Shock/ Turbulent Boundary Layer Interaction
Double Fin S 12°
Surface Pressure Distribution
Two Short Fins
Y
X
Z
Plate
Flow
P_w / P_1
X mm
Z = 5 mm
Z = 0 mm
0
1
2
3
4
5
6
100
120
140
160
180
200
220
240
260

Fig. 2.28

3-D Hypersonic Shock/ Turbulent Boundary Layer Interaction
Double Fin S 12°
Surface Pressure Distribution

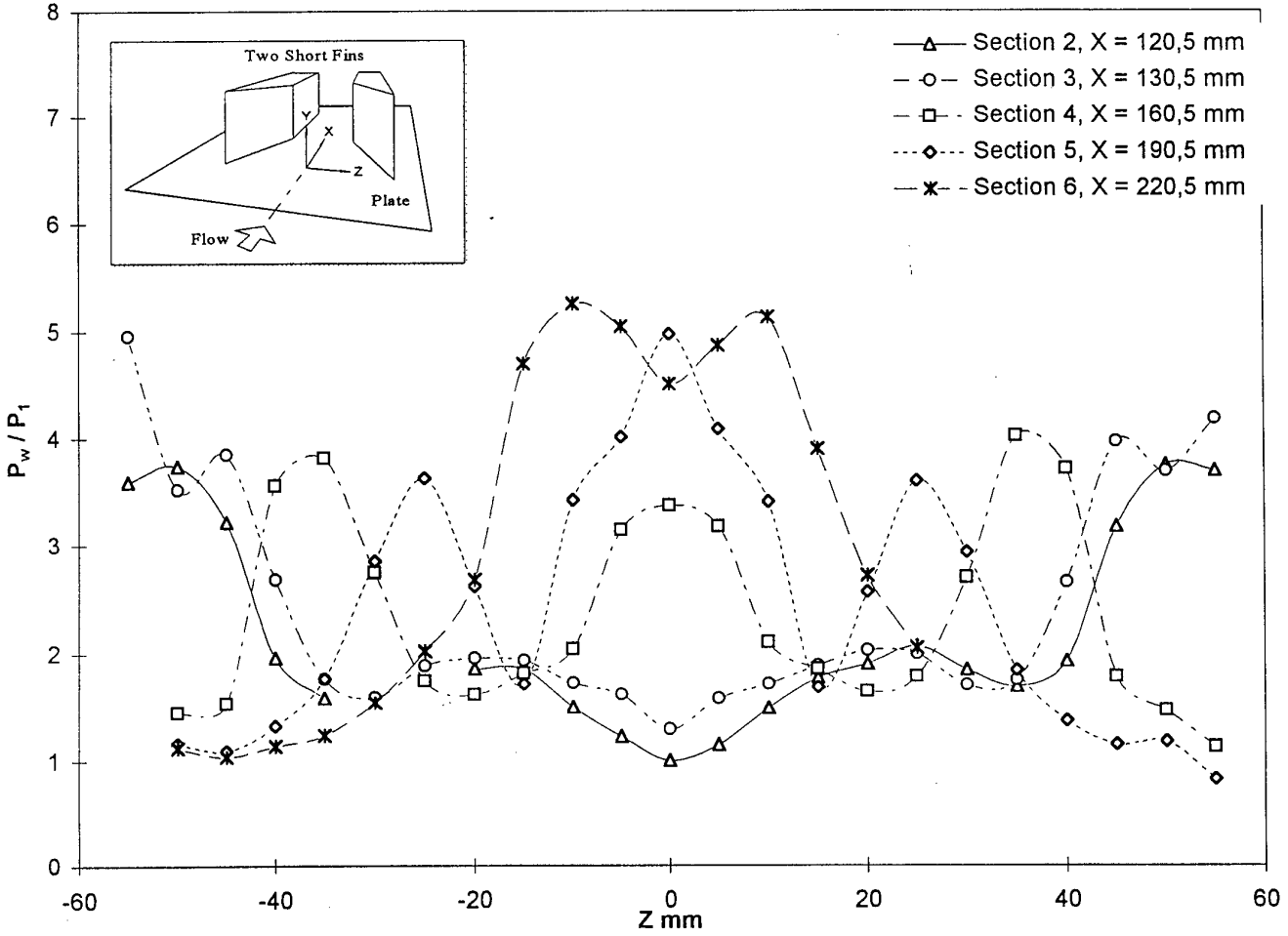

Fig. 2.29

Surface Pressure for SF 12°

	Pw / P1				
Z mm	Section 2	Section 3	Section 4	Section 5	Section 6
-55	3,58697677	4,95581388			
-50	3,73441863	3,51930237	1,44348836	1,15488374	1,12046516
-45	3,21674418	3,84372091	1,53395355	1,09023261	1,037907
-40	1,96581399	2,67604661	3,55511618	1,32162786	1,13395345
-35	1,58186042	1,76093018	3,81162786	1,76465118	1,23000002
-30		1,58651161	2,74093032	2,84767437	1,53581393
-25		1,88767445	1,74418604	3,62255812	2,02093029
-20	1,86023259	1,95883715	1,61302328	2,61348844	2,67395353
-15	1,8555814	1,93790698	1,8141861	1,71418607	4,6934886
-10	1,49302328	1,72372091	2,04348826	3,41720939	5,257442
-5	1,22325587	1,6127907	3,13953495	4,00976753	5,04255819
0	0,9995349	1,28813958	3,36744189	4,97279072	4,5060463
5	1,14674413	1,57720935	3,17441869	4,0855813	4,87116289
10	1,48279071	1,71348834	2,10488367	3,4034884	5,1293025
15	1,77232563	1,88558137	1,8555814	1,68209302	3,89348841
20	1,90069771	2,03023267	1,64116275	2,55976748	2,70953488
25	2,06558132	1,99372089	1,78116274	3,59581399	2,04883718
30	1,84674418	1,70255816	2,69186044	2,9288373	
35	1,6913954	1,75069773	4,01651144	1,84395349	
40	1,93023252	2,65069771	3,70558143	1,36302328	
45	3,17604661	3,96232557	1,78162789	1,14488375	
50	3,74441862	3,68813944	1,46093023	1,17069769	
55	3,69023252	4,18302345	1,12441862	0,81604654	

X mm	Z = 0 mm	Z = 5 mm
120,5	0,9995349	1,14674413
130,5	1,28813958	1,57720935
140,5	2,23581386	1,97790694
150,5	2,81279063	2,65395355
160,5	3,36744189	3,17441869
170,5	3,88186049	3,51976752
180,5	4,53651142	3,66279078
190,5	4,97279072	4,0855813
200,5	4,99558163	4,41674423
210,5	4,86069775	4,5569768
220,5	4,5060463	4,87116289
230,5	4,64674425	5,32651186
240,5	5,12906981	5,24604654

Section 2, X = 120,5 mm
Section 3, X = 130,5 mm
Section 4, X = 160,5 mm
Section 5, X = 190,5 mm
Section 6, X = 220,5 mm

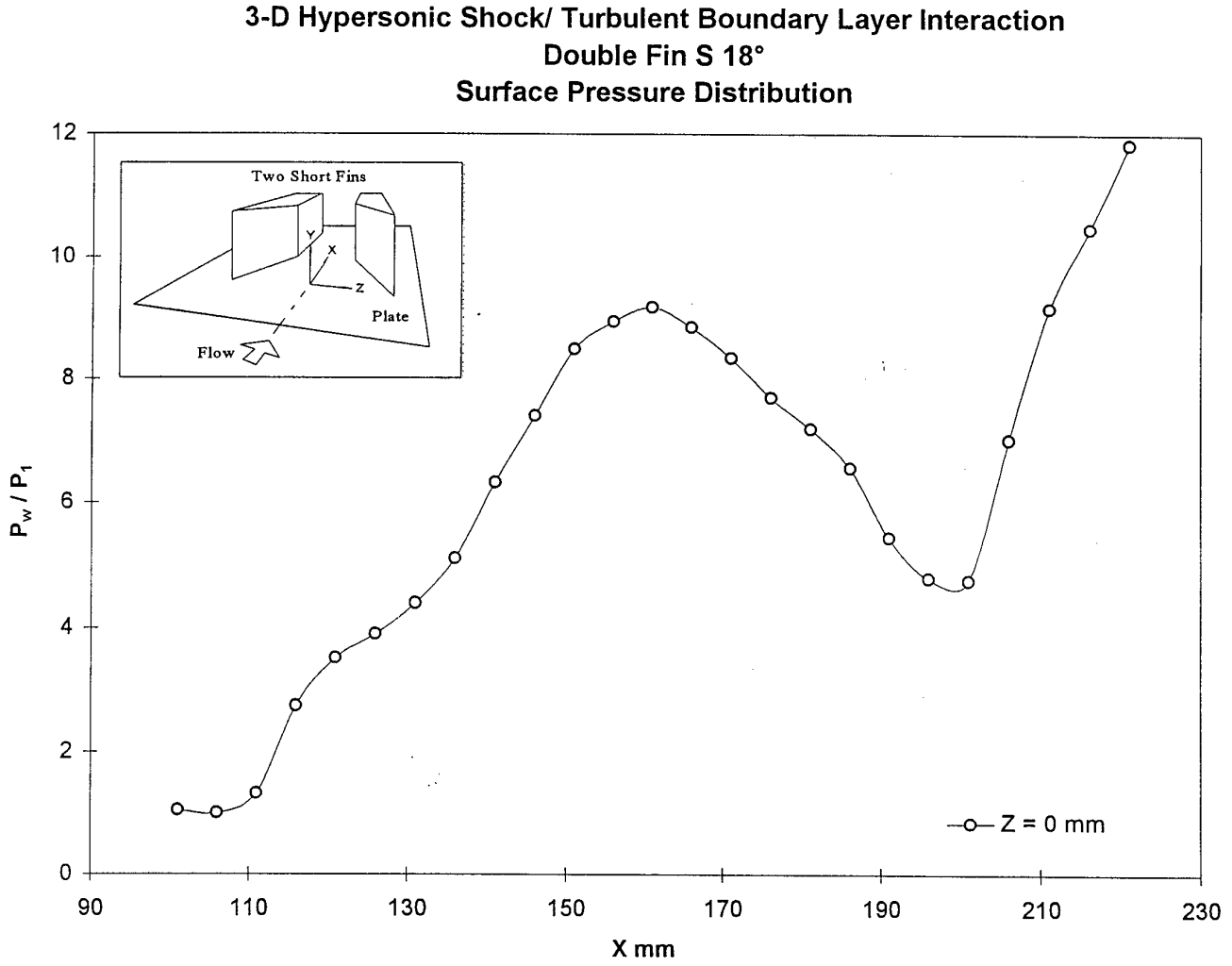
3-D Hypersonic Shock/ Turbulent Boundary Layer Interaction
Double Fin S 18°
Surface Pressure Distribution
Two Short Fins
Y
X
Z
Plate
Flow
P_w / P_1
X mm
Z = 0 mm
0
2
4
6
8
10
12
90
110
130
150
170
190
210
230

Fig. 2.30

3-D Hypersonic Shock/ Turbulent Boundary Layer Interaction
Double Fin S 18°
Surface Pressure Distribution

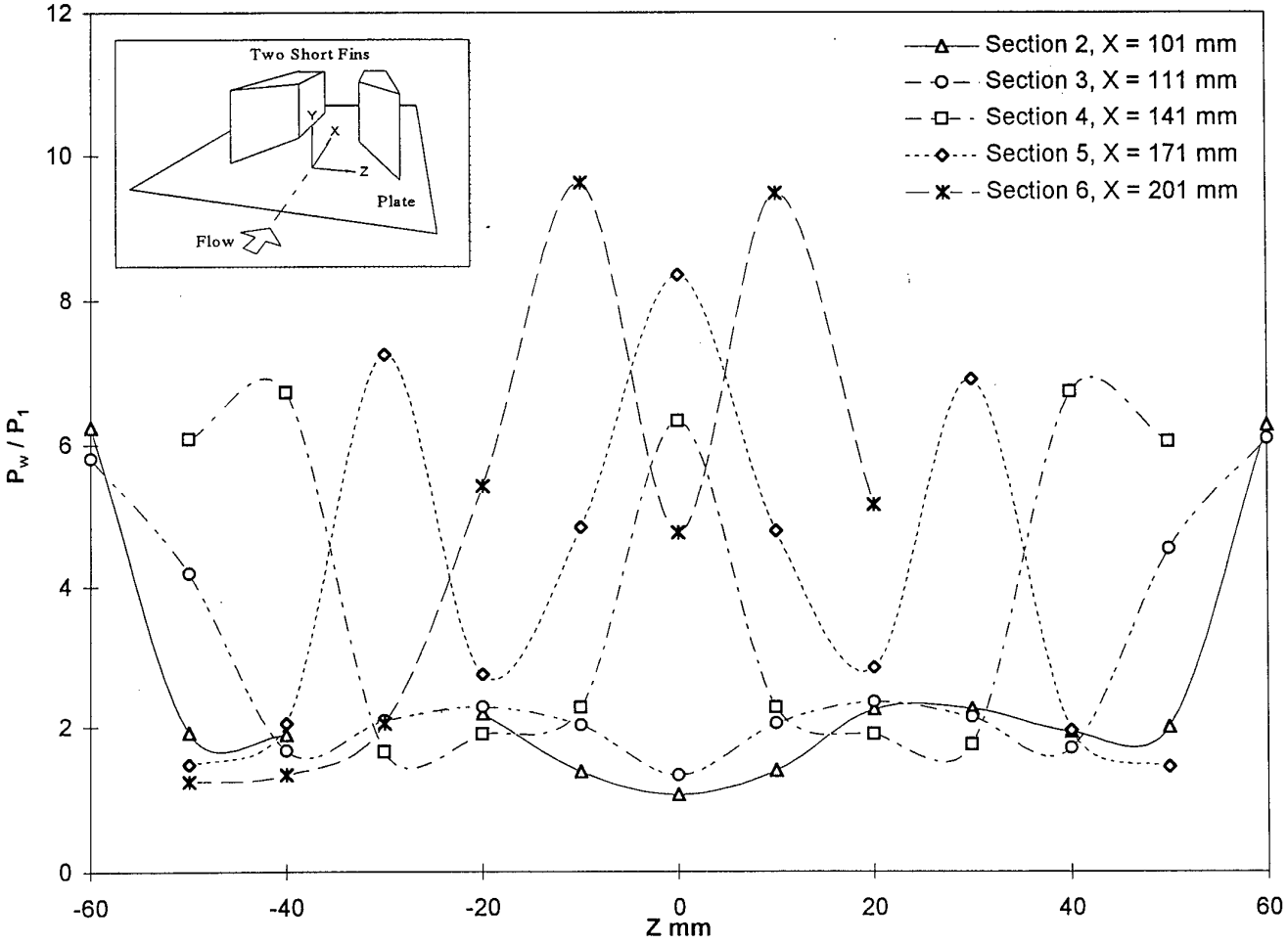

Fig. 2.31

Surface Pressure for SF 18°

Z mm	Pw / P1 Section 2	Section 3	Section 4	Section 5	Section 6
-60	6,23044443	5,80288887			
-50	1,9133333	4,19222212	6,07441854	1,46976745	1,23279071
-40	1,89111114	1,6684444	6,71744204	2,04813957	1,33325577
-30		2,08866668	1,65372097	7,24627924	2,04395342
-20	2,1833334	2,28577781	1,89697671	2,74883723	5,40325594
-10	1,37600005	2,01644444	2,27697682	4,82302332	9,6218605
0	1,05688894	1,32533336	6,32533312	8,34977818	4,75244427
10	1,38822222	2,04288888	2,27627897	4,77604628	9,46930218
20	2,2522223	2,35511637	1,8997674	2,84930229	5,14790678
30	2,25377774	2,13418603	1,75395346	6,89162779	
40	1,92933333	1,69837213	6,72372103	1,94744182	
50	1,99977779	4,53441858	6,03651142	1,4376744	
60	6,26933336	6,07372093			

X mm	Z = 0 mm
101	1,05688894
106	1,00340915
111	1,32533336
116	2,74000001
121	3,51133323
126	3,90409088
131	4,39088869
136	5,0977273
141	6,32533312
146	7,39295435
151	8,49577808
156	8,94522762
161	9,18022251
166	8,85227299
171	8,34977818
176	7,70090914
181	7,18688869
186	6,55909109
191	5,43266678
196	4,78340912
201	4,75244427
206	7,00954533
211	9,16355515
216	10,4693184
221	11,832222

Section 2, X = 101 mm
Section 3, X = 111 mm
Section 4, X = 141 mm
Section 5, X = 171 mm
Section 6, X = 201 mm

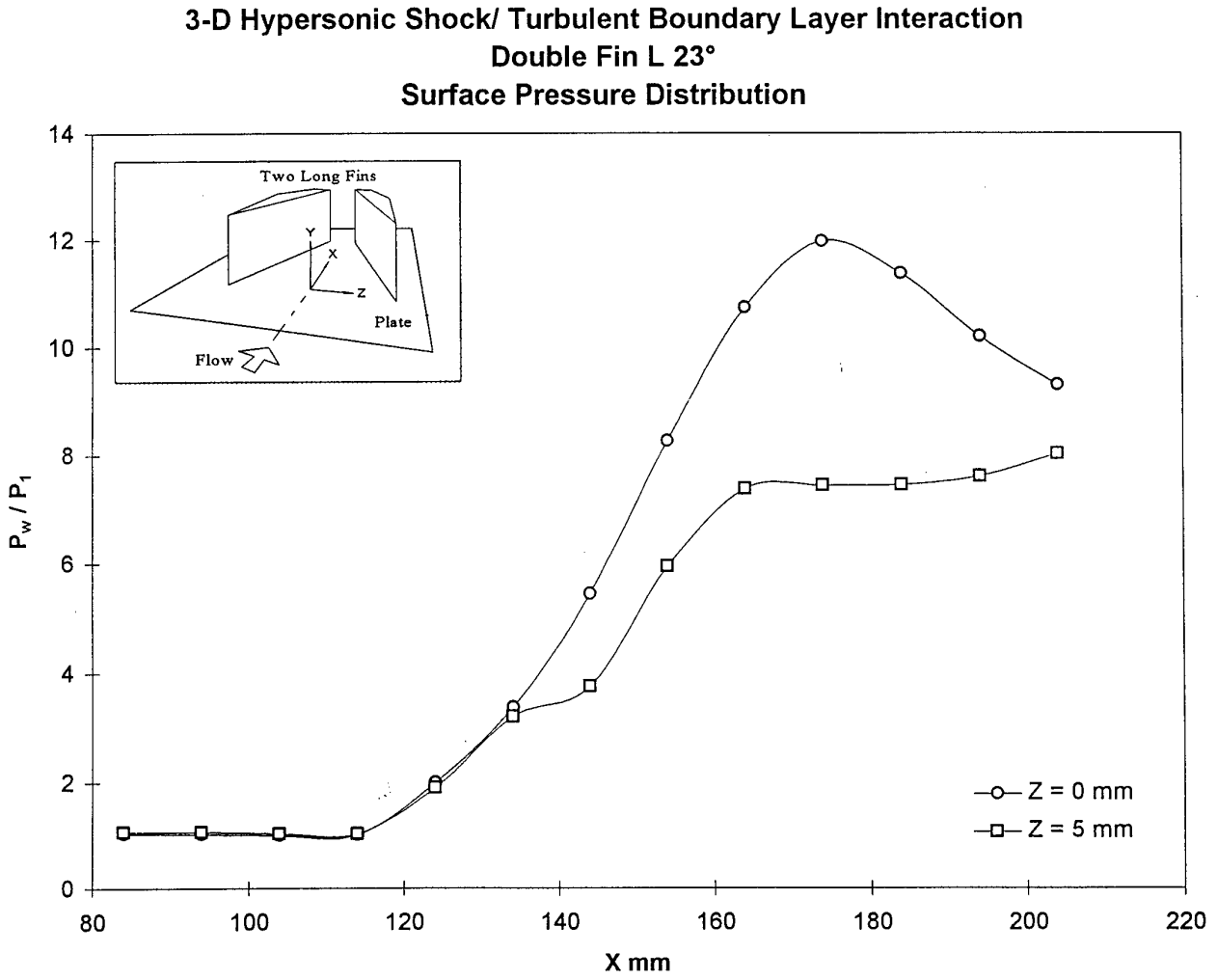
3-D Hypersonic Shock/ Turbulent Boundary Layer Interaction
Double Fin L 23°
Surface Pressure Distribution
Two Long Fins
Y
X
Z
Plate
Flow
P_w / P_1
X mm
Z = 0 mm
Z = 5 mm
0
2
4
6
8
10
12
14
80
100
120
140
160
180
200
220

Fig. 2.32

3-D Hypersonic Shock/ Turbulent Boundary Layer Interaction
Double Fin L 23°
Surface Pressure Distribution

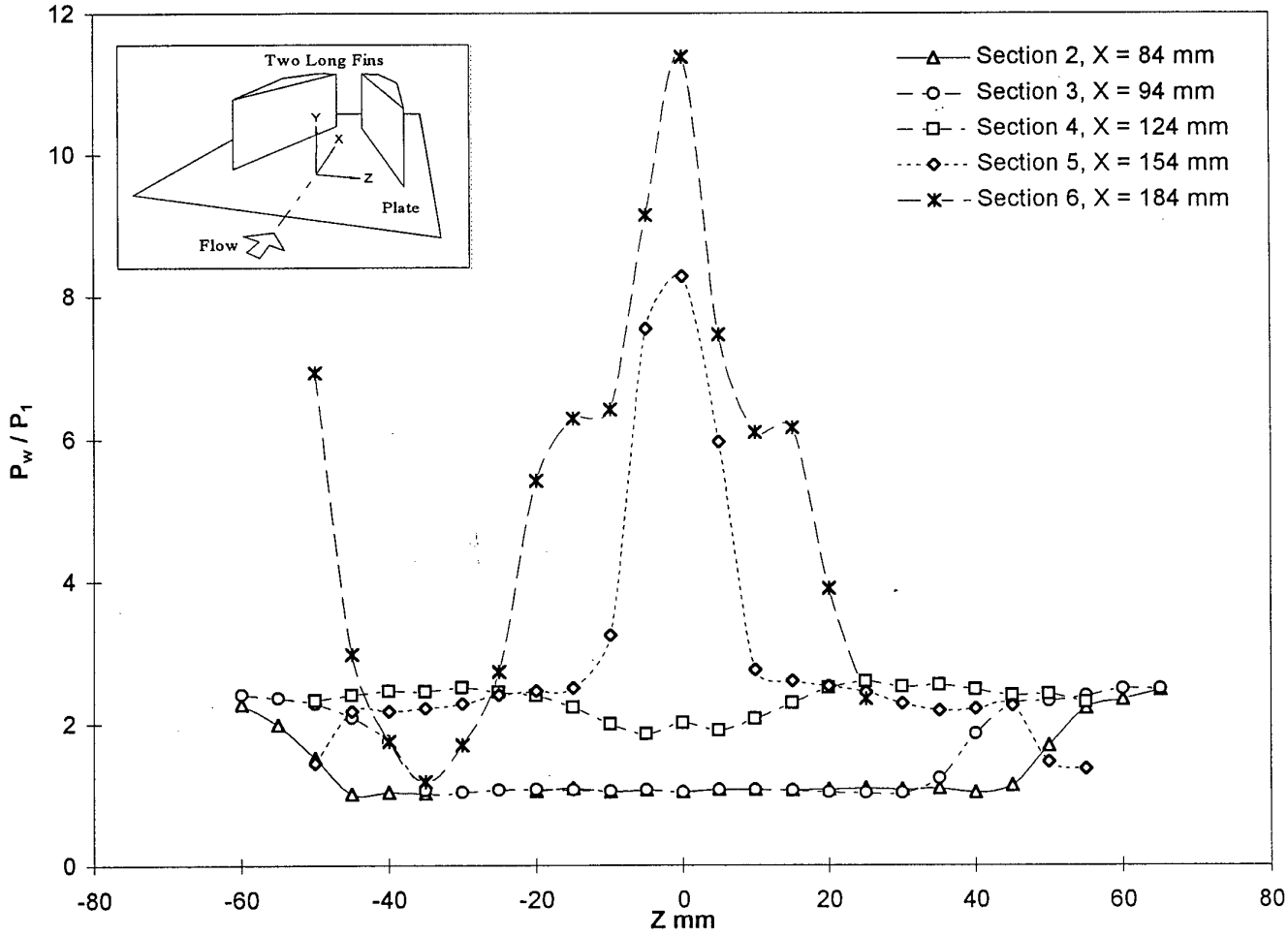

Fig. 2.33

Surface Pressure for LF 23°

Z mm	Pw / P1				
	Section 2	Section 3	Section 4	Section 5	Section 6
-60	2,26279068	2,40813947			
-55	1,97604656	2,35255814			
-50	1,51279068	2,27069759	2,32534885	1,43837214	6,92116261
-45	1,00209308	2,08162785	2,39744186	2,16976738	2,96860456
-40	1,03023255	1,74046516	2,4539535	2,16953492	1,74348843
-35	1,01325583	1,05465114	2,44534874	2,21232557	1,18069768
-30		1,03209305	2,50325584	2,27790689	1,68976748
-25		1,0641861	2,43813944	2,39930224	2,72418594
-20	1,04999995	1,07209301	2,38720942	2,45325589	5,41348839
-15	1,08883727	1,06558144	2,22255802	2,49790692	6,28325558
-10	1,03581393	1,04441857	1,98511624	3,2393024	6,40883732
-5	1,06255817	1,06069767	1,84674418	7,53720951	9,13023281
0	1,04116285	1,02813959	2,00162792	8,2704649	11,3762789
5	1,07116282	1,06604648	1,89581394	5,95186043	7,45465136
10	1,07255816	1,06558144	2,06488371	2,75186038	6,08465099
15	1,0641861	1,05790699	2,27906966	2,59046507	6,15325594
20	1,07418609	1,03325582	2,49302316	2,51604652	3,8900001
25	1,08860469	1,01999998	2,58627915	2,43627906	2,335814
30	1,07046509	1,0234884	2,51279068	2,27720928	
35	1,09162796	1,22790694	2,53860474	2,17744184	
40	1,03162789	1,84883726	2,47023249	2,19930243	
45	1,13	2,26255822	2,3925581	2,24232554	
50	1,68813956	2,30511618	2,4034884	1,46000004	
55	2,20465112	2,3816278	2,28930235	1,36023259	
60	2,33418608	2,48093033			
65	2,45906973	2,47534895			

X mm	Z = 0 mm	Z = 5 mm
84	1,04116285	1,07116282
94	1,02813959	1,06604648
104	1,00697672	1,037907
114	1,01790702	1,03302324
124	2,00162792	1,89581394
134	3,36976743	3,20418596
144	5,44813967	3,75906968
154	8,2704649	5,95186043
164	10,7372093	7,37441874
174	11,970233	7,44674397
184	11,3762789	7,45465136
194	10,1995344	7,61930227
204	9,30372047	8,03023243

Section 2, X = 84 mm
Section 3, X = 94 mm
Section 4, X = 124 mm
Section 5, X = 154 mm
Section 6, X = 184 mm